MOLECULAR BEAM EPITAXIAL GROWTH AND CHARACTERIZATION OF EXTENDED SHORT WAVELENGTH INFRARED MERCURY CADMIUM TELLURIDE DETECTORS

A THESIS SUBMITTED TO
THE GRADUATE SCHOOL OF NATURAL AND APPLIED SCIENCES
OF
MIDDLE EAST TECHNICAL UNIVERSITY

BY

EMRAH ŞAŞMAZ

IN PARTIAL FULFILLMENT OF THE REQUIREMENTS
FOR
THE DEGREE OF MASTER OF SCIENCE
IN
ELECTRICAL AND ELECTRONICS ENGINEERING

SEPTEMBER 2017

Approval of the thesis:

MOLECULAR BEAM EPITAXIAL GROWTH AND CHARACTERIZATION OF EXTENDED SHORT WAVELENGTH INFRARED MERCURY CADMIUM TELLURIDE DETECTORS

submitted by **EMRAH ŞAŞMAZ** in partial fulfillment of the requirements for the degree of **Master of Science in Electrical and Electronics Engineering Department, Middle East Technical University** by,

Prof. Dr. Gülbin Dural Ünver
Dean, Graduate School of **Natural and Applied Sciences** _____

Prof. Dr. Tolga Çiloğlu
Head of Department, **Electrical and Electronics Engineering** _____

Prof. Dr. Cengiz Beşikci
Supervisor, **Electrical and Electronics Eng. Dept., METU** _____

Examining Committee Members:

Prof. Dr. Tayfun Akın
Electrical and Electronics Engineering Dept., METU _____

Prof. Dr. Cengiz Beşikci
Electrical and Electronics Engineering Dept., METU _____

Prof. Dr. Mehmet Parlak
Physics Dept., METU _____

Assist. Prof. Dr. Serdar Kocaman
Electrical and Electronics Engineering Dept., METU _____

Assist. Prof. Dr. Dinçer Gökcen
Electrical and Electronics Eng. Dept., Hacettepe University . _____

Date: 06.09.2017

I hereby declare that all information in this document has been obtained and presented in accordance with academic rules and ethical conduct. I also declare that, as required by these rules and conduct, I have fully cited and referenced all material and results that are not original to this work.

Name, Last Name : Emrah ŞAŞMAZ

Signature :

ABSTRACT

MOLECULAR BEAM EPITAXIAL GROWTH AND CHARACTERIZATION OF EXTENDED SHORT WAVELENGTH INFRARED MERCURY CADMIUM TELLURIDE DETECTORS

Şaşmaz, Emrah

M.S., Department of Electrical and Electronics Engineering

Supervisor: Prof. Dr. Cengiz Beşikci

September 2017, 111 pages

This thesis reports the growth, fabrication and characterization of extended short wavelength infrared (SWIR) mercury cadmium telluride ($Hg_{1-x}Cd_xTe$) photodiodes with a cut off wavelength of 2.17 μm at room temperature. HgCdTe layers were grown on home-polished cadmium zinc telluride, CdZnTe, substrates by molecular beam epitaxy (MBE).

Test arrays were fabricated in order to evaluate the electrical and optical characteristics of the photodiodes. Test array consists of mesa type pixels with 30 μm pitch. The test array was hybridized with silicon fan-out with flip-chip bonder.

Electrical and optical characterization performed on 28x28 μm^2 detectors yielded a room temperature dark current density of ~100 $\mu A/cm^2$ which is diffusion limited. The peak responsivity of the test diodes without anti-reflection coating is 1.0 A/W corresponding to a quantum efficiency of 62%. Dark current limited peak detectivity of the detectors is 1.17×10^{11} $cm\sqrt{Hz}/W$ at room temperature.

Deep level transient spectroscopy (DLTS) measurements were performed on the detectors in order to identify the performance limiting material characteristics. DLTS measurements yielded a hole trap with activation energy of 267 meV, capture cross section of $2.0x10^{-17}$ cm^2 and trap density of $3x10^{13}$ cm^{-3}. The trap does not display extended defect characteristics suggesting that it originates from isolated defects in the material.

Keywords: Mercury Cadmium Telluride (MCT), extended short wavelength infrared (SWIR), Molecular Beam Epitaxy (MBE)

ÖZ

UZATILMIŞ KISA DALGA BOYU KIZILÖTESİ CIVA KADMİYUM TELLÜR DEDEKTÖRLERİN MOLEKÜLER IŞIN EPİTAKSİSİ İLE BÜYÜTÜLMESİ VE KARAKTERİZASYONU

Şaşmaz, Emrah

Yüksek Lisans, Elektrik – Elektronik Mühendisliği Bölümü

Tez Yöneticisi : Prof. Dr. Cengiz Beşikci

Eylül 2017, 111 sayfa

Bu tezde, oda sıcaklığıdaki kesim dalga boyu 2.17 µm olan uzatılmış kısa dalga boyu kızılötesi cıva kadmiyum tellür ($Hg_{1-x}Cd_xTe$) fotodiyotların büyütülmesi, fabrikasyonu ve karakterizasyonu rapor edilmektedir. HgCdTe filmleri Aselsan A.Ş.'de parlatılmış kadmiyum çinko tellür, CdZnTe, tabanlar üzerine moleküler ışın epitaksi (MBE) yöntemi ile büyütülmüştür.

Elektriksel ve optiksel testleri yapabilmek için test matrisleri fabrike edilmiştir. Test matrisleri 30 µm adımlı ada tipli piksellerden oluşmaktadır. Test matrisleri hizalayıcı tümleştirici ile silikondan üretilmiş çıkış kartlarına basılmıştır.

28x28 μm^2 alana sahip dedektörlerde gerçekleştirilen elektriksel ve optiksel karakterizasyonlar, oda sıcaklığında yaklaşık 100 $\mu A/cm^2$ difüzyon dominant karanlık akım yoğunluğunun olduğunu göstermiştir. Piksellerin tepe tepkiselliği %62 kuantum

verimliliği sağlayacak şeklilde 1 A/W'dır. Piksellerin karanlık akım limitli tepe dedektivitesi yaklaşık olarak 1.17×10^{11} $cm\sqrt{Hz}/W$ 'dır.

Performans sınırlayan malzeme karakteristiklerini belirlemek üzere, dedektörler üzerinde Derin Seviye Geçici Spektroskopi ölçümleri gerçekleştirilmiştir. Ölçümler aktivasyon enerjisi, yakalama kesit alanı ve yoğunluğu sırasıyla 267 meV, 2×10^{-17} cm^2 ve 3×10^{13} cm^{-3} olan bir delik tuzağının olduğunu göstermiştir. Bahis konusu tuzak, izole malzeme kusurlarından kaynaklandığına işaret edecek şekilde genişletilmiş kusur özellikleri yansıtmamaktadır.

Anahtar Kelimeler: Cıva Kadmiyum Tellür (MCT), uzatılmış kısa dalga boyu kızılötesi (SWIR), Moleküler Işınlı Epitaksi (MBE)

To My Family

ACKNOWLEDGEMENTS

I would like to thank my thesis advisor Prof. Dr. Cengiz Beşikci for providing me the chance to use all opportunities of Quantum Devices and Nanophotonics Research Laboratory. Moreover I would like to express my gratitude for teaching me about HgCdTe material and MBE growth and assisting me during detector characterization.

I would like to thank Dr. Süleyman Umut Eker, Melih Kaldırım and Alp Tolungüç for sharing their knowledge about MBE growth technology, HgCdTe material and their invaluable comments, opinions and friendships. Special thanks to Melih Kaldırım for helping me during the characterization steps of HgCdTe photodiodes.

I would like to thank Nardin Avishan and Kübra Çırçır for their efforts to help me in Deep Level Transient Spectroscopy (DLTS) measurements.

I would like to thank Ayşe Şan and Berna Barutcu for sharing their knowledge and advices about fabrication processes.

I would like to thank Dr. Çağla Akgün and Esin Akça for their efforts to help me in the process of the substrate thinning.

I would like to thank ASELSAN for providing me the chance to work in such an equipped laboratory.

Last but not least, I would like to express my deepest love and gratitude to my wife for her endless support and motivation.

TABLE OF CONTENTS

LIST OF TABLES

LIST OF FIGURES

CHAPTER 1

INTRODUCTION

There is an increasing interest on the detectors sensing in the short wavelength infrared (SWIR) region. SWIR detectors benefit from natural light or laser illumination for detection. Unlike visible light, SWIR radiation can penetrate through fog and dust. Therefore SWIR detectors are able to show details which are hidden to visible detectors facilitating the utilization of these sensors in a wide application area.

SWIR imagers' working principle is different from that of thermal imaging sensors. SWIR thermal imagers use reflected light instead of the emitted light. SWIR detectors provide higher contrast and can show the scene behind the glass. In addition, SWIR detector materials have larger energy band gap. Hence the dark current is less than that of thermal imaging detectors operating in the mid and long wavelength infrared (MWIR and LWIR) bands. Thanks to the reduced dark current level, SWIR detectors can be operated with moderate or even without any cooling requirement.

Indium Gallium Arsenide ($In_xGa_{1-x}As$) is an optimal material choice in the SWIR band with 1.7 μm cut-off wavelength (x=0.53) for the military and civil applications such as remote sensing, night vision and astronomical applications, etc., since InGaAs detector structures can be grown with perfect uniformity and high quantum efficiency on (relatively) low cost indium phosphide (InP) substrates [1], [2]. On the other hand, $In_xGa_{1-x}As$ detectors have relatively high dark currents for extended wavelength SWIR

with nearly 2.5 μm cut-off wavelength (x~0.8) due to its large lattice mismatch to InP substrate that creates many dislocations degrading the diode performance.

Mercury Cadmium Telluride, HgCdTe is a common infrared detector material used in imaging applications in the MWIR and LWIR bands. Recently, it has started to be used in extended wavelength SWIR applications, since it has a tunable bandgap by adjusting the cadmium mole fraction for a wide range of wavelengths. Moreover, the lattice constant of HgCdTe is almost constant over the whole range of the wavelength. Hence, it is possible to tune the bandgap with negligible change in the lattice constant.

There are different methods to grow HgCdTe such as liquid phase epitaxy (LPE), molecular beam epitaxy (MBE), and metal organic chemical vapor deposition (MOCVD). MBE growth of HgCdTe is a challenging study, since the growth depends on lots of parameters affecting each other. Furthermore, the growth window of HgCdTe is narrow, therefore it is difficult to obtain HgCdTe layers with low defect density. Little change in composition corresponds to large difference in cut-off wavelength in MWIR and LWIR regions. On the other hand, the change is not so severe in the SWIR band. Hence it is important to keep composition constant as far as possible in MWIR and LWIR bands. All these concerns make MBE growth of HgCdTe difficult. However, the utilization of modern MBE systems have eliminated the uniform growth problem of HgCdTe in the SWIR, MWIR and LWIR bands.

This thesis reports the growth, fabrication and characterization of extended wavelength short wavelength infrared (SWIR) HgCdTe photodiodes. In situ doped HgCdTe layers were grown on home-polished CdZnTe substrates with MBE. X-ray diffraction, Fourier Transform Infrared Spectroscopy, Scanning Electron Microscopy, Deep Level Transient Spectroscopy and Hall Effect measurements were used to evaluate and optimize the growth conditions. Test pixel arrays consisting of 30 μm pitch pixels were fabricated and hybridized with silicon fan-outs. The pixel arrays were subjected to electrical and optical testing, and the results were compared with the recent studies.

This thesis consists of 4 chapters. Chapter I constitutes infrared background, HgCdTe material properties and growth technologies. Moreover a literature survey on InGaAs and HgCdTe in the SWIR band is given.

MBE growth of HgCdTe and test array fabrication are explained in Chapter II.

Chapter III gives the results and interpretation of electrical and optical characterizations, and compares the results with the state of the art studies.

Chapter IV is the concluding part where future work is also summarized

1.1 Basics of Infrared Detection

1.1.1 Infrared Radiation

In 1800, infrared radiation was first introduced by the Herschel's thermometer experiment. In order to measure the energy of the light, he used a monochromator to scatter light to its components and a thermometer as a detector. He concluded that the temperature increases when thermometer was exposed to the part of spectrum beyond red colored rays. He understood that the spectral components of light also include some form of invisible rays [3]. Indeed, infrared radiation is a form of radiated electromagnetic energy, satisfying the same laws for visible light, radio waves and x-rays [4].

Every object above absolute zero (0 K) emits electromagnetic radiation depending on the object temperature. For room temperature objects, the wavelength of the emitted radiation falls in the infrared region invisible to human eye, and hot objects emit radiation at shorter wavelengths.

1.1.2 Blackbody Radiation

Every object at any given absolute temperature above 0 K emits thermal radiation. Blackbody which absorbs all incoming radiation in all wavelengths is an ideal emitter which does not transmit or reflect the incoming radiation. For blackbodies, the emitted radiant power depends on only temperature. However for real matters an additional property, the emissivity (ε), comes into play [5]. Emissivity is the ratio of the total energy emitted by a matter at a temperature T to the total energy emitted by a blackbody at the same temperature T. Planck's law of blackbody radiation gives the spectral distribution of radiant exitance as [5],

$$M_{\lambda}(\lambda,T)=\frac{2\pi hc^{2}}{\lambda^{5}\left(e^{\frac{hc}{\lambda kT}}-1\right)}\left(\frac{W}{cm^{2}-\mu m}\right) \tag{1.1}$$

where λ is the wavelength of the radiation, c is speed of light in vacuum, h is Planck's constant, k is Boltzmann's constant, and T is the absolute temperature of the blackbody in Kelvin.

Figure 1.1 shows the spectral radiant exitance of a blackbody for different temperatures. As seen from Figure 1.1, when the temperature of the blackbody increases, the wavelength of the peak radiation becomes shorter. Furthermore, the total exitance reflected by the area under the curves increases much faster than the blackbody temperature. This can easily be seen from Stefan-Boltzmann law given in Equation (1.2), that is obtained by integrating Planck's Law from λ=0 to λ=∞ [5],

$$M(total)=\sigma T^{4}\left(W/cm^{2}\right) \tag{1.2}$$

where σ is the Boltzmann constant.

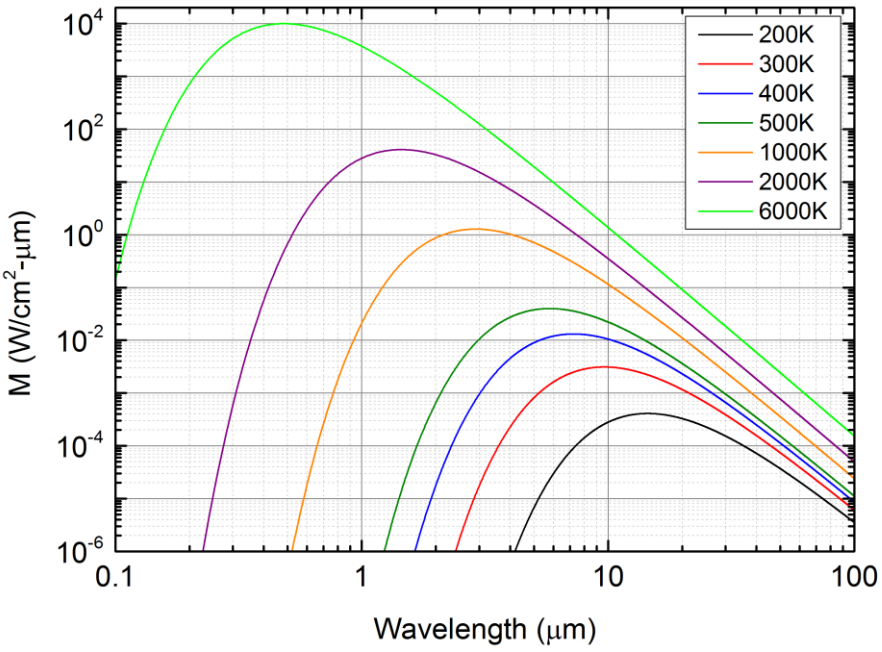

Figure 1.1 Spectral radiant exitance of a blackbody for different temperatures.

The peak radiation wavelength is given by Wien's Displacement Law, which is obtained by differentiating Planck's Law yielding [5],

$$\lambda_{max}(\mu m) = \frac{2898\,\mu m.K}{T(K)} \tag{1.3}$$

1.1.3 Atmospheric Transmission

The radiation emitted or reflected from the objects and backgrounds must propagate through the atmosphere in order to reach imaging systems. Hence, the attenuation of the atmosphere should be taken into account for the detection of infrared light. Since the atmosphere is also a source of radiation, it creates background while detecting the target. Moreover, it weakens the incoming radiation in two ways, namely absorption and scattering [5].

Molecules such as NO, CO, CO_2, CH_4 and H_2O are able to absorb infrared radiation at some specific wavelengths [5]. The size of these molecules is smaller than the wavelength of the radiation [6]. Therefore, the transmission of infrared radiation through atmosphere at these wavelengths is very poor. The absorption of H_2O (water vapor) is one of the main factors affecting the performance of the detector systems, since the concentration of the water vapor is varying with geographical condition and weather. As a result of the absorption of the atmosphere, certain bands in the infrared region are formed as indicated in Table 1.1. Figure 1.2 shows the atmospheric transmission spectrum and the molecules responsible for absorption lines.

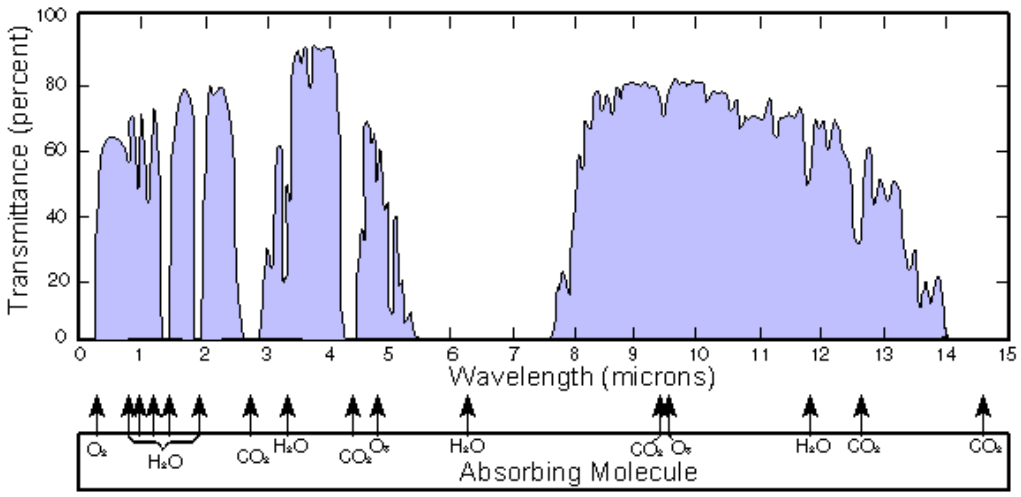

Figure 1.2 Atmospheric transmission spectrum and respective molecules responsible for absorption [7].

As seen from Figure 1.2, the atmosphere is relatively transparent at some wavelengths. This is known as 'atmospheric transmission windows'.

Table 1.1 Atmospheric Transmission Windows.

Infrared Region	Wavelength range (μm)
Near Infrared (**NIR**)	0.7 – 1.5
Short Wavelength Infrared (**SWIR**)	1.5 – 3
Mid Wavelength Infrared (**MWIR**)	3 – 5
Long Wavelength Infrared (**LWIR**)	8 – 12
Very Long Wavelength Infrared (**VLWIR**)	12 – 25
Far Infrared (**FIR**)	Longer than 25

Another effect of the atmosphere is scattering. There are two kinds of scattering mechanism, namely Mie scattering and Rayleigh scattering. Mie scattering is scattering of radiation by particles with a larger size than the wavelength. Scattering is independent of wavelength for larger particles. It is difficult to estimate the attenuation by this scattering mechanism, since the concentration, size distribution and characteristics change with location, time and other environmental conditions. Rayleigh scattering is scattering of radiation by particles with a smaller size than the wavelength and it is inversely proportional to λ^4. As a result, for wavelengths longer than 2 μm, scattering by gas molecules is negligible. Moreover IR radiation can

penetrate through smoke and mist unlike visible radiation, since smoke and mist particles are usually small compared with IR wavelengths. The infrared wavelengths are much larger than the gas molecules. As a result Rayleigh scattering is negligible for IR bands where visible spectrum suffers from it. On the other hand, Mie scattering may be significant depending on the weather conditions [8].

Since the peak radiant power emitted by near room temperature targets is in the range of 3 – 12 μm wavelength, MWIR and LWIR infrared regions are widely used for thermal imaging. LWIR is usually preferred when high performance is required, since LWIR detectors have higher sensitivity to objects at ambient temperature, and long wavelength infrared radiation can penetrate through mist and smoke better. However, MWIR is usually preferred when compact camera systems are needed. In addition to those differences, MWIR band requires smaller size optics, and absorption by water vapor is less in the MWIR band compared to the LWIR band.

Summarizing the infrared regions, MWIR and LWIR infrared regions are different in terms of background flux, scene characteristics, thermal contrast and atmospheric transmission under severe weather conditions. According to these differences, LWIR is usually preferred for low humidity and cold environments. Moreover LWIR is also used under battlefield conditions due to longer penetration of radiation [9].

1.2 Infrared Detectors

Infrared detector is a kind of transducer that converts infrared radiation into electrical signals. It plays an important role for an IR imaging system. The quality of this conversion determines the performance of the imaging system. Infrared detectors can be divided into two groups: thermal and photon detectors.

1.2.1 Thermal Detectors

Thermal detectors can be treated as two-step transducers. First, the incident radiation is absorbed to change the temperature of the material. This temperature change causes a change in the physical property of the material, and then an electrical signal is generated according to this change. In other words, the temperature is increased by incident IR radiation, and the changes in temperature are sensed by a temperature

dependent mechanism, such as thermoelectric voltage, resistance, and pyroelectric voltage [5], [10].

The main advantage of the thermal detectors is the ability of working without cooling. Although cryogenic cooling is not a requirement, isolation of the thermal detectors from the ambient temperature fluctuations is usually required. They are quite slow in response time when compared with photon detectors. Moreover, thermal detectors are not spectrally selective. On the other hand, they are reliable and low-cost detectors which make them useful for most of the civil applications. Bolometer is the most commonly used thermal detector.

Bolometers: The electrical resistance of the material is changed because of the temperature increase caused by the incident radiation. When bias is applied between the terminals, current flowing through the bolometer increases or decreases depending on the temperature change. Bolometer has a thin metal or semiconductor film as an absorbing layer. The most popular thermistor material used is vanadium dioxide, VO_2 [3]. A micro bolometer can be seen from Figure 1.3.

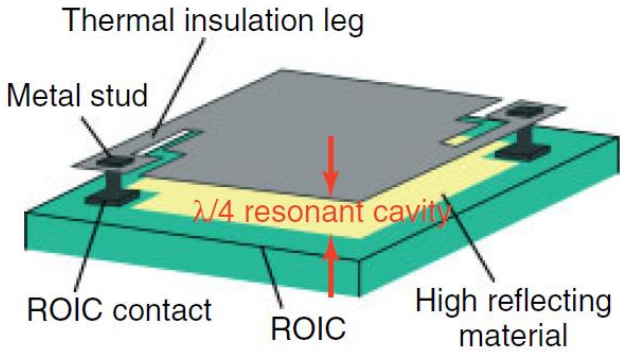

Figure 1.3 A bolometer FPA [3].

As shown in Figure 1.3, there is a quarter wave resonant cavity between the bolometer and the substrate. For wavelengths near 10 μm, this cavity behaves as a reflector.

Pyroelectric Detectors: This type of detector contains certain dielectric materials with low crystal symmetry. When the material is heated via IR radiation, the electrical polarization is changed, and as a result surface charge is created. When the incident radiation is modulated using a chopper, an alternating current is generated, and this

current is sensed for imaging. Pyroelectric detectors are generally required to be worked with optical modulator for chopping or defocusing the incoming radiation [3].

Thermocouples and thermopiles: These thermoelectric structures have one or more junctions between two metals. A thermocouple generates thermo-electric emf when it is heated. Thermopiles include a group of thermocouples connected in series in order to increase thermo-electric emf. Thermocouples use the Seebeck effect that is the induction of voltage because of thermal gradient across a conductor. Utilization of higher Seebeck coefficient materials provides higher sensitivity [11].

1.2.2 Photon Detectors

Photon detectors use the absorption of radiation resulting from the interaction of electrons with incident photons. There are three main electron excitation processes that may be exploited in photon detectors, being (i) intrinsic absorption across the fundamental bandgap, (ii) extrinsic absorption by carriers in an impurity level, and (iii) absorption of photon energy by free carriers in the conduction band. These processes are shown in Figure 1.4. Photon detectors have small response time and high detectivity. Moreover, the responsivity depends on the wavelength facilitating the production of dual/multi-band sensors.

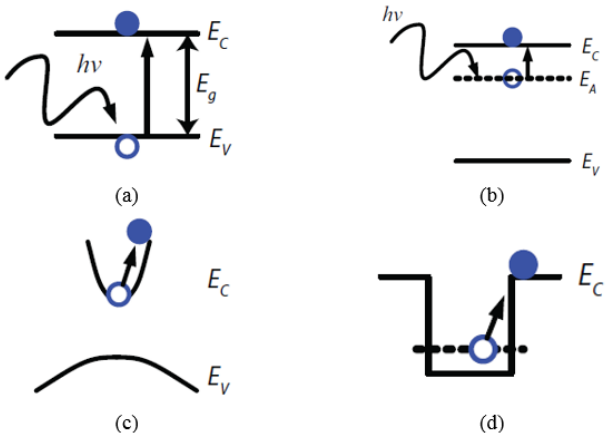

Figure 1.4 Fundamental optical excitation processes in semiconductors; (a) intrinsic absorption, (b) extrinsic absorption, (c) free carrier absorption, (d) quantum absorption. The notation *hν* denotes the energy of a single photon, while E_c and E_v represent the conduction band and valance band edges, respectively [12].

In extrinsic detectors, photon-electron interaction occurs from impurity states to either the conduction band or the valance band. The detection wavelength is limited according to the energy level of the doped impurities. All of the extrinsic detectors operate as a photoconductor [13]. Those detectors should be operated at lower temperatures than intrinsic detectors' temperature in order to reach the same performance.

For the intrinsic type detectors, the photon-electron interaction occurs across the band gap of the detector material, which provides a limit for detection wavelength. If the incident photon energy becomes lower than the energy band gap of the detector material, then the response of the detector drops very rapidly. According to the electrical output of the detector, we can divide intrinsic type detectors into two groups; photoconductive and photovoltaic [13].

1.2.2.1 Photoconductive Detectors

Photoconductive devices operate according to photo-generation of charge carriers. Basic operation of a photoconductor can be seen from Figure 1.5. When the incident photon is absorbed by the detector material, the conductivity of the material increases because of the photo-generated charge carriers. Indeed absorption increases the number of free carriers by exciting electrons from valance band to conduction band, therefore the conductivity changes. Note that the energy of the incident photons must exceed the bandgap of the semiconductor. One should apply enough bias to avoid the recombination of the photo-generated charge carriers. Since this type of detectors require large bias and current levels, they are unsuitable for dense focal plane arrays even though these detectors may yield high responsivity.

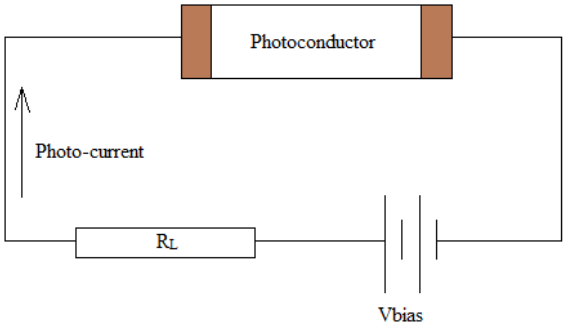

Figure 1.5 Basic operation of a photoconductor. An external bias is required to sweep the photo-generated carriers to the contacts.

1.2.2.2 Photovoltaic Detectors

Another type of intrinsic photodetector is photovoltaic detector which is the most widely used optical sensor. This type of detector has an internal potential barrier with a built-in Electric field. The photo generated charge carriers move in opposite directions due to the built-in E-field. The separated electrons and holes give rise to current flow in an external circuit. The potential barrier can be formed by the use of p-n junctions, heterojunctions, Schottky barriers and metal-insulator-semiconductor (MIS) photo-capacitors. The most important and widely used example of a photovoltaic detector is a photodiode that is simply a p-n junction [13], [14]. Incident radiation excites electrons and generates electron-hole pairs in n and p type regions. Photo-generated electrons and holes diffuse towards the junction and are swept to opposite directions due to the electric field in the depletion region.

The magnitude of generated photocurrent is

$$I_{ph} = \eta q A \Phi \tag{1.4}$$

where η is the quantum efficiency, q is the electron charge, A is the area of photodiode, and Φ is the incident photon flux density. Quantum efficiency is defined as the ratio of number of generated electron hole pairs to the number of incoming photon.

1.2.2.3 Photoconductive versus Photovoltaic Detectors

For high density staring arrays, photovoltaic detectors are usually preferred because of lower power dissipation and higher impedance that is better matched to high-input impedance silicon readout circuitry. Moreover, the maximum detectivity of photovoltaic detectors is higher than that of photoconductive detectors theoretically.

1.2.2.4 Quantum Well Infrared Photodetectors

The last type of photon detectors is quantum detectors such as quantum well infrared photodetectors (QWIPs) and quantum dot infrared photodetectors (QDIPs). These detectors use carrier transition from/to quantized levels which are formed as a result of narrower bandgap materials such as GaAs encapsulated by wider bandgap materials such as AlGaAs on a scale comparable to the electron wavelength within the material. Although QWIPs suffer from lower quantum efficiencies and lower operating temperatures, the excellent uniformity, pixel operability, thermal cycling stability and lower cost offer important advantages for focal plane array applications.

1.2.3 Comparison of Thermal and Photon Detectors

Low cost thermal detectors such as bolometers are mostly preferred in applications where high sensitivity and speed are not important, yet they are easy to use and inexpensive, since they do not need cooling, i.e. thermal detectors can work at room temperature. High sensitivity and high-speed infrared detectors can be achieved by photovoltaic, photoconductor or QWIP detectors. However they are required to be cooled down to cryogenic temperatures.

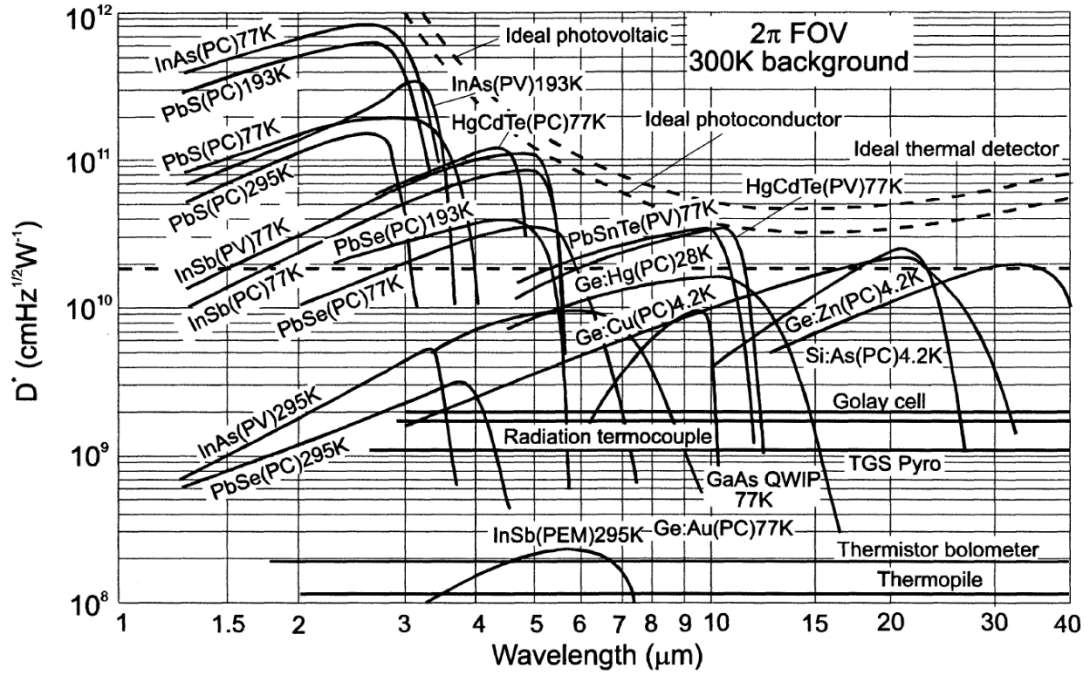

Figure 1.6 The detectivity (D^*) of various commercially available infrared detectors when operated at the indicated temperature. Theoretical curves for D^* for ideal photovoltaic, photoconductive and thermal detectors are also shown [15].

As we can see from Figure 1.6, ideal photovoltaic detectors have a higher specific detectivity D^* than ideal photoconductor or thermal detectors. D^* is one of the main characterizing parameter, and is explained later in this chapter. The detectivity of the thermal detectors has a weak dependence on the temperature unlike photon detectors.

1.3 Figures of Merit

1.3.1 Responsivity

A detector is a perfect tool converting incoming radiant power to an output signal in the form of photocurrent or photovoltage. Responsivity is the ratio of the output signal to the incident radiant power falling on the detector.

$$\text{Responsivity}(R) = \frac{\text{signal output (A or V)}}{\text{total power received by detector (W)}} \tag{1.5}$$

In terms of quantum efficiency responsivity can be expressed as;

$$R = \frac{I_{photo}}{\phi} = q\eta \frac{g}{h\nu} = q\eta g \frac{\lambda}{hc} = \eta g \frac{\lambda}{1.24} \ (A/W) \tag{1.6}$$

where g is the photoconductive gain which is 1 for photovoltaic detectors, h is the Planck constant, c is the speed of light in vacuum and λ is the cut-off wavelength of the detector.

1.3.2 Noise

Noise can be explained as undesired fluctuations in the measured signal. It is impossible to completely remove noise, yet may be kept at a minimum level. When noise affects the output, it can hide small signals as seen from Figure 1.7.

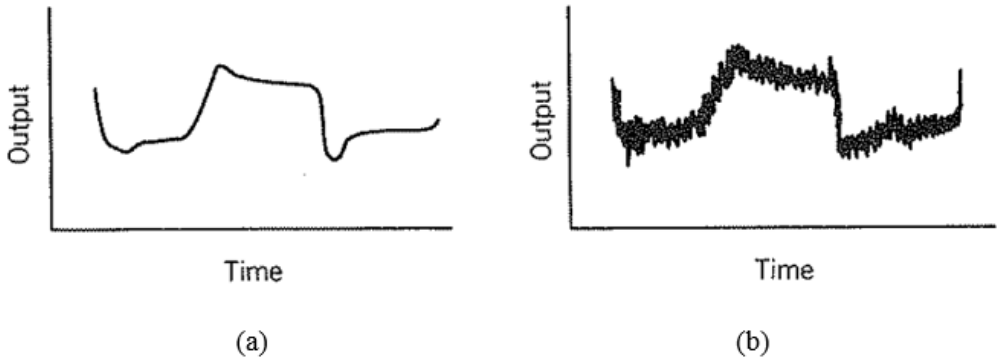

Figure 1.7 Signal (a) with low noise; (b) with more noise [4].

Some noise components are inherent that cannot be removed. Fundamental noise can be divided into four groups; Johnson (Nyquist or Thermal) noise, capacitor noise, shot noise and 1/f noise.

Johnson (Nyquist or Thermal) Noise

When the temperature is above 0 K, thermal fluctuations exist. As a result, thermal noise is observed in a conductor which is expressed as [6],

$$V_n(rms) = \sqrt{4kTR\Delta f} \tag{1.7}$$

$$i_n(rms) = \sqrt{\frac{4kT\Delta f}{R}} \tag{1.8}$$

where k is the Boltzmann constant, T is the temperature, R is the dynamic resistance, and Δf is the measurement bandwidth.

Capacitor (kTC) Noise

Noise voltage arising from the capacitor noise is expressed as,

$$V_n(rms) = \sqrt{\frac{kT}{C}} \tag{1.9}$$

where k is the Boltzmann constant, T is the temperature, and C is the capacitance.

Shot (Photon) Noise

Both photons and charge carriers are quantized. Neither an electron nor a photon can be divided. In the context of photon detection, a photon either excites an electron or not. The fluctuated arrival rate of photons causes shot noise. It may also occur in a p-n junction diode where the photo generated carriers must cross a potential energy barrier in order to be detected [16]. Shot noise is replaced by generation-recombination noise in devices such as photoconductors that lack of the potential energy barrier. Shot noise is zero in devices that have a zero current flow, such as an open circuit photovoltaic detector. It means that in order to observe shot noise, a bias voltage must be applied to the detector. In that sense it differs from thermal noise. The noise current is given by

$$i_n(rms) = \sqrt{2qI\Delta f} \tag{1.10}$$

where q is the electron charge, I is the total current flowing through the diode, and Δf is the measurement bandwidth.

1/f (Pink) Noise

The power spectral density of 1/f noise is inversely proportional to the frequency. It causes fluctuations in the signal over wide range of frequencies limiting the low frequency detectivity [6].

1.3.3 Noise Equivalent Power

Knowledge of the noise performance of a detector can be obtained via the signal to noise ratio (SNR) which is calculated when the amount of incident radiant power is known. The noise equivalent power (NEP) is the amount of flux which creates an output signal equals to the rms value of the noise. In other words, NEP is the amount of radiation flux required to produce SNR=1. NEP can be expressed by,

$$NEP = \frac{\phi}{S/N} = \frac{v_{noise}}{R_v} = \frac{i_{noise}}{R_i} \tag{1.11}$$

1.3.4 Specific Detectivity

The specific detectivity, D^* is generally used to specify the performance of a detector. NEP is enough for predicting the minimum detectable power. A good detector has a small NEP, yet the size of the detector should be indicated when specifying NEP. Since NEP depends on the area of the detector. The specific detectivity eliminates this drawback [4]. D^* is inversely proportional to the NEP, this means that good detectors have high D^*. Note that D^* is independent of detector area and bandwidth. Because NEP is also proportional to detector area and bandwidth, i.e. $\sqrt{A_D \Delta f}$. Specific detectivity is given by,

$$D^* = \frac{\sqrt{A_D \Delta f}}{NEP} = \frac{\sqrt{A_D \Delta f}}{\phi}\frac{S}{N} = \frac{\sqrt{A_D \Delta f}}{v_{noise}}R_v = \frac{\sqrt{A_D \Delta f}}{i_{noise}}R_i \tag{1.12}$$

where A is the area of the detector, Δf is the measurement bandwidth, and R is the responsivity.

1.3.5 Noise Equivalent Temperature Difference

There is a minimum temperature difference between background and the target object to produce an output signal equivalent to the system noise. This minimum temperature is called as noise equivalent temperature difference (NETD). In other words, NETD is the minimum temperature difference in field of view to produce signal to make SNR=1. NETD is expressed as,

$$NETD = \frac{(4F/\#^2 + 1)\sqrt{\Delta f}}{\sqrt{A_D}\int_0^\infty T(\lambda) D^*(\lambda) \frac{dM_{target}(\lambda)}{dT} d\lambda} \quad (1.13)$$

where F/# is the f number which is expressed as the focal length of the lens divided by the aperture diameter, Δf is the measurement bandwidth, A is the detector area, $T(\lambda)$ is the wavelength dependent atmospheric transmission, D^* is the specific detectivity and M is the target spectral exitance.

1.3.6 Noise Equivalent Irradiance

Noise Equivalent Irradiance also called as Noise Equivalent Flux Density, is the flux density in order to make signal to noise ratio 1. NEI depends on integration time, therefore NEI calculations should be given with integration time. NEI is expressed as,

$$NEI = \frac{NEP}{A_d} = \frac{\sqrt{\Delta f}}{D^*\sqrt{A_d}} \quad (1.14)$$

where A_d is the detector area and Δf is the bandwidth. NEI can be expressed in W/cm^2 or photons/(cm^2-s).

1.4 HgCdTe Material and Properties

$Hg_{1-x}Cd_xTe$ (mercury cadmium telluride, MCT) is a II-VI semiconductor alloy formed from the binary compounds, CdTe (cadmium telluride) and HgTe (mercury telluride). In $Hg_{1-x}Cd_xTe$ 'x' and '1-x' indicate the mole fractions of CdTe and HgTe in the alloy, respectively. Due to the advantageous properties of MCT which is introduced in further sections, it is the choice of material for the majority of high performance IRFPA systems fielded in SWIR, MWIR and LWIR applications [17].

1.4.1 HgCdTe History

MCT material studies have been documented from 1970 to the present. Studies before 1970 were not published in detail because of the military issues. However, it does not mean that there was no study on MCT before 1970. The first studies on mixtures of HgTe and CdTe was reported by W.D. Lawson et al. at the Royal Radar Establishment in England in 1958 [10]. They mixed HgTe and CdTe with different fractions to obtain

HgCdTe, and they concluded that it is possible to change the bandgap value of HgCdTe between the bandgap values of CdTe and HgTe [18]. HgCdTe has been studied for 56 years, and the technology can be divided into three groups; namely first, second and third generation of infrared detectors. The first generation of infrared detectors consists of photoconductive linear arrays which have been produced in large quantities, and are still in use. The second generation consists of photovoltaic two dimensional arrays which are today in high production rate. The third generation covers the new detector technologies including dual/multi-band sensors and detectors with improved capabilities and performance with smaller pitch and elevated operation temperature.

1.4.2 Crystal Structure and Lattice Parameter

Compared to covalently bonded III-V materials, HgCdTe bonding is more ionic resulting in a soft, brittle and fragile material. The $Hg_{1-x}Cd_xTe$ alloy system has a zinc blende crystal structure which is in the form of two interpenetrating face centered cubic lattices (FCC) displaced along their body diagonal by a quarter of their length, where one FCC cell contains Te atoms and the other, Cd and Hg atoms [12]. As seen from Figure 1.8, the smaller red atoms represent the random distribution of Cd and Hg atoms in a mean proportion of mole fraction, while the larger purple atoms represent the Te atoms.

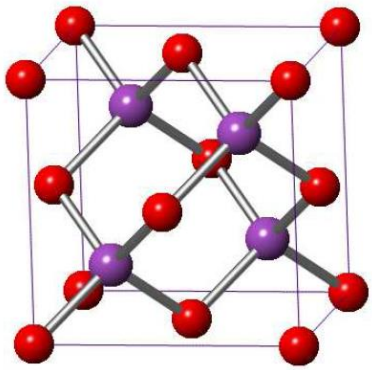

Figure 1.8 Unit lattice of HgCdTe crystal indicating the Te cations (larger purple atoms) and Cd and Hg anions (smaller red atoms) lattice sites [12].

Each cation (Cd or Hg) is tetrahedrally coordinated with four nearest neighbor anions (Te) and etc. The bonding is a mix of covalent and ionic bonding depending on the

degree of difference in electronegativity between the anions and the cations [12]. There are five possible selections of the Cd and Hg as nearest neighbors to the Te ion [10]:

- 4 Cd ions
- 4 Hg ions
- 2 Cd ions and 2 Hg ions
- 3 Cd ions and 1 Hg ion
- 3 Hg ions and 1 Cd ion

These five structures occur randomly throughout the $Hg_{1-x}Cd_xTe$ alloy in a perfect crystal [10]. As seen from Figure 1.9 the lattice mismatch between HgTe and CdTe is very small with the lattice constants of CdTe and HgTe being about 6.4825 °A and 6.4614 °A at room temperature, respectively.

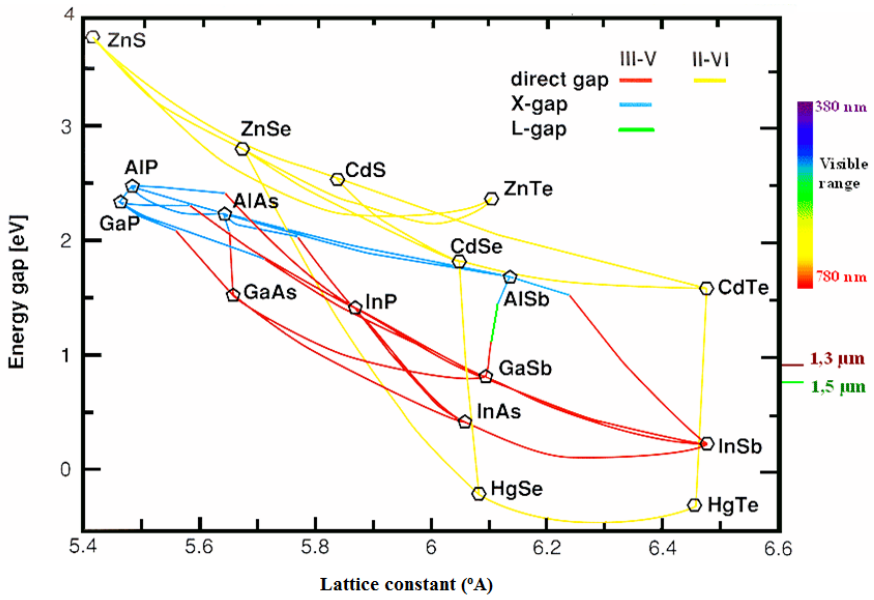

Figure 1.9 Lattice constant vs energy gap of some semiconductors and semimetals at room temperature [19].

The expression for the variation of lattice parameter, α , with the composition, x , at room temperature which was proposed by Higgins et al. is [20]:

$$a(x) = 6.4614 + 0.0084x + 0.016x^2 - 0.0057x^3 \quad (\text{Å}) \tag{1.15}$$

where α is lattice constant, and x is Cd mole fraction. Equation (1.15) is plotted in Figure 1.10. As seen from this figure, the lattice constant of CdTe (x=1) is only 0.3% larger than that of HgTe (x=0). This is so important since it allows the utilization of HgCdTe in the entire IR spectrum with a small change of lattice constant. At this point it should be noted that lattice constant depends also on temperature. Brice expressed the variation of lattice constant with respect to temperature as follows [20]:

$$a(T) = a(300\mathrm{K}) + B(T) \quad (\mathrm{\AA}) \tag{1.16}$$

where α(300K) is the lattice constant at room temperature and B(T) has the values given in Table 1.2 [20]. Figure 1.11 shows the lattice constant of HgCdTe with respect to temperature.

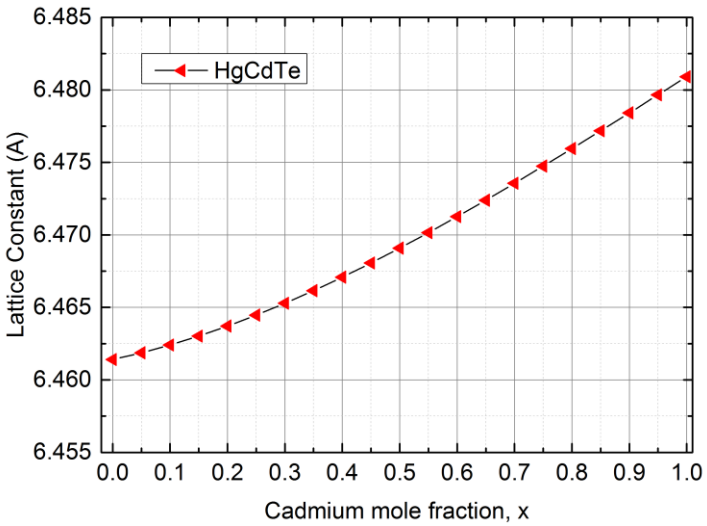

Figure 1.10 Lattice parameter of $Hg_{1-x}Cd_xTe$ as a function of composition at room temperature.

Table 1.2 Lattice parameter correction factor $B(T)$ in Equation (1.16)

T	100	200	300	400	500	600	700	800
B(T)	-0.007	-0.004	0.0	0.003	0.006	0.01	0.014	0.019

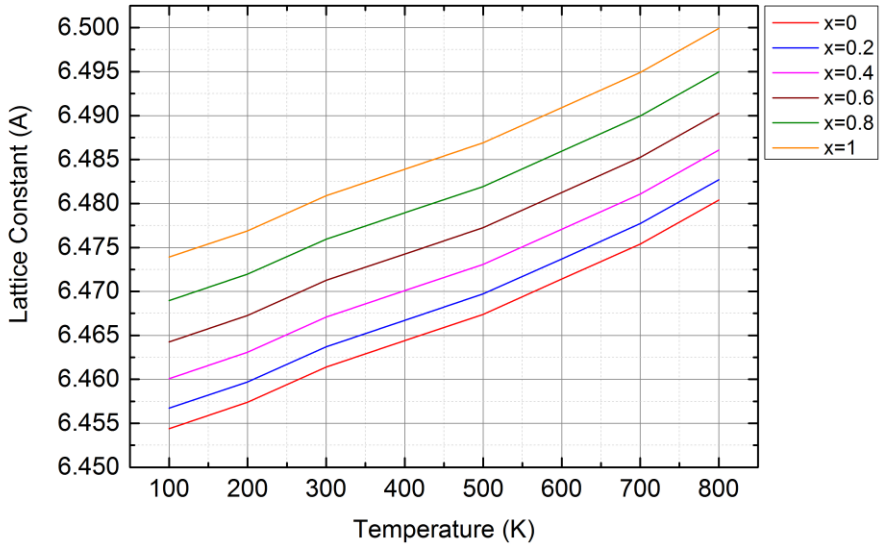

Figure 1.11 Lattice parameter of $Hg_{1-x}Cd_xTe$ as a function of temperature.

1.4.3 Energy Bandgap

CdTe is a semiconductor, whereas HgTe is a negative bandgap material with the conduction band edge lying below the valance band edge. HgTe and CdTe are fully miscible, and $Hg_{1-x}Cd_xTe$ alloy of these compounds can be obtained for the whole composition range [20]. As the cadmium concentration is decreased, the bandgap of the alloy approaches to zero. There exist some equations in literature expressing the bandgap of $Hg_{1-x}Cd_xTe$ in terms of cadmium mole fraction and temperature. One commonly used expression by Laurenti et al. is [20]:

$$E_g = -0.303(1-x) + 1.606x - 0.32x(1-x) + [6.3(1-x) - 3.25x - 5.92x(1-x)] \times 10^{-4} T^2 / (11(1-x) + 78.7x + T) \quad (1.17)$$

where E_g is the energy bandgap of $Hg_{1-x}Cd_xTe$ in electron-volts (eV), x is Cd mole fraction, and T is the temperature in Kelvin. This equation can be applied to HgCdTe with compositions larger than 0.4. Equation (1.17) is plotted in Figure 1.12 for three temperatures; 77K, 120K and 300K.

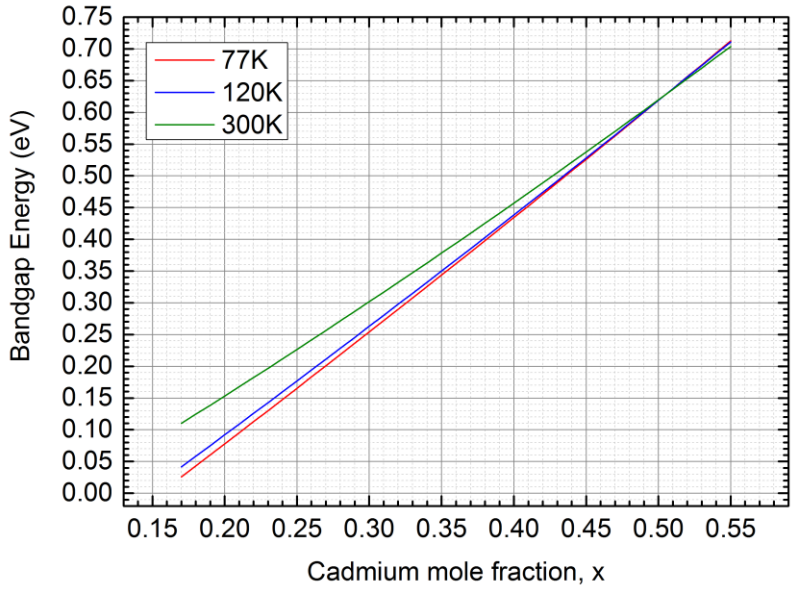

Figure 1.12 Bandgap energy of $Hg_{1-x}Cd_xTe$ as a function of cadmium mole fraction, x for three temperatures.

Cut-off wavelength can be calculated from the energy bandgap values by using the Equation (1.18) and it is plotted in Figure 1.13. Cut-off wavelength is expressed as the maximum wavelength of incoming infrared radiation absorbed by the detector material. It is given by,

$$\lambda_{cut-off}(\mu m) = \frac{1.24}{E_g(eV)} \tag{1.18}$$

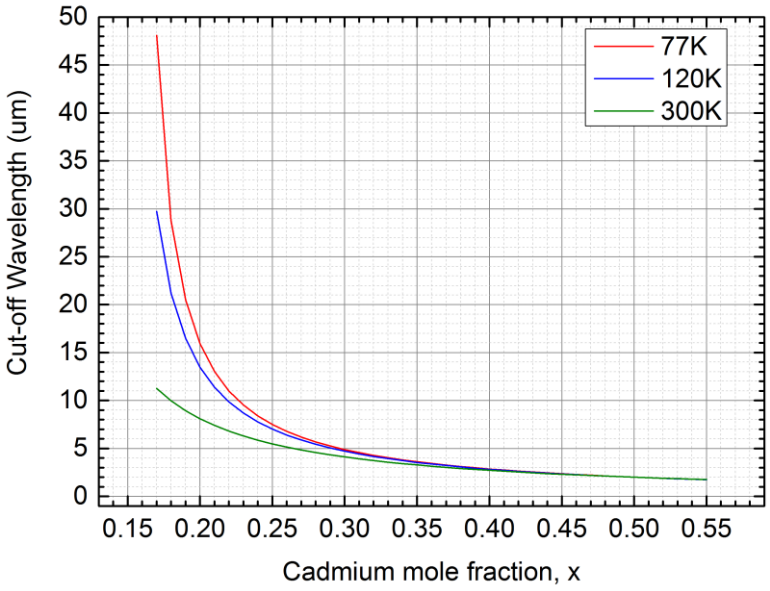

Figure 1.13 Cut-off wavelength of $Hg_{1-x}Cd_xTe$ as a function of cadmium mole fraction, x for three temperatures.

It is possible to adjust energy bandgap of $Hg_{1-x}Cd_xTe$ from 0.7 μm ($x \approx 1$) to 25 μm ($x \approx 0.18$ at 77K). However, when Figure 1.13 is examined carefully, one can observe that cut-off wavelength strongly depends on cadmium mole fraction for high cut-off wavelength values. As a result of this dependence, a small change in targeted 'x' value causes a relatively large variation in the cut-off wavelength which makes it difficult to control composition uniformly.

1.4.4 Intrinsic Carrier Concentration

An empirical formula for the intrinsic carrier concentration, $n_i(cm^{-3})$ of $Hg_{1-x}Cd_xTe$ as a function of cadmium mole fraction, *x*, temperature and bandgap given by Hansen and Schmit [12] is:

$$n_i = (5.585 - 3.82x + 0.001753T - 0.001364xT) \times 10^{14} \times E_g^{3/4} \times T^{3/2} \times \exp\left(-\frac{E_g}{2kT}\right) \quad (1.19)$$

where k is the Boltzmann constant (8.617e-5 $eV\text{-}K^{-1}$). Equation (1.19) is valid for composition x ranging from 0.16 to 0.4 and for a temperature range $50 < T < 300$ K.

Equation (1.19) is plotted in Figure 1.14. As seen from Figure 1.14, at a given temperature, n_i decreases with increasing x.

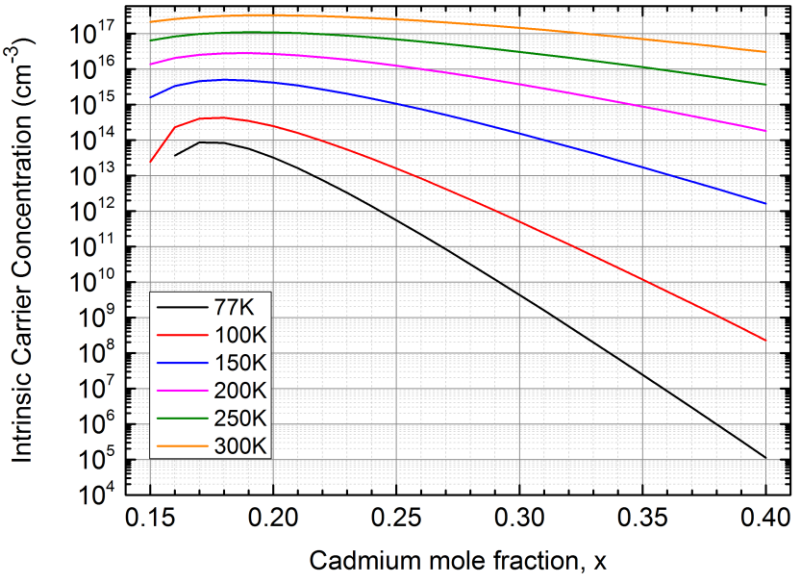

Figure 1.14 Intrinsic carrier concentration of $Hg_{1-x}Cd_xTe$ as a function of cadmium mole fraction, x, for different temperatures.

1.4.5 Mobility

The mobility of an electron can be described by how easily the carrier can move through the lattice. The main factors affecting the mobility of a carrier are the carrier effective mass and the average time between lattice/impurity collisions [12]. These collisions are a result of various scattering processes which are inherent to the material and other non-fundamental scattering processes due to defects in the crystal lattice, all of which act to reduce the mobility [12]. The electron mobilities in HgCdTe is high due to the small effective mass, while heavy-hole mobilities are about two orders of magnitude lower. The *x*-dependence of the mobility is due to *x*-dependence of the bandgap, and the temperature dependence is due to temperature dependence of various scattering mechanisms [21].

An empirical expression for the electron mobility ($cm^2V^{-1}s^{-1}$) in $0.2 \leq x \leq 0.6$ and $T > 50$ K given by Rosbeck et al. is [12]:

$$\mu_e = \frac{9\times10^8 b}{T^{2a}}, \quad \text{where} \quad a = \left(\frac{0.2}{x}\right)^{0.6}, \quad b = \left(\frac{0.2}{x}\right)^{7.5} \tag{1.20}$$

where μ_e is the mobility, x is the cadmium mole fraction and T is the temperature in Kelvin. Electron mobility is plotted in Figure 1.15 according to Equation (1.20).

The hole mobility is generally evaluated with assuming that the electron to hole mobility ratio $b = \mu_e / \mu_h$ is constant and equal to 100 [21].

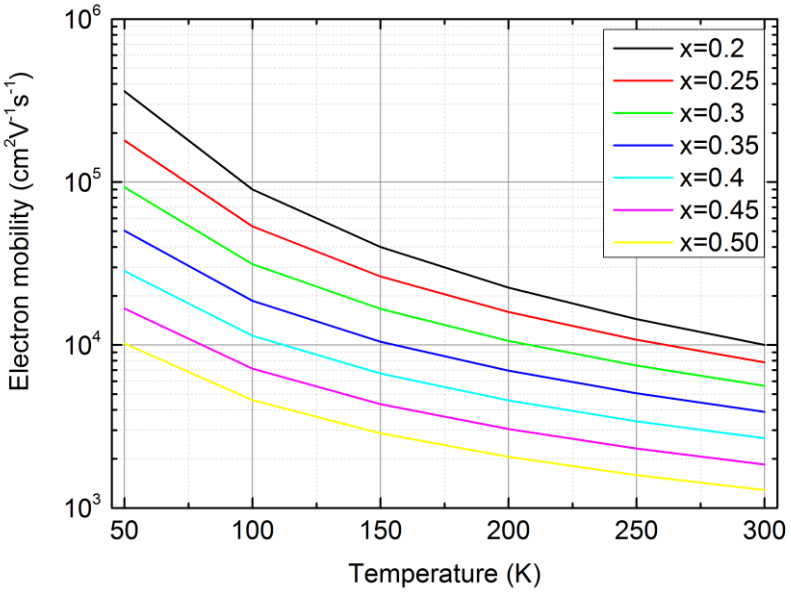

Figure 1.15 Electron mobility as a function of temperature for different compositions.

1.4.6 Carrier Lifetimes

An important electrical parameter of determining the performance and upper limit of various detector parameters such as the quantum efficiency, responsivity, dark current and noise is the photo-generated minority carrier lifetime in HgCdTe [12], [21]. It defines the average time that an excess minority carrier exists before it recombines. In n-type (p-type) HgCdTe, excess holes (electrons) recombine with majority carrier electrons (holes). Therefore the lifetime of these excess minority carriers is a direct measure of the average bulk lifetime of excess photo-generated minority carriers. There are three dominant recombination processes in HgCdTe that limit this lifetime; radiative, Auger and Shockley-Read-Hall recombination [22]. The first two

recombination mechanisms are intrinsic to the material band structure, whereas the Shockley-Read-Hall mechanism is a result of crystal imperfections and impurities. [21], [22]. The net lifetime of excess carriers is [10]:

$$\frac{1}{\tau_{net}} = \frac{1}{\tau_R} + \frac{1}{\tau_A} + \frac{1}{\tau_{SRH}} \tag{1.21}$$

where τ_R, τ_A ,τ_{SRH} are the radiative, Auger and Shockley-Read-Hall lifetimes, respectively. Another important factor affecting the minority carrier lifetime is HgCdTe surface. Recombination rates at the various surfaces are usually much higher than the recombination rate in the bulk due to the presence of interface traps [12]. Taking into consideration recombination at the HgCdTe/surface and HgCdTe/substrate interface, modeled by a surface recombination velocity parameter S (cm s^{-1}), the net effective lifetime, τ_{eff} can be defined as [10]:

$$\frac{1}{\tau_{eff}} = \frac{1}{\tau_{net}} + \frac{2S}{d} \tag{1.22}$$

where d is the thickness of the HgCdTe layer. Note that Equation (1.22) assumes that the back and front surface recombination rates are same.

1.4.6.1 Radiative Recombination

When an electron in the conduction band recombines with a hole in the valance band, an excess energy is generated, and this energy is given as a photon [10]. The recombination rate depends on the concentration of electrons in the conduction band and the availability of holes in the valance band. The process is illustrated in Figure 1.16.

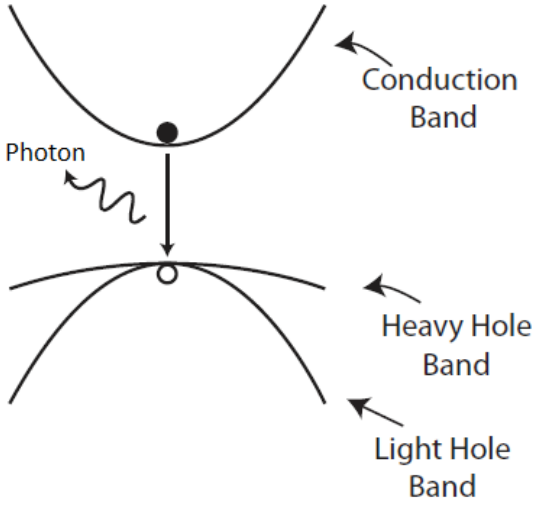

Figure 1.16 Radiative recombination process [12].

Radiative recombination lifetime developed by Schacham and Finkman can be expressed as [22]:

$$\tau_R = \frac{n_i^2}{(n_0 + p_0)G_R} \quad \text{in seconds} \tag{1.23}$$

where n_i is the intrinsic carrier concentration, n_o and p_o are the electron and hole concentration respectively, and G_R is the thermal equilibrium spontaneous generation rate (cm^{-3}-sec^{-1}). G_R is expressed as in Equation (1.24) [22]:

$$G_R = n_i^2 5.8 \times 10^{-13} \varepsilon_\infty^{1/2} \left(\frac{m_0}{m_e^* + m_h^*} \right)^{3/2} \left(1 + \frac{m_0}{m_e^*} \right) \left(\frac{300}{T} \right)^{3/2} [E_g^2 + 3kTE_g + 3.75(kT)^2] \tag{1.24}$$

where ε_∞ is the high frequency dielectric constant, m_e^* and m_h^* are the electron and hole effective masses, respectively, and m_o is the electron rest mass (kg), k is Boltzmann constant (eV K^{-1}).

1.4.6.2 Auger Recombination

There are two dominant types of Auger recombination, Auger-1 and Auger-7 recombination processes. The dominant recombination mechanism for n-type material is Auger-1. It can be explained as following. An electron in the conduction band recombines with a hole in the valance band. This recombination creates excess energy,

and this energy is transferred to another electron in the conduction band. Due to that excess energy, this acceptor electron is excited to a higher energy level in the conduction band. The dominant recombination mechanism for p-type material is Auger-7, which can be explained as following. An electron in the conduction band recombines with a hole in the valance band, and the created excess energy excites another hole in the valance band into a higher energy state as illustrated in Figure 1.17 [10], [20].

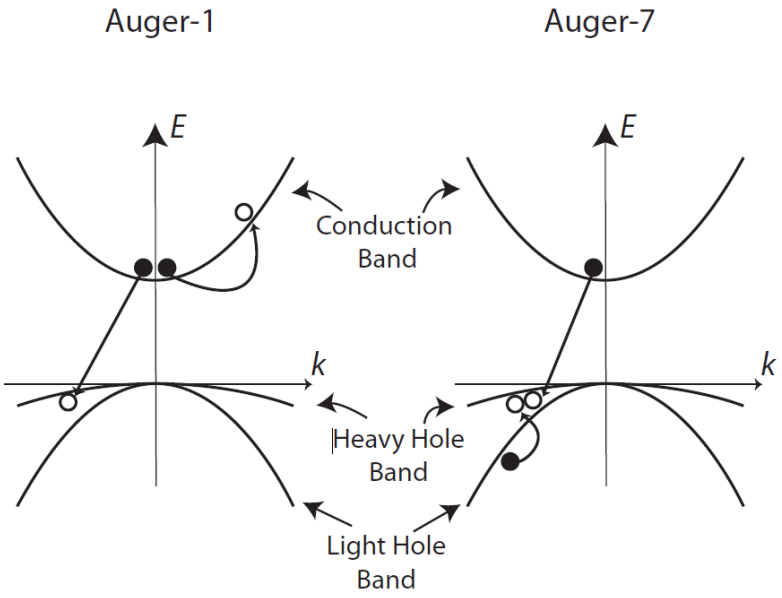

Figure 1.17 Auger-1 and Auger-7 recombination processes [12].

Intrinsic Auger-1 lifetime can be expressed as [12]:

$$\tau_{A1}^{i} = 3.8\times10^{-18}\frac{\varepsilon_{\infty}^{2}(1+r)^{1/2}(1+2r)\exp\left(\frac{(1+2r)E_g}{(1+r)kT}\right)}{\left(\frac{m_e^*}{m_0}\right)\left|F_1F_2\right|^2\left(\frac{kT}{E_g}\right)^{3/2}} \tag{1.25}$$

where $r = \frac{m_e^*}{m_h^*}$, $\left|F_1F_2\right|$ is the wave function overlap integral. For n-type material Auger-1 lifetime is given by [10]:

$$\tau_{A1} = \frac{2\tau_{A1}^{i}n_i^2}{n(n+p)} \tag{1.26}$$

where n_i is the intrinsic carrier concentration, n and p are the total electron and hole concentrations, respectively. For p-type material, Auger-7 lifetime is given by [10]:

$$\tau_{A7} = \frac{2\tau_{A7}^{i} n_i^2}{(n_0 + p_0 + \Delta n)(p_0 + \Delta n)} \tag{1.27}$$

where Δn is the excess electron concentration. τ_{A7}^{i} is given by [10]:

$$\tau_{A7}^{i} = \gamma \tau_{A1}^{i} \tag{1.28}$$

where γ is dependent on temperature and cadmium mole fraction, and it is estimated to lie between $0.5 < \gamma < 6$ for the composition $0.16 < x < 0.3$, and temperature range $50 < T < 300\ K$ [10].

Since n-type and p-type material have different Auger lifetimes, it has to be taken into consideration when choosing the type of material for the absorbing layer.

1.4.6.3 Shockley-Read-Hall Recombination

Shockley Read Hall mechanism occurs through a recombination center in the energy bandgap between the conduction and the valance band, and is not intrinsic. Defects and impurities cause those levels in the energy bandgap. These centers capture one type carrier while attracting the other type as illustrated in Figure 1.18 [10].

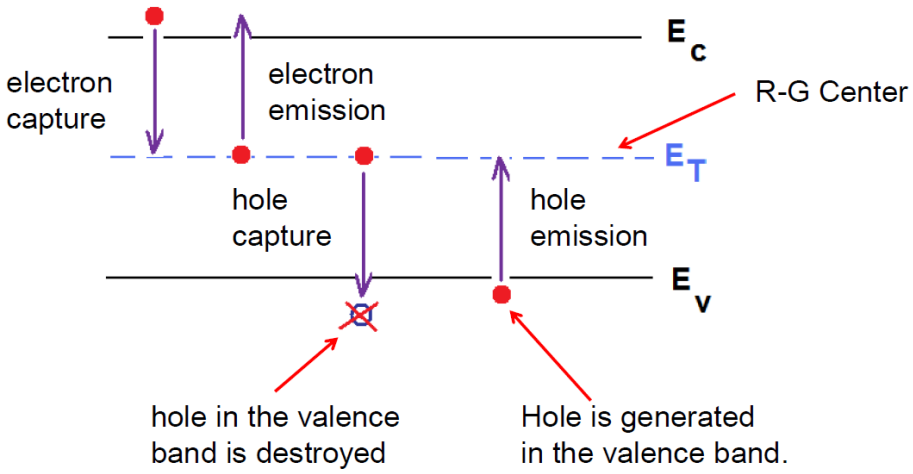

Figure 1.18 Mechanism of Shockley-Read-Hall recombination [6].

The lifetime due to SRH mechanism τ_{SRH} (s) is given by [10]:

$$\tau_{SR} = \frac{\tau_{p0}(n_0 + n_1 + \delta n) + \tau_{n0}(p_0 + p_1 + \delta p)}{(n_0 + p_0 + \delta n)} \tag{1.29}$$

where δn and δp are the excess electron and hole concentrations, and note that since electrons and holes are annihilated in pairs $\delta n = \delta p$, n_1 and p_1 are expressed as [9]:

$$n_1 = N_c \exp\left[\frac{E_t - E_c}{kT}\right] \quad \text{and} \quad p_1 = N_v \exp\left[\frac{E_v - E_t}{kT}\right] \tag{1.30}$$

where N_c and N_v are effective density of states for the conduction and the valance band, and E_c and E_v are the energy values at the conduction and valance band edge. τ_{n0} and τ_{p0} are given by [9]:

$$\tau_{n0} = \frac{1}{\sigma_n v_{th} N_t} \quad \text{and} \quad \tau_{p0} = \frac{1}{\sigma_p v_{th} N_t} \tag{1.31}$$

where σ_n and σ_p are the capture cross sections for electrons and holes respectively. v_{th} is the carrier thermal velocity for electrons and holes, N_t is the density of SR centers.

1.4.7 Optical Absorption

Since HgCdTe has a direct bandgap, it has a very sharp optical absorption characteristic. Figure 1.19 shows the absorption coefficient for different photon energies and different compositions.

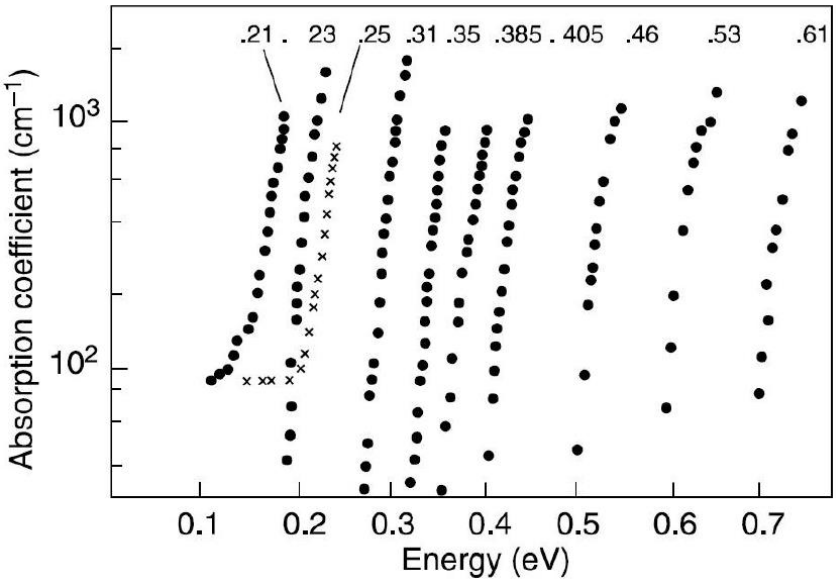

Figure 1.19 Optical absorption coefficient of HgCdTe for different photon energies and different composition [23].

1.4.8 Refractive index

The dispersion of the refractive index can be described by an empirical formula [20]:

$$n(\lambda,T)^2 = A + \frac{B}{1-\left(\frac{C}{\lambda}\right)^2} + D\lambda^2 \tag{1.32}$$

where A, B, C and D are fitting parameters, which vary with composition and temperature, as follows [20]:

$$\begin{aligned} A &= 13.173 - 9.852x + 2.909x^2 + 10^{-3}(300 - T), \\ B &= 0.83 - 0.246x - 0.0961x^2 + 8\times10^{-4}(300 - T), \\ C &= 6.706 - 14.437x + 8.531x^2 + 7\times10^{-4}(300 - T), \\ D &= 1.953\times10^{-4} - 0.00128x + 1.853\times10^{-4}x^2. \end{aligned} \tag{1.33}$$

A plot of refractive index according to Equation (1.32) is shown in Figure 1.20

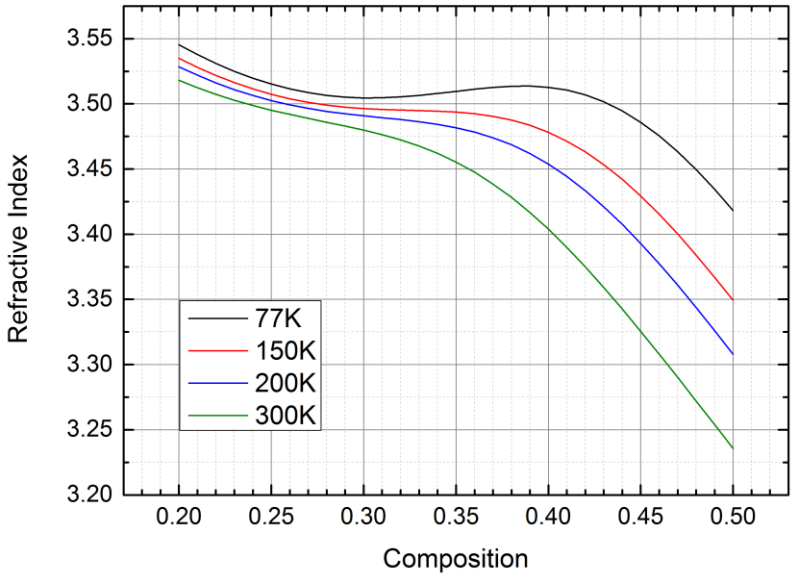

Figure 1.20 Refractive index of HgCdTe with respect to composition for different temperatures according to Equation (1.32).

1.4.9 Dielectric Constant

The dielectric constant describes how an electric field behaves inside the material. The high frequency dielectric constant ε_∞ and static dielectric constant ε_0 are as follows [12]:

$$\begin{aligned} \varepsilon_\infty &= 15.2 - 15.6x + 8.2x^2 \\ \varepsilon_0 &= 20.5 - 15.6x + 5.7x^2 \end{aligned} \tag{1.34}$$

A plot of dielectric constant according to Equation (1.34) is shown in Figure 1.21

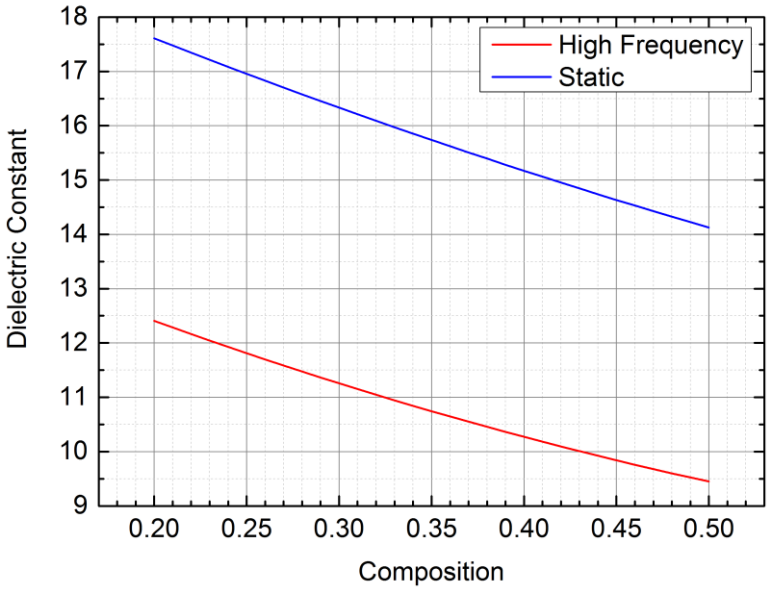

Figure 1.21 Dielectric constants of HgCdTe as a function of composition according to Equation (1.34).

1.4.10 Advantages and Disadvantages of HgCdTe

HgCdTe is the choice of material for advanced infrared detection and imaging devices that are widely used for high performance systems since it was first grown almost 56 years ago [24], [25]. What makes MCT state of the art material for most IR applications can be explained by a number of reasons. These are mainly [25]–[27]:

- The ability to adjust bandgap by changing the mole fraction 'x'. Obtaining cut-off wavelength values between 1-30 μm is possible.
- Almost constant lattice constant with varying the mole fraction 'x'.
- High optical absorption coefficient and high quantum efficiency (as high as 0.99),
- Low carrier generation rate.
- Long carrier lifetime and high electron mobility.

In the IR band, direct bandgap semiconductors such as HgCdTe have much smaller normalized detector dark current than for any of the other types of systems namely, extrinsic semiconductors, quantum well infrared photodetectors and silicon Schottky

barriers. Therefore background limited performance (BLIP) at operating temperature is high for direct bandgap semiconductors [25]. Moreover HgCdTe enables the implementation of hetero-structure devices, multi-color detectors and quantum structured materials. As a result, HgCdTe is the most studied semiconductor for IR applications.

It should be also noted that there are some disadvantages of HgCdTe. HgCdTe material is fragile (weak Hg-Te bonds which lead to bulk and interface instability), and the high cost and limited availability of large area high quality substrate materials (CdZnTe) may present problems.

1.5 HgCdTe Growth Technologies

Different growth methods have been developed for MCT production over the past 56 years. The methods can be classified as;

- Bulk growth,
- Liquid phase epitaxy (LPE) growth,
- Metalorganic chemical vapor deposition (MOCVD),
- Molecular beam epitaxy (MBE).

In the early days of mercury cadmium telluride bulk growth techniques were generally used. As time progressed, other methods took over MCT production.

1.5.1 Bulk Growth of HgCdTe

Bulk growth of HgCdTe is very difficult due to the high vapor pressure of Hg at the crystal melting point, about 950°C [23]. The dominant bulk growth techniques are solid state recrystallization (SSR), the traveling heater method (THM) and Bridgman growth technique [20].

Solid State Recrystallization (SSR): SSR, which is also called as quench anneal (QA) or cast recrystallize anneal (CRA) is crystal growth from the solid phase at near to the melting point temperature. For preparation to growth, pure elements are put into an etched silica ampoule and the mixture is melted and shaken to mix completely. Then the mixture is rapidly quenched to room temperature. This results in a dendritic

structure. This is recovered by the recrystallization step which occurs at below solidus temperature for many days. This step provides grain growth, and inhomogeneities in composition are also recovered [20].

Traveling Heater Method (THM): According to Triboulet, it is needed to be able to grow at lower temperatures, lower pressures and decreased contamination and defect levels. For large-area growth, uniformity of composition and low defects, traveling heater method provides benefits of zone refining and low temperatures [28]. The principle of the method can be seen from Figure 1.22. It consists of a quartz involving source material and heater.

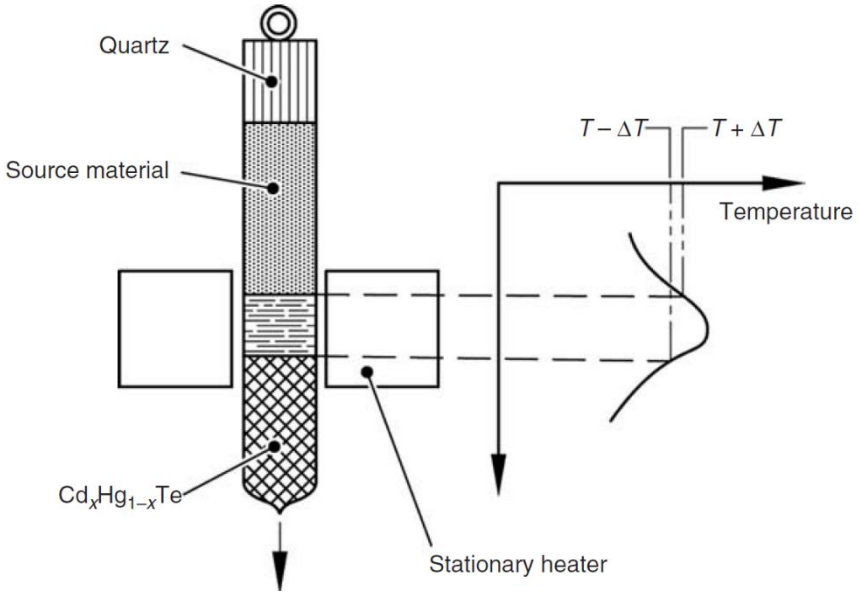

Figure 1.22 The principle of traveling heater method [20].

To produce a narrow molten zone and to avoid super cooling, there should be a high temperature gradient at the growth interface and a sharp temperature peak [20].

Bridgman growth method: In this method, Cd, Hg and Te elements are put into a clean silica ampoule and mixed homogeneously by melting and shaking the mixture. In order to obtain a large good grain ingot, it is frozen slowly from one end in a vertical system.

1.5.2 Epitaxial Growth of HgCdTe

Unlike bulk growth methods, epitaxial growth methods provide lower growth temperatures and uniformity in composition. Another advantages of this method is shorter growth times and larger crystals [10]. However epitaxial growth requires a suitable substrate having the following properties,

- Substrates should be very closely lattice matched to the MCT,
- Substrates should be stable at growth temperature,
- Substrates should not introduce impurities to the epilayer,
- Substrates should be transparent in the IR spectral band of interest unless it is removed later [10].

Early experiments used CdTe as substrate for epitaxial growth of HgCdTe despite its about 2% lattice mismatch to HgCdTe. Later approximately 4% ZnTe is added to CdTe to obtain a lattice matched substrate to be able to grow HgCdTe with epitaxial growth methods.

1.5.2.1 Liquid Phase Epitaxy (LPE) Growth

Liquid phase epitaxy is an epitaxial growth method of HgCdTe. In this method HgCdTe mixture is dissolved in a solvent and the liquid mixture is placed in contact with a single crystal substrate. When the solvent is cooled down, a solid HgCdTe layer is deposited on the substrate [10], [29]. This growth method can be divided into three groups according to the type of apparatus used to place the liquid mixture in contact with the substrate. Moreover it can be divided into two groups according to the type of liquid mixture [10], [30]. Methods classified by apparatus are; dipping, slider and tipping which can be seen from Figure 1.23.

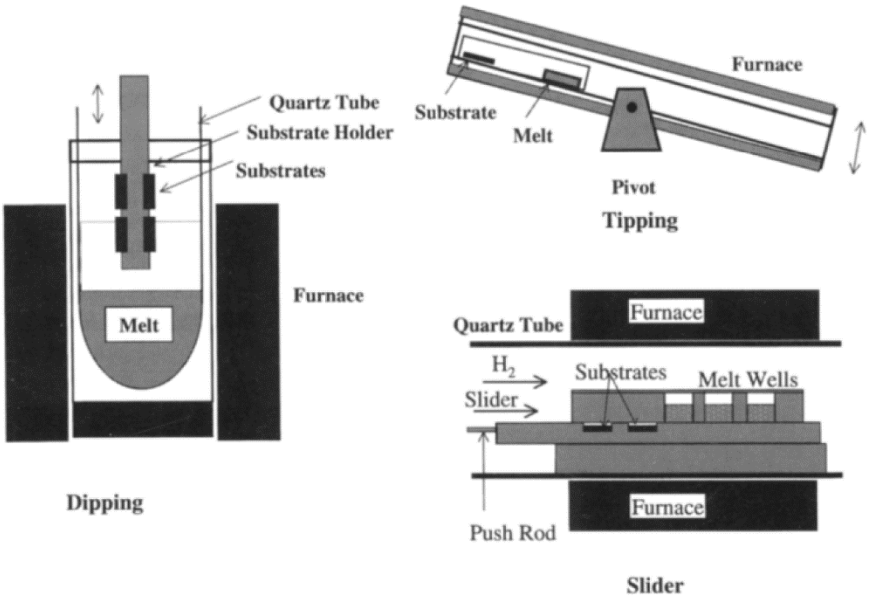

Figure 1.23 Types of Liquid Phase Epitaxy according to the apparatus used [10].

Capper et al. summarizes the advantages and disadvantages of those techniques in Table 1.3 [30].

Table 1.3 Comparison of the three LPE growth techniques [30].

Technique	Advantages	Disadvantages
Sliding Boat	* Thickness control * Large area * Double layers	* Difficult to grow thick layers * Substrate thickness/ planarity control * High cost
Tipping	* Thickness control * Lowest investment for experimental research * Closed system – good P_{Hg} control	* High cost * Scale up
Dipping	* Thick layer growth * High throughput * Low cost * Large/flexible area	* Thin layer thickness control * Double layers

LPE of MCT is a mature technology that it is possible to obtain perfect layers with excellent uniformity and low defects [20]. The typical growth temperature is about ~500 °C.

Growth from Hg-rich solution and growth from Te-rich solution are two different techniques of LPE growth method. Hg-rich solution technique provides perfect surface morphology, more feasible cap layer and ease of the incorporation of dopants [30], [31]. Moreover better compositional and thickness uniformity can be obtained with large melts. Te-rich technique decreases the Hg vapor pressure by almost two orders of magnitude at the growth temperature. Layers which are grown with Hg-rich technique can be easily doped with group VB elements, yet it is difficult with Te-rich technique. On the other hand Group IIIB elements are easily incorporated with both techniques. Both Hg and Te rich solutions can be used with tipping and dipping techniques, whereas the sliding boat has been used with only Te-rich solutions [30].

LPE is characterized as near-equilibrium growth process when compared to other epitaxy techniques. The benefits of LPE include [31]:

- Growth rate can be arranged from 0.1 μm to 10 μm/h. It is faster than that of MOVPE and MBE,
- Lower residual or background impurities in the epitaxial layer,
- Ability to obtain very flat surfaces and excellent surface morphology,
- Unlike vapor-phase growth, wide selection of dopants can be used in liquid phase epitaxy,
- Certain types of defects can be suppressed. LPE grown material has generally lower point defects,
- Growth for a wide range of temperature is possible when phase diagram is established,
- Low cost.

1.5.2.2 Metalorganic chemical vapor deposition (MOCVD)

MOCVD of MCT has been tested using diethyl telluride (DETe), dimethyl cadmium (DMCd) and Hg in 1969. In the formation of HgCdTe, two processes are involved [10]:

1. The CdTe formation from DMCd and DETe at the substrate,
2. The formation of HgTe from DETe and Hg at the substrate.

Control of composition and lateral uniformity are two major difficulties. Those problems have been solved with a breakthrough technique for MCT growth called as Interdiffused Multilayer Process (IMP) [10], [20], [31]. In this technique, very thin layers of CdTe and HgTe are grown sequentially and these layers diffuse together during growth. According to the thickness ratio of CdTe and HgTe, the composition is determined.

In order to obtain sharp interfaces for heterojunction layers, low temperature MOCVD processes are being developed. Since DMCd partial pressure becomes higher and Hg partial pressure becomes lower, the composition of HgCdTe decreases as substrate temperature increases [10]. Moreover the lowest growth temperature is determined by the stability of DETe. As a result, various studies have focused on decreasing of stability of tellurium alkyl [10], [20], [31]. The most direct solution is to use less stable alkyls. The alternative methods include pre-cracking the DETe in a hot zone upstream of the cooler growth area and photo assisted MOCVD. The organometallic species are partially broken down by the energy from ultraviolet photons produced by Hg-arc lamps [10].

The alternative tellurium alkyls include di-isopropyl telluride (DiPTe), di-tertiary-butyl telluride (DtBTe), dimethyl ditelluride (DMDTe) and dihydrotellurophene (DHTeP). It is possible to decrease the growth temperature from ~400°C with use of DETe to ~230°C with use of DtBTe. The tradeoff is that the vapor pressures also decrease with decreasing stability. The commonly preferred Te source is di-isopropyl telluride (DiPTe) which requires a growth temperature of ~350°C [10], [20], [31].

In terms of dopants, most commonly used n- and p-type dopants are iodine (I) and arsenic (As), respectively. Figure 1.24 shows the schematic of a MOCVD cell and IMP [31].

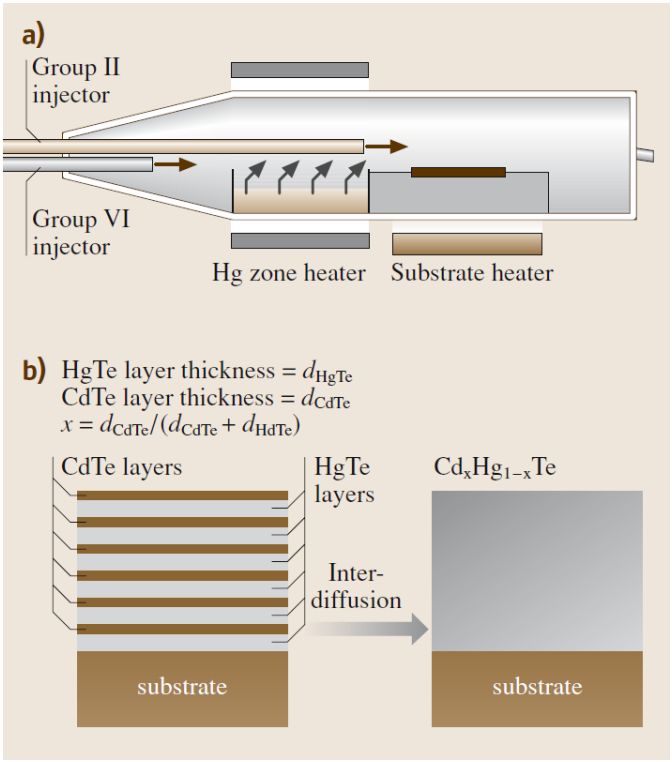

Figure 1.24 (a) Schematic of MOCVD cell (b) schematic of IMP [31].

1.5.2.3 Molecular – Beam Epitaxial Growth (MBE)

MBE is an ultra-high vacuum (UHV) system utilizing vacuum levels less than $5x10^{-11}$ Torr which is achievable with a clean system after baking and filling the cryo panels with liquid nitrogen. This vacuum minimizes the contamination. The atoms and molecules from elemental effusion sources travel in nearly collision free paths until arriving either to substrate or to walls of chamber. The growth chamber is surrounded by cryo panel having a high pumping speed for H_2O, CO, O_2 and other condensable species [20], [31]. Figure 1.25 shows a schematic of MBE system [31].

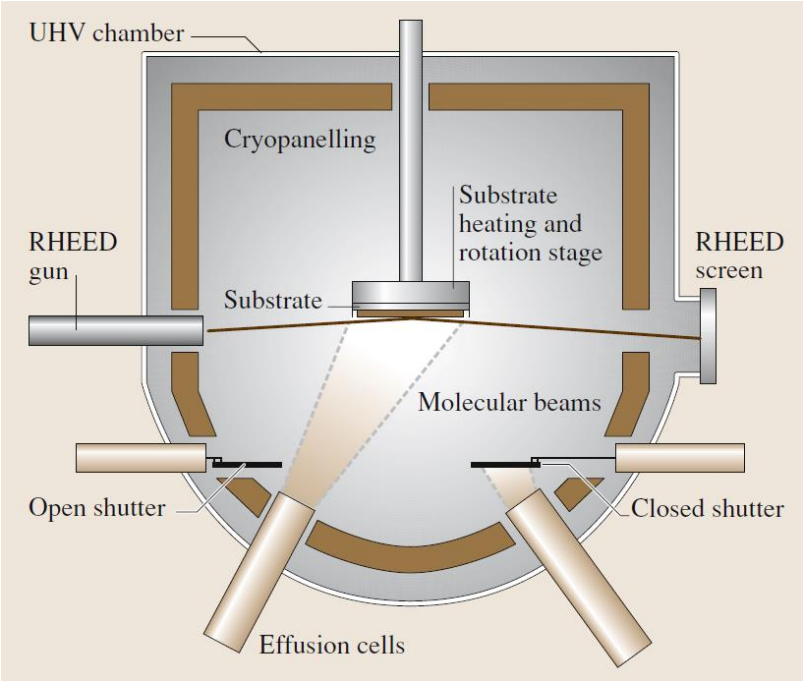

Figure 1.25 Schematic of a MBE growth chamber [31].

The growth chamber includes substrate holder and oven, effusion cells, beam shutters and their movement mechanisms, in-situ characterization tools and beam-flux monitors.

The optimum growth temperature for HgCdTe is between 180°C – 190°C. This temperature gives thermal energy to the atoms arriving at the substrate and due to this energy, atoms can migrate along the surface. Shutters allow the beams to be turned on and off almost instantly with opening and closing times much shorter than the growth time for a single atomic layer. Complex structures can be grown with precise control over thickness and composition.

Indium (In) is mostly used n-type dopant, where As is most widely used for p-type doping.

The detail of MBE growth is given in Chapter 2.

1.5.3 Comparison of the growth technologies

- The MBE growth temperature of HgCdTe is ~185°C which is lower than LPE and MOCVD growth temperatures of ~450°C and 300 - 400°C

respectively. This low temperature greatly reduces inter-diffusion. It allows the formation of precisely controlled homojunctions and heterojunctions.

- Multilayer structures can be grown with MBE, whereas LPE is usually limited to two or three layers, since different melts are required for different composition and doping.
- MBE provides better composition and thickness control.
- Unlike LPE which requires high quality of CdZnTe substrate, MBE allows to grow HgCdTe on alternative substrates.
- MBE allows use of in-situ monitoring tools such as spectroscopic ellipsometry (SE) and reflection high-energy electron diffraction (RHEED).
- MBE offers low growth rates, giving the capability of attaining abrupt interfaces and doping profiles, thus allowing growth of multilayered structures such as quantum wells and superlattices.
- Low kinetic energy of impinging atoms in MBE which leads to a reduced defect density and dopant segregation.

It should be also noted that there are some disadvantages of MBE which create difficulties while growing MCT. These can be listed as:

- Low growth temperature results in poor crystalline quality because of low electron mobility of atoms on surface,
- The growth temperature window is so narrow within ~5-10˚C. Therefore when the growth temperature is out of the optimum window, the growth results with void defects. On the other hand lower temperatures lead to the formation of twin defects. This is because Hg sticking coefficient strongly depends on the growth temperature.
- Unlike n-type doping, p-type doping is a problematic process.

1.6 Short Wavelength Infrared Detectors

The most common SWIR detectors are InGaAs and HgCdTe alloys. InGaAs is widely used because of excellent uniformity, mature fabrication technology, and low cost. HgCdTe has a tunable bandgap by changing the cadmium mole fraction for a wide

range of wavelengths with nearly constant lattice mismatch. On the other hand, InGaAs is lattice matched to InP substrate when In mole fraction is 0.53, and the cut-off wavelength is 1.7 μm at room temperature.

Traditionally SWIR sensing applications use 1.7 μm cut-off wavelength for both civil and military applications. Especially, the detectors with extended wavelength up to 2.5 μm cut-off wavelength have been attracting growing interest nowadays. In order to obtain this cut-off wavelength $In_xGa_{1-x}As$ detectors should have a high mole fraction of In (x) causing the degradation of the performance due to increasing lattice mismatch to InP substrate. Recently, HgCdTe extended SWIR detectors have also become hot topic for researchers. In the following paragraphs, recent studies on InGaAs and HgCdTe SWIR detectors will be given.

In 1992, Linga et al. at Epitaxx Inc. reported extended wavelength InGaAs with 72% In on InP substrate. The growth method was hydride vapor phase epitaxy (VPE). The cut-off wavelength was 2.2 μm. The dark current of 100 μm size pixels was 115 nA under 5 V reverse bias at room temperature [32].

In 1994, Gregory H. Olsen et al. at Sensors Unlimited, Inc. reported lattice matched and extended wavelength InGaAs detectors with 53%, 70% and 85% In on InP substrates. The growth method was vapor phase epitaxy (VPE). A detector array had three different selectable cut-off wavelengths corresponding to 1.65, 2.07 and 2.64 μm, respectively. The detector pixels' dimension was 100 μm by 150 μm. The reported dark current was around 0.4 μA under low reverse bias at room temperature. The quantum efficiency where the responsivity is at maximum level was about 50%. There is no anti-reflection coating on the back surface [33].

In 1996, Kochhar et al. reported extended wavelength InGaAs with 74% In on InP substrate. The growth method was molecular beam epitaxy (MBE). The cut-off wavelength was 2.2 μm. The measured dark current density was about 1.8 mA/cm^2 under 1 V reverse bias at room temperature for 100x100 μm^2 test diodes. The peak responsivity of a 100 μm diameter photodetector was around 0.8 A/W. The reason of this poor responsivity was claimed to be the thickness of the absorber layer which had 1 μm thickness [34].

In 2001, Joachim John et al. reported extended wavelength InGaAs with 80% In on 3" GaAs substrate. The growth method was molecular beam epitaxy (MBE). The cut-off wavelength was 2.55 μm at 250K. The full width at half maximum (FWHM) of the epilayer was reported to be lower than 550 arcsec. The test which was performed with 128 pixels with 50 μm pitch showed that average R_0A was 7.47 Ωcm^2 [35].

In 2004, Martin H. Ettenberg et al. at Sensors Unlimited reported lattice matched InGaAs p-i-n photodiodes with 53% In on InP substrates. The tests indicated that the dark current of 25x25 μm^2 pixels was about 120fA under 500 mV reverse bias at 295K [36].

In 2006, H. Guo-Qiang et al. at State Key Laboratory of Functional Materials of Informatics reported extended wavelength InGaAs with 53%, 60% and 70% In on InP substrates. The growth method was gas source molecular beam epitaxy (GSMBE). The tests on 150 μm diameter photodetectors which had 2.2 μm cut-off wavelength indicated that the dark current was around 10 μA under 5 V reverse bias at 300K. R_0A product was about 10.3 Ωcm^2 and $4.69x10^3$ Ωcm^2 at 290K and 210K, respectively. The peak detectivity was $3.05x10^{10}$ Jones and $7.65x10^{11}$ Jones at 290K and 210K, respectively. The quantum efficiency was supposed to be 70% [37].

In 2007, Tan Hengjing et al. reported lattice matched InGaAs with 53% In on InP substrates. The growth method was MOCVD. The tests indicated that the peak detectivity was $1.9x10^{12}$ Jones at room temperature. The dark current of 56x56 μm^2 detectors was 0.94 nA under 500 mV reverse bias at room temperature [1].

In 2011, Michael MacDougal et al. at Aerius Photonics reported lattice matched InGaAs with 53% In on InP substrates. The tests indicated that the dark current density of 25x25 μm^2 pixels was below 1.5 nA/cm^2 at 293K and below 0.5 nA/cm^2 at 280K [38].

In 2012, Henry Yuan et al. at Teledyne Judson Technologies reported lattice matched InGaAs with 53% In on InP substrate. The growth method was MOCVD. The test indicated that the dark current density of 10x10 μm^2 pixels was 2.2 nA/cm^2, 0.44 nA/cm^2 and 0.19 nA/cm^2 at 300K, 280K and 273K, respectively. For the 12 μm, 15 μm and 20 μm pixels the average dark current densities were 0.44 nA/cm^2, 0.35

nA/cm^2 and 0.33 nA/cm^2 respectively at 280K. The average dark current density was 13.8 nA/cm^2 for 5 μm pixels, 10.3 nA/cm^2 for 6 μm pixels and 9.7 nA/cm^2 for 8 μm pixels. All these data was recorded under 100 mV reverse bias. An anti-reflection coated test photodiode with 0.5mm diameter indicated that quantum efficiency was about 80-85% at room temperature [39].

In 2012, Andrew D.Hood et al. at FLIR Electro-Optical Components reported lattice matched InGaAs with 53% In on InP substrates. The tests indicated that the dark current density of 15x15 μm^2 pixels was 2.95 nA/cm^2 under 100mV reverse bias at 293K [40].

In 2013, F.Rutz et al. reported lattice matched InGaAs p-i-n photodiodes with 53% In on InP substrates. The growth method was MBE. The tests indicated that the dark current density of 15x15 μm^2 pixels was below 10 nA/cm^2 for the applied bias less than 100 mV at 200K [41].

In 2014, Y.Arslan et al. reported extended wavelength InGaAs with 83% In on InP substrate. The growth method was MBE. The cut-off wavelength was 2.65 μm at room temperature. The full width at half maximum (FWHM) of the epilayer was reported to be lower than 1032 arcsec. The tests indicated that the dark current density was 3.7 μA/cm^2 under 25 mV reverse bias at 200K. R_0A was 7x10^3 Ωcm^2 at the same temperature. R_0A was about 10 Ωcm^2 at room temperature. The peak quantum efficiency was higher than 80%. The peak detectivity limited by Johnson noise was 2x10^{10} Jones at room temperature without any anti-reflection coating. Fabricated 640x512 FPA with 25 μm pitch pixels indicated that the nonuniformity in responsivity was 9% at operating temperature of 200K [42].

In 2014, Gaoqi Cao et al. reported extended wavelength mesa type InGaAs with 82% In on InP substrate. The growth method was MOCVD. The cut-off wavelength was 2.58 μm and 2.43 μm at room temperature and 200K, respectively. The dark current density of single pixel with 1 mm diameter was 13.7 μA/cm^2 under 10 mV reverse bias at 200K. The peak responsivity was 1.41 A/W and D* is 3.44x10^{11} Jones at 200K [2].

In 2015, Noam Cohen and Ori Ahpek at Israel Aerospace Industry reported extended wavelength InGaAs/GaAsSb type II superlattice structure. In content was 53% and As content in GaAsSb was 51%. The structure was grown by IQE with MBE method on 3" InP substrate. Three device structures namely 'nin', 'pin' and 'npin' were designed and tested. The first structure consisted of 300 periods of intrinsic InGaAs/GaAsSb with 5 nm thick layers. At the bottom and the top, there was InP layer as a contact layer, and the contact layers were doped with Si. There was an additional buffer layer InAlAs with 52% In concentration between top contact layer and superlattice layers. The wide of the buffer layer was 20 nm. The p zone of the layer and the top p contact were constructed with Zn implantation. The second structure was similar to the first one except for doping. The bottom 50 periods of the SL was n doped with Si, and the top 50 periods of the SL, InAlAs buffer layer and InP contact layers were p doped with Be. That structure was mesa etched. The third structure was designed as bipolar phototransistor. The device consisted of n type InGaAs, intrinsic SL, p type GaAsSb base and n type InP emitter. The photo current generated by radiation was replaced by the base terminal.

The dark current densities of the structures was summarized in Table 1.4. The data was measured with large area devices whose one dimension was 160-1000 μm [43].

Table 1.4 Dark current densities of the designed structures at Israel Aerospace Industry [43].

	nin (A/cm^2) @ -0.4 V	pin (A/cm^2) @ -0.7 V	npin (A/cm^2) @ -0.26 V
Dark @ 233K	$5.5x10^{-4}$	$3.6x10^{-4}$	$5.6x10^{-5}$
Dark @ 253K	$7.5x10^{-4}$	$6x10^{-4}$	$2.6x10^{-4}$
Dark @ 273K	$1.5x10^{-3}$	$1.3x10^{-3}$	$6.9x10^{-4}$
Dark @ 293K	$2.5x10^{-3}$	$3.9x10^{-3}$	$1.3x10^{-3}$
Quantum efficiency @ 293K	60% in short SWIR region and 40% in extended region	60% in short SWIR region and 40% in extended region	In the order of a few percent for whole region

In 2001, Philppe Chorier et al. at Sofradir reported extended wavelength HgCdTe SWIR detector on CdZnTe substrate. The growth method was LPE. The planar type diodes were fabricated from n-on-p films. The cut-off wavelength was 2.5 μm at 175K,

and at this temperature the quantum efficiency was reported as 80%. It is important to note that there was a single layer anti reflection coating. The dark current of 30 μm pitch pixel was about 0.1 pA at 175K. It is unknown how much bias was applied [44].

In 2002, Jin-Sang Kim et al. reported extended wavelength HgCdTe SWIR detector on GaAs substrate. The growth method was MOVPE. The mesa type diodes were fabricated from n-on-p films. The cut-off wavelength was 2.5 μm at 300K. The dark current of 110 μm pitch pixel was 100 pA at 200K and 25 nA at 300K under 400 mV reverse bias. The R_0A product was 300 and $5x10^5$ Ωcm^2 at 300K and 200K respectively [45].

In 2003, Honnavalli Vydyanath et al. at Avyd Devices reported extended wavelength HgCdTe SWIR detector on CdZnTe substrate. The growth method was LPE. The planar type diodes were fabricated from p-on-n films. The cut-off wavelength was 2.1 μm. The tests on 30 μm pitch pixels indicated that R_0A product was 152 and $6.24x10^3$ Ωcm^2 at 295K and 250K respectively [46].

In 2006, A.Hairstone et al. at BAE Systems reported extended wavelength HgCdTe SWIR detector on CdZnTe substrate. The growth method was LPE. The mesa type diodes were fabricated from p-on-n films. The tests results on mini array of 30 μm pixels are summarized in Table 1.5. No anti-reflection was used. Moreover the dark current of the pixels with 100 μm diameter was 50 pA at 220K, 5 pA at 200K and 2.5 pA at 190K under 300 mV reverse bias [47].

Table 1.5 Test results of mini arrays at BAE systems [47].

Temp (K)	Wafer	Cut-off (μm)	R_0A (Ωcm^2)	QE (%)
190	LN781	2.67	$1.27x10^5$	-
	LN782	2.71	$1.68x10^5$	64
	LN783	2.72	$1.44x10^5$	72
200	LN781	2.66	$1.02x10^5$	-
	LN782	2.70	$9.15x10^4$	64
	LN783	2.71	$7.54x10^4$	73
220	LN781	2.65	$1.90x10^4$	-
	LN782	2.68	$9.82x10^4$	64
	LN783	2.69	$1.06x10^4$	74

In 2012, O.Gravrand et al. at Cea-Leti reported extended wavelength HgCdTe SWIR detector on CdZnTe substrate. Two growth methods were used namely MBE and LPE. Some planar type diodes were fabricated from p-on-n films grown by MBE. Other planar type diodes were fabricated from n-on-p films grown by LPE. The dark current density of p-on-n diodes with 2.45 μm cut-off wavelength was about 0.8 mA/cm^2 at 300K and 0.1 $\mu A/cm^2$ at 200K. The dark current density of p-on-n diodes with 2.03 μm cut-off wavelength was about 100 $\mu A/cm^2$ at 300K and 10 nA/cm^2 at 200K. The dark current density of n-on-p diodes with 1.96 μm cut-off wavelength was about 50 $\mu A/cm^2$ at 300K and 2 nA/cm^2 at 200K. Quantum efficiency for both n/p and p/n configurations was larger than 70% at 140K [48].

In 2014, R.Bommena et al. at Epir Technologies reported extended wavelength HgCdTe SWIR detector on Si substrate. The growth method was MBE. The planar type diodes were fabricated from p-on-n films. The cut-off wavelength was 2.65 μm. The tests indicated that the dark current density was about 1 mA/cm^2 at 300K and 10 $\mu A/cm^2$ at 235K. Optical characterization showed that quantum efficiency was about 70% without any anti reflection coating. The average R_0A product was about 15 Ωcm^2 at room temperature [49].

In 2014, H.Figgemeier et al. at AIM reported HgCdTe SWIR detector on in-house fabricated CdZnTe substrate. The growth method was LPE. The cut-off wavelength was 1.75 μm. The planar type diodes were fabricated from n-on-p films. The dark current density of the pixels with 15 μm pitch (under 100 mV reverse bias) was 20 pA/cm^2, 0.2 nA/cm^2 and 2 nA/cm^2 at 200, 220 and 240K, respectively. The maximum $R_{dyn}A$ product was $2x10^6$ Ωcm^2 at 300K and $1x10^7$ Ωcm^2 at 270K corresponding to 1 V reverse bias. The quantum efficiency was about 80% at 210K with three layer anti reflection coating [50].

In 2016, A.Weber et al. at AIM reported extended wavelength HgCdTe SWIR detector on in-house fabricated CdZnTe substrate. The growth method was LPE. The cut-off wavelength was 2.5 μm at room temperature. The planar type diodes were fabricated from n-on-p films. The dark current density of the pixels with 24 μm pitch (under 500 mV reverse bias) was 15 $\mu A/cm^2$, 50 nA/cm^2 and 0.6 nA/cm^2 at 250, 200 and 170K, respectively. The maximum $R_{dyn}A$ product was $2x10^5$ Ωcm^2 at 300K, $3x10^6$ Ωcm^2 at

270K and $1x10^8$ Ωcm^2 at 200K. The average quantum efficiency between 1 μm and 2.4 μm was about 74% at 150K [51], [52].

In 2017, Xiaoning Hu et al. reported extended wavelength HgCdTe SWIR detector on Si substrate. The growth method was MBE. The FWHM was about 61 arcsec for CdTe on Si and 65 arcsec for HgCdTe on CdTe/Si. The cut-off wavelength was 2.67 μm. The planar type diodes were fabricated from n-on-p films. The dark current density of the pixels with 30 μm pitch was on the order of 10^{-10} A/cm^2 at 110K. The quantum efficiency was around 70% at the same temperature [53].

The next chapter will present the MBE growth and fabrication of the extended SWIR HgCdTe detectors investigated in this thesis work. The results of the investigation will be discussed in Section 3.7.

CHAPTER 2

MOLECULAR BEAM EPITAXIAL (MBE) GROWTH OF EXTENDED SHORT WAVELENGTH HgCdTe AND TEST ARRAY FABRICATION

The HgCdTe layers studied in this thesis was grown by MBE at Aselsan A.Ş. The substrates, CdZnTe, are home-polished to make them epi-ready for MBE growth by another group at Aselsan A.Ş.

2.1 MBE growth chamber

The MBE system is mainly composed of a loading chamber, a storage chamber, a degas chamber, a growth chamber and a cluster chamber which allows to the transfer of the substrate between each chambers under UHV environment. A reflection high energy electron diffraction (RHEED) system, a spectroscopic ellipsometry system, a band edge measurement system and a residual gas analyzer (RGA) system are installed on the growth chamber.

RHEED is used to gather information about the crystal quality of very few top layers during the growth. RHEED consists of an electron gun and phosphor covered screen. The electron beam with 8 -20 keV energy is incident on the growing surface at a small angle, and the diffracted beam strikes the screen providing information about the crystal quality of the growing [54].

Band edge measurement system measures the bandgap of the substrate by optical methods. The substrate is illuminated by a broadband light source and the reflected light from the substrate is measured from which the bandgap of the substrate is determined. The system is not useful when HgCdTe layer thickness is greater than 300 nm, since HgCdTe absorbs the light at the wavelength of interest after a specific thickness.

2.2 Growth of Extended SWIR HgCdTe

2.2.1 Substrate Preparation

CdZnTe is the choice of substrate in order to obtain high quality epitaxially grown HgCdTe layers since its thermal and mechanical properties perfectly match with HgCdTe. As received CdZnTe substrates have a thin oxide layer on top and this oxide layer cannot be removed thermally without degrading the crystal quality. As a result the oxide layer is removed by chemical etching. The main purpose of the MBE pre-etch is to provide a clean stoichiometric, atomically smooth and well-ordered surface to reduce the number of the growth defects. Benson et al. [55] and Garland et al. [25] clearly demonstrated that MBE pre-etch is a must for CdZnTe substrates. The MBE preparation etch is composed of:

1. Organic cleaning of the substrate in hot acetone, methanol and isopropanol alcohol.
2. Removing of top 5-7 μm layer by etching in Bromine/Methanol solution.
3. Rinsing the substrate with methanol and DI water.

Once the CdZnTe substrate is cleaned, etched, rinsed and dried, it is sticked to the substrate holder. The substrate is held in place on the substrate holder by surface tension. After the substrate is sticked, it is loaded into the loading chamber as soon as possible in order to avoid surface reaction with oxygen.

2.2.2 Flux Calibration

In order to obtain reproducible layers in terms of thickness and composition, all fluxes have to be same for each growth run. The fluxes of the high purity materials depend on the cell temperature and valve openings or both. Therefore fluxes for each material

is measured by placing the flux gauge as close as possible to the substrate location. The required fluxes are achieved by adjusting the cell temperatures and valve openings.

2.2.3 Growth of HgCdTe layer

Whenever the system is calibrated and ready for the growth, the substrate is transferred to the growth chamber. First of all, the substrate is thermally degassed in order to remove the very thin native oxide and excess Te left after the Bromine/Methanol etch. Improper preparation and degassing of the substrate will result in poor crystalline quality of HgCdTe.

The temperature of the manipulator is increased to evaporate excess Te. RHEED is used to monitor the Te desorption. The RHEED pattern for as loaded substrate is shown in Figure 2.1.a. After a specific temperature, excess Te molecules on the surface becomes mobile and streaky lines start to be observed. At the time Te is evaporated, short straight lines are observed as in Figure 2.1.b. Note that there is no pattern at the background of RHEED. The evaporation temperature of Te is important, since it is used for temperature calibration for growth. It is noted that the Te evaporation temperature is ~195°C [20], [25]. That temperature is noted for both thermocouple and BandiT. Hereafter, the temperatures of BandiT is given in the form of T_0 which indicates Te evaporation temperature. After observing the evaporation, the manipulator temperature is continued to increase up to T_0+100°C. At this temperature the substrate is degassed for 10 min. The high temperature thermally cleans the substrate of any native oxide and excess Te, which is always present after bromine-methanol etch. After degas RHEED pattern improves as in Figure 2.1.c. Then the substrate temperature is decreased to T_0-10, since the optimum growth temperature for HgCdTe is reported to be ~185°C [20], [25].

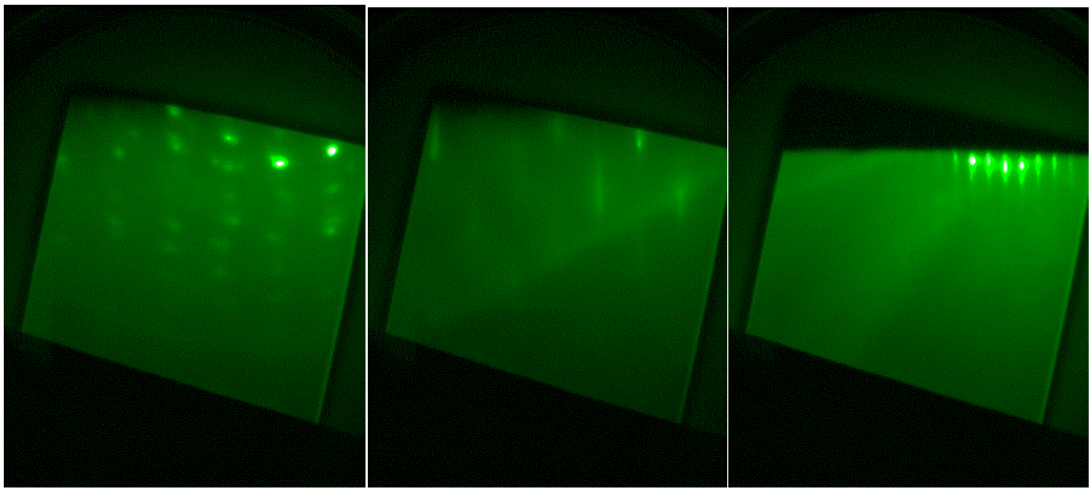

a b c

Figure 2.1 RHEED patterns of CdZnTe substrate when it is loaded (a), when Te is evaporated (b), when the substrate is degassed (c).

The substrate temperature shall be kept constant in a very narrow temperature window. If growth is performed at a temperature higher than the optimum window then void defect density increases, if growth is performed at a temperature lower than the optimum window then twin defect density increases. This is due to the sticking coefficient of Hg which strongly depends on the growth temperature. The effect of growth temperature on crystalline quality of HgCdTe is shown in Figure 2.2. Hence, whenever the manipulator temperature is stabilized, growth can be started by opening the required source shutters.

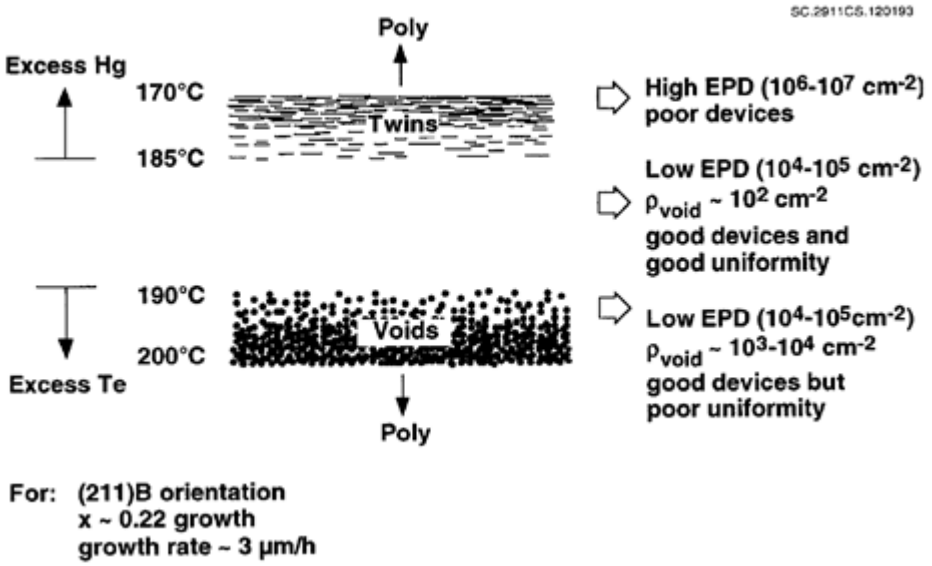

Figure 2.2 MBE growth window of HgCdTe [56].

The growth temperature can also be interpreted via observing the RHEED pattern. If growth starts at lower temperatures than optimum or Hg flux is so high, then one can see cross dots instead of long straight lines at the RHEED pattern as shown in Figure 2.3.a. If growth starts at higher temperatures than optimum or Te flux is so high, then one can see short segments following by circles at the RHEED pattern as shown in Figure 2.3.b. For optimum case the long straight lines pattern of CdZnTe do not change when HgCdTe growth is started. It is shown in Figure 2.3.c.

There is an optimum Hg to Te flux ratio for every substrate temperature. If higher Hg is used twin defects are observed after the growth, if lower Hg is used then Te void defects are observed after the growth. The detailed defect characterization is given in the following sections.

The growth rate is another important parameter. If the growth rate is too high or too low then defect density may increase. The growth is performed in a layer by layer fashion. Therefore, if growth rate is high, then the second monolayer starts to grow before the first monolayer completes its growing. Hence, at higher growth rates, atoms cannot have enough time to migrate on the surface. Same situation is observed for lower growth rates. In this case, atoms stick to grown atoms and coming excess atoms

continue to stick creating islands which is not desirable. The desired growth mode is layer-by-layer, two dimensional or Frank-van der Merwe growth mode [25].

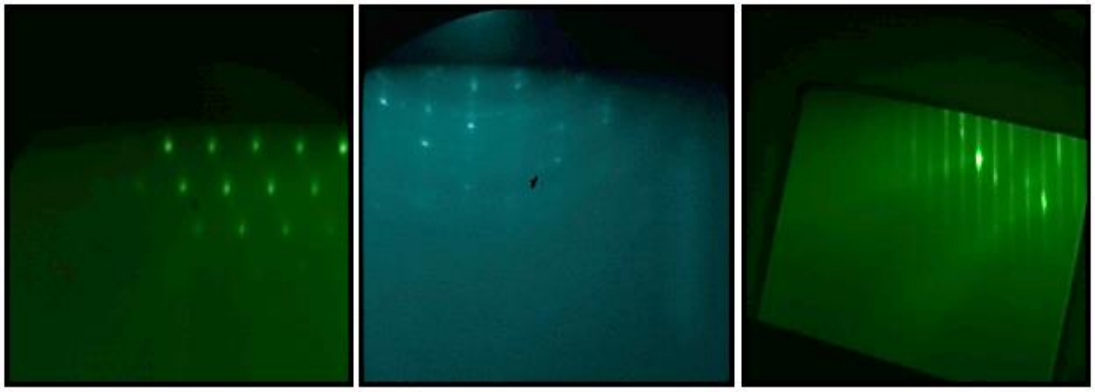

(a) (b) (c)

Figure 2.3 RHEED patterns of HgCdTe when the growth starts at low temperatures or Hg is high (a), when the growth starts at high temperature or Hg is low (b), when the growth is at optimum conditions (c).

Figure 2.4 shows a study conducted by E.C.Piquette et al. [57]. It is claimed that higher growth rate causes insufficient Hg at the surface and small migration time which lead to high void density and twin defects, respectively. Lower growth rate makes surface Hg-rich resulting in increase of micro defects as well as larger voids.

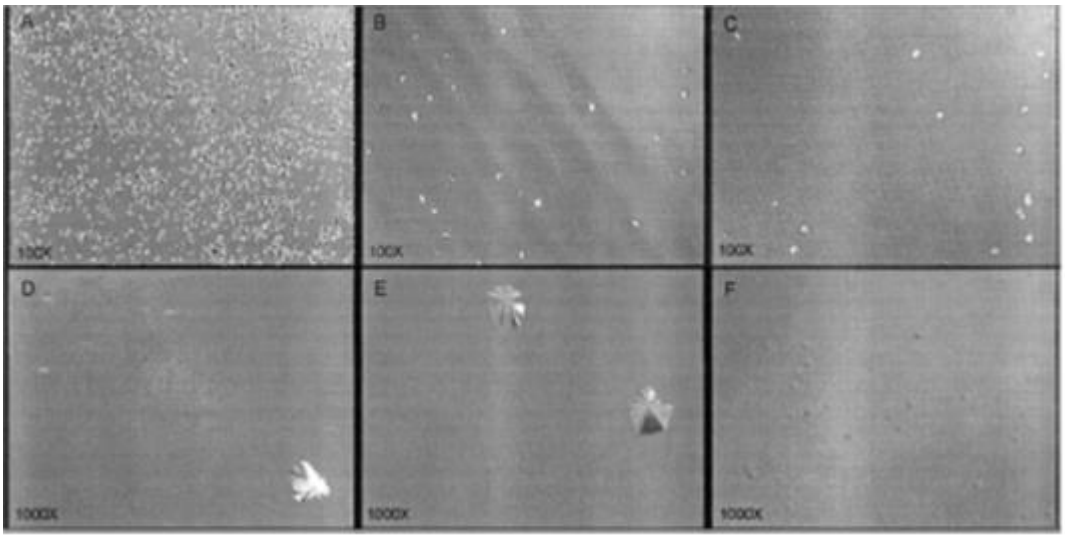

Figure 2.4 Nomarski microscope images of three layers (x=0.2) grown with same conditions except for different growth rates. A and D show a layer grown at 3.6 μm/h, B and E show a layer grown at 1.9 μm/h, C and F show a layer grown at 1.2 μm/h [57].

When the growth is completed, the temperature is decreased to a suitable level for transferring. The substrate is cooled under Hg flux. The Hg flux prevents Hg out diffusion from the layer and keep the surface stoichiometry. Since Hg is volatile, Hg bonding can be easily broken at high temperatures. As a result, Hg vacancies and voids may arise which are detrimental for diode performance.

The standard temperature cycle for growth is illustrated in Figure 2.5.

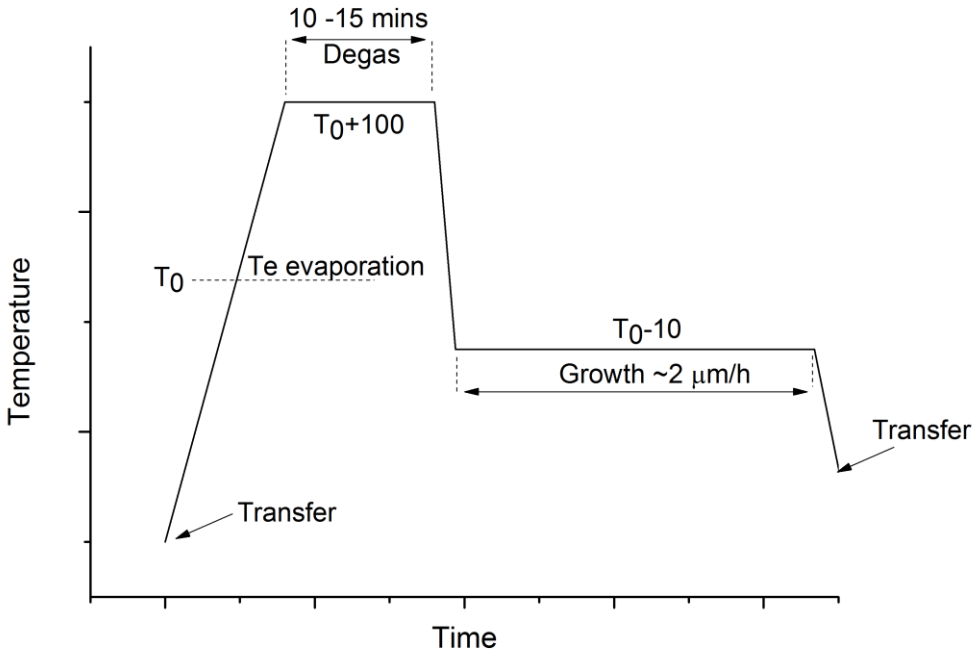

Figure 2.5 Typical substrate temperature cycle used in the growth of HgCdTe from the initial thermal cleaning to the growth.

2.2.4 Doping of HgCdTe

1B and 5A elements can be p-type dopants, since these elements have one less electron than 2B and 6A elements, respectively. Similarly 3A and 7A elements can be n-type dopants, since these elements have one more electron than 2B and 6A elements, respectively. Furthermore, some research groups use Hg vacancies as p-type doping. However, it is challenging to repeatably obtain same doping levels with this method.

For n-type doping In and I are mostly used elements. For MBE system In is preferred, since under Te rich growth conditions, growing layers have a high density of cation vacancies which provides layers with incorporating with 3A elements easily for doping [26]. In this study, In was used as n-type dopant, and the targeted n-type doping level for the layers is ~$5x10^{15}$ cm^{-3}.

For p-type doping, Group I elements incorporate easily into HgCdTe as p-type dopants, yet they are unsuitable because of their high diffusivities [58]. Since group V elements have large atomic size, those group elements have lower diffusivity which

make group V elements suitable for p-type doping. On the other hand, these elements are amphoteric in HgCdTe that they can occupy both cation (Cd or Hg) and anion (Te) sites [59]. Arsenic is the most commonly studied and used as p-type doping element. However, the growth conditions of MBE causes As to be incorporated in the cation site of Hg. This leads to As to behave like n-type dopant. In order to provide As with enough energy to transfer from cation to anion site, an activation annealing should be performed. This process is necessary to convert As to a p-type dopant [56]. Annealing includes two steps, namely activation annealing and vacancy annihilation annealing.

The goal of activation annealing is to transfer As atoms from the cation site to anion site, so that they can behave as acceptors. The required thermal energy to make site transfer possible is provided with high temperature annealing around 430-450°C. The annealing procedure is usually conducted under Hg overpressure to maintain stoichiometry of the sample and avoid defects that form due to Hg out diffusion [59].

The goal of vacancy annihilation or saturation annealing also called as low temperature annealing is to fill the Hg vacancies in the HgCdTe layer. In order to be sure about filling of Hg vacancies, the layer is annealed at 220-250°C for extended amounts of time (at least 16-120 hours). This annealing step is usually performed under Hg overpressure [59].

In the first stage of activation, Te atom moves to Hg vacancy to leave behind a Te vacancy and creating a Te anti-site. The arsenic then moves to the Te vacancy and becomes an acceptor. Finally, the Te anti-site bound to an Hg vacancy will migrate to the surface and leaves the crystal [56]. Schematic of As activation is given in Figure 2.6.

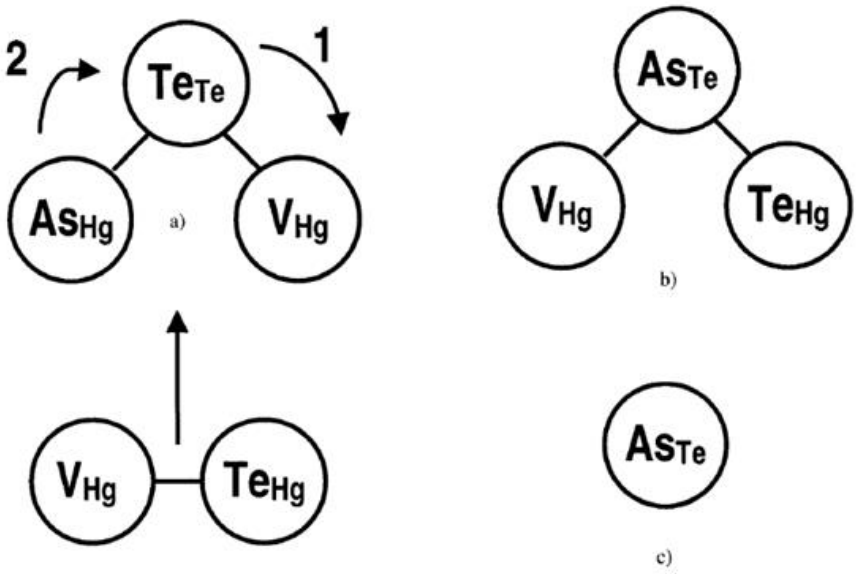

Figure 2.6 Schematic of As activation [56].

In this study, the samples were annealed at 450°C for 1 hour and followed by low temperature annealing at 200°C for 48 hours. The achieved p-type doping level with As is ~1x10^{19} cm^{-3}.

2.3 Characterization of HgCdTe Layers

As part of this thesis study, extended SWIR HgCdTe layers was grown on home-polished CdZnTe substrates with ~2.2 μm cut-off wavelength. The grown layer structure is shown in Figure 2.7.

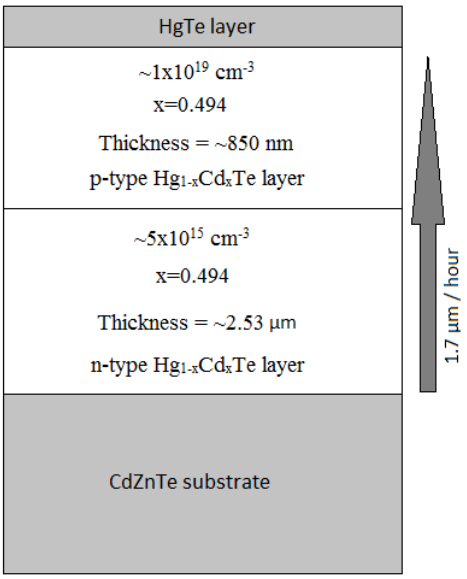

Figure 2.7 The structure of grown extended SWIR HgCdTe layer

The grown sample on molybdenum blank can be seen from Figure 2.8. Before characterization of the sample, the sample is cleaned from In which is used to stick CdZnTe substrate to molybdenum blank. This is achieved with HCl acid dipping.

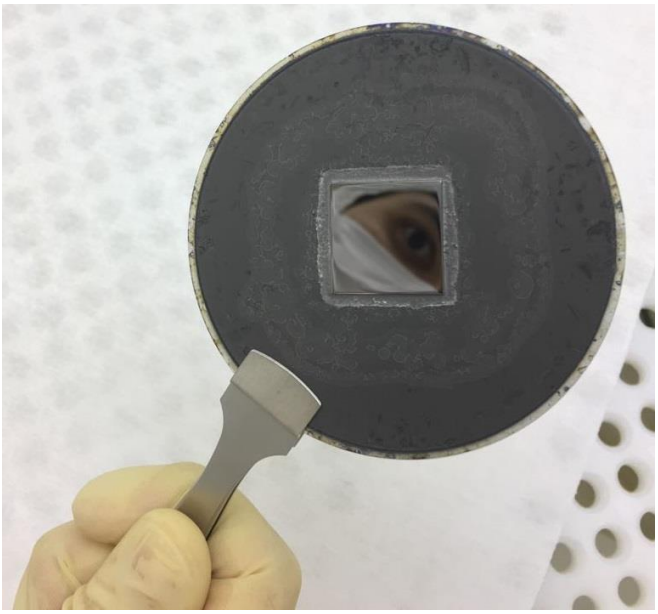

Figure 2.8 SWIR HgCdTe grown sample which is sticked on molybdenum blank with Indium.

2.3.1 FTIR Measurement for composition determination

Fourier transform infrared spectroscopy (FTIR) is a tool providing infrared spectrum of transmission or absorption of a sample. Any absorption spectroscopy aims to detect how much a sample absorbs the light at each wavelength. FTIR uses a beam of light with different frequencies and measures how much of that light is absorbed by the sample.

The FTIR spectrum of the grown sample at room temperature is given in Figure 2.9. The cut-off wavelength of the sample is 2.17 μm. The corresponding cadmium composition is 0.494. The method to determine the cut-off wavelength is to find the maximum transmission, and then obtain the wavelength as cut-off at half of maximum transmission. The reason why transmission is low is due to HgTe layer. Since this layer a semi-metal, transmission is reduced through this layer.

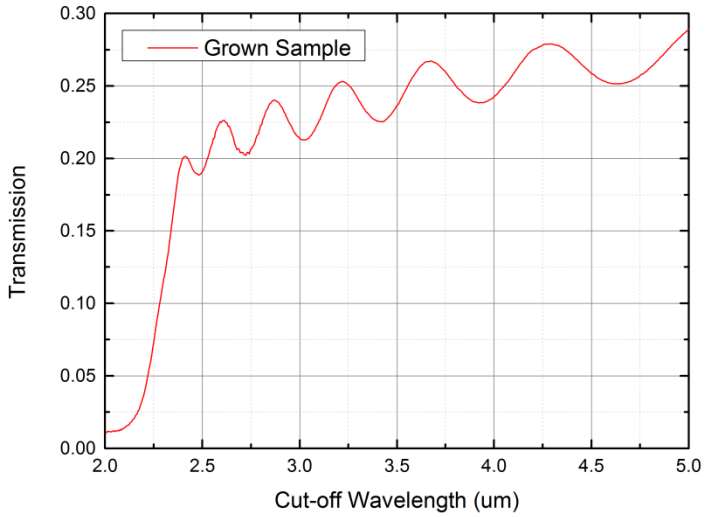

Figure 2.9 The FTIR spectrum of the grown HgCdTe layer.

2.3.2 X-Ray Diffraction for crystal quality determination

An X-ray is scattered from an atom and the striking X-ray generates a secondary wave arising from the atom. This is called as elastic scattering and the scatterer is atom. These secondary waves add constructively in a few specific directions although they

remove one another in most directions destructively. That constructive interference is determined by Bragg's law as:

$$2d \sin\theta = n\lambda \tag{2.1}$$

where d is the spacing between diffracting planes, θ is the incident angle, n is an integer, and λ is the wavelength of the beam. In order to obtain meaningful diffraction, the wavelength of the incident wave should be comparable with the spacing between the scatterers. Since X-rays have wavelength similar in size with the spacing, they are used to obtain the diffraction pattern.

The X-ray diffraction pattern of the CdZnTe substrate is given in Figure 2.10. The full width at half maximum (FWHM) is 69 arcsec. That of the grown sample is given in Figure 2.11. The FWHM is 78 arcsec. FWHM is the width of the spectrum where the intensity is half of the maximum intensity. Lower FHWM values indicate better crystal quality. In other words impulsive characteristic of the spectrum means perfect crystal quality. Since XRD measurements were performed with analyzer, the substrate peak is not seen in X-Ray diffraction pattern of the grown sample.

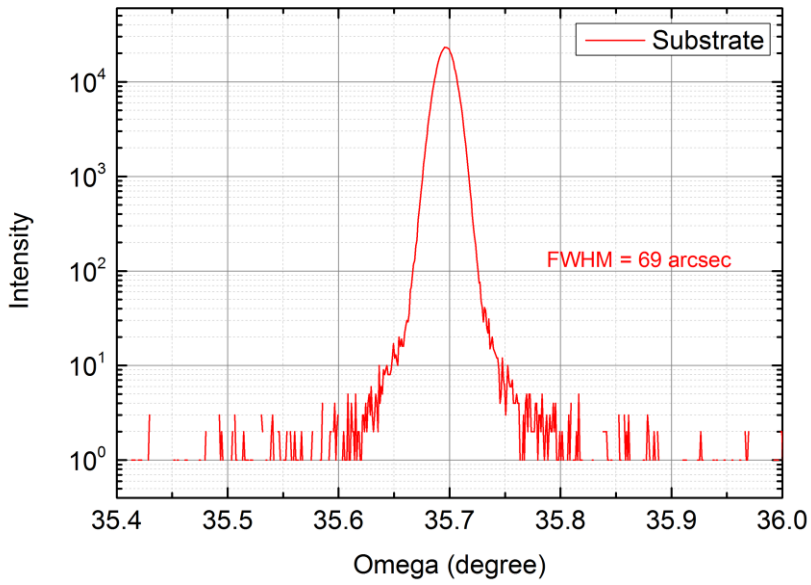

Figure 2.10 X-ray diffraction pattern of CdZnTe substrate.

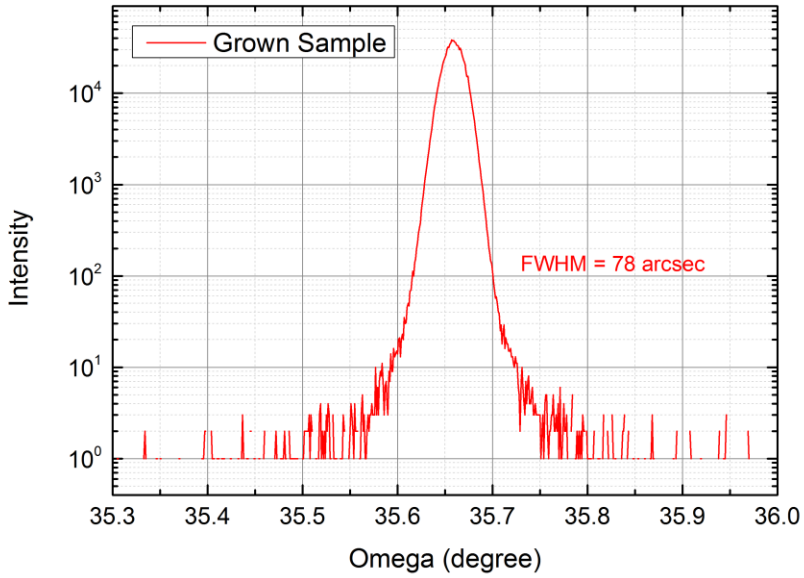

Figure 2.11 X-ray diffraction pattern of the grown HgCdTe layer.

2.3.3 Surface characterization of the HgCdTe layer

Nomarski microscopy and scanning electron microscopy (SEM) are used to observe surface defects of the grown sample. One of the significant drawbacks of HgCdTe alloys is high densities of native defects. Defects originating from the growth decrease the pixel performance. There are kinds of defects on HgCdTe surfaces. Voids, hillocks and the mixture of both of them are observed defects. Substrate, growth or both of them are source of those defects. The most common observed defect in MBE grown HgCdTe layer is surface voids, also known as 'V-shaped defects' [57], [60]–[67]. It is believed that those defects result from Hg deficiency due to Te-rich growth conditions. A typical density of V-shaped defects is around 10^3 cm^{-2} [64]. However Zandian et al. reported as low as 100 – 200 cm^{-2} defect density [57], and also another group demonstrated 300 cm^{-2} defect density by optimizing the growth conditions and substrate preparation [60]. V-shaped defect located within the active area of a photo diode reduces the diode performance. Therefore V-shaped defects should be minimized as far as possible. Figure 2.12 shows a V- shaped defect.

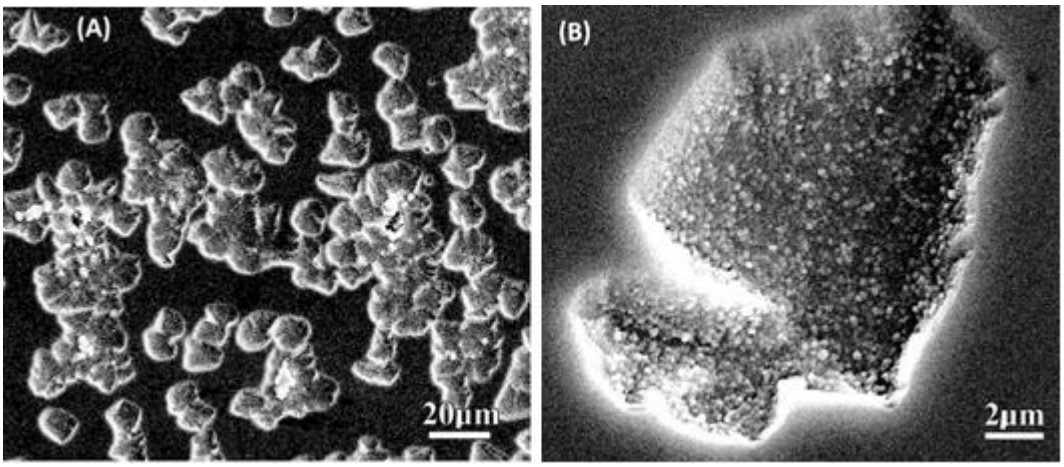

Figure 2.12 (a) SEM micrograph of surface crater defects for HgCdTe / CdZnTe grown by MBE. (b) Higher magnification of the crater defect [62].

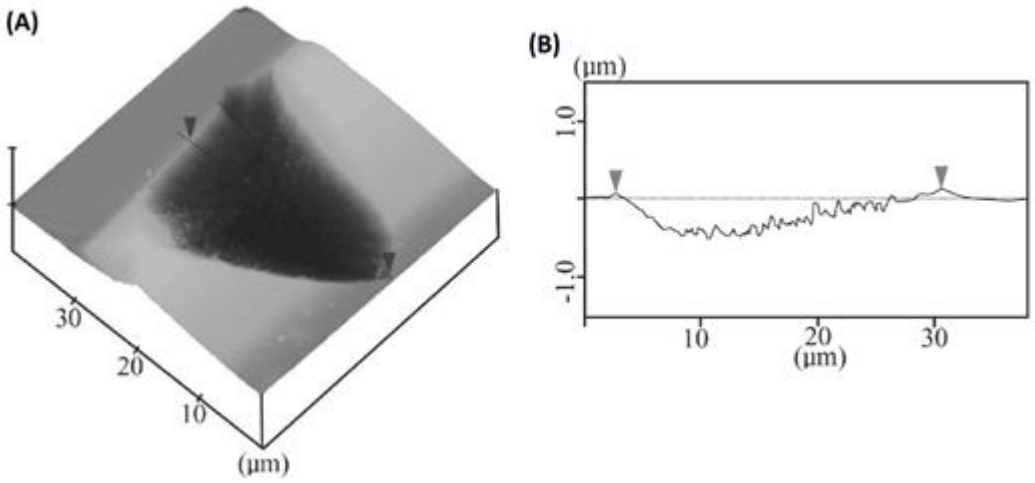

Figure 2.13 (a) AFM micrograph of the surface crater defect. (b) line scan across the region indicated in picture (a) and overall depth of ~600 nm [62].

As seen from Figure 2.13, the size of V-shaped can be as large as 10 – 30 µm or more for films of 8 – 10 µm thickness.

L.He et al. [60] and R. Haakenaasen et al. [63] classified the defect types as growth and substrate originating defects. When the substrate temperature is lower than optimum growth temperature or Hg/Te flux ratio is higher than optimal, then microvoids are formed and twinning occurs. When the substrate temperature is higher than optimum growth temperature or Hg/Te flux ratio is lower than optimal, then high

temperature voids (also called as V-shaped defects, surface crater defects and voids) start to form.

Haakenasen et al. studied on growth of HgTe and HgCdTe in order to optimize the growth temperature [63], [65]–[67]. Microvoids in HgTe has a clear characteristic in shape and density with respect to growth temperature. Figure 2.14 shows microvoids in layers grown at different growth temperatures. At low temperatures microvoids create clusters (Figure 2.14.a and Figure 2.14.b). The number of microvoids in these clusters decreases with increasing of growth temperature. At optimum growth temperature, they are single microvoids. The shape of the microvoid at optimum growth temperature can be seen from Figure 2.14.c. It is like a diamond. There is a hole at the center of the diamond. The shape of the microvoid changes from diamond to triangular shape as the temperature increases.

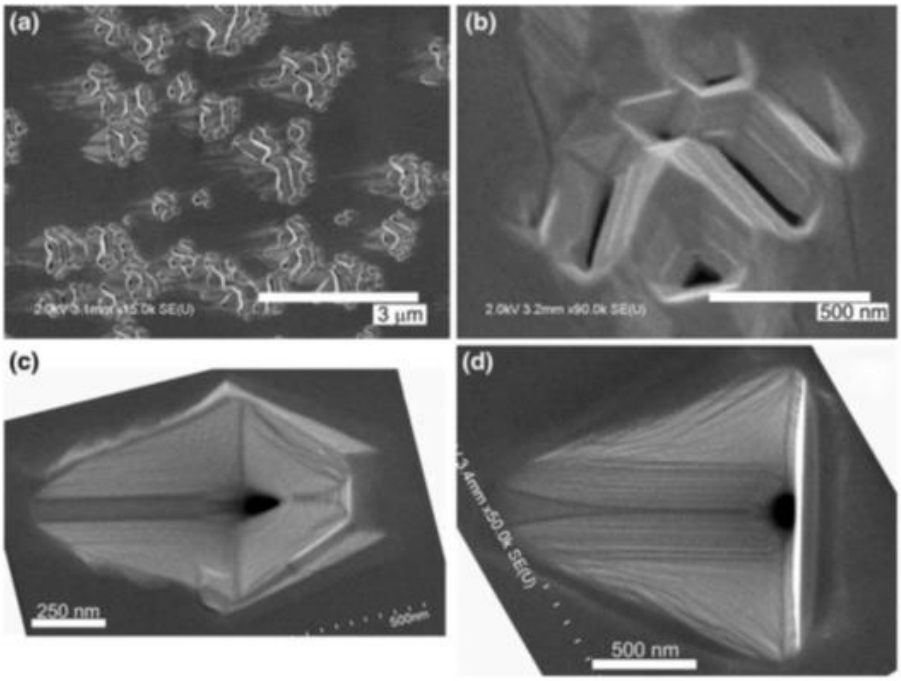

Figure 2.14 Microvoids in HgTe layers grown at different growth temperatures. a) T_{opt} – 10°C, b) T_{opt} – 6°C, c) T_{opt}, d) T_{opt} + 6°C [66].

In HgCdTe, there is no such clear temperature dependence of the microvoids. The microvoids can have different shapes and sizes in the same layer which indicates that the microvoids can start to form in the films as well as at the substrate interface [63], [66]. For low growth temperatures, unlike HgTe layers, the microvoids are mostly

unclustered in HgCdTe layers. Moreover the microvoids are usually more rounded than the shape of it in HgTe. Figure 2.15 shows microvoids in HgCdTe grown at different temperatures.

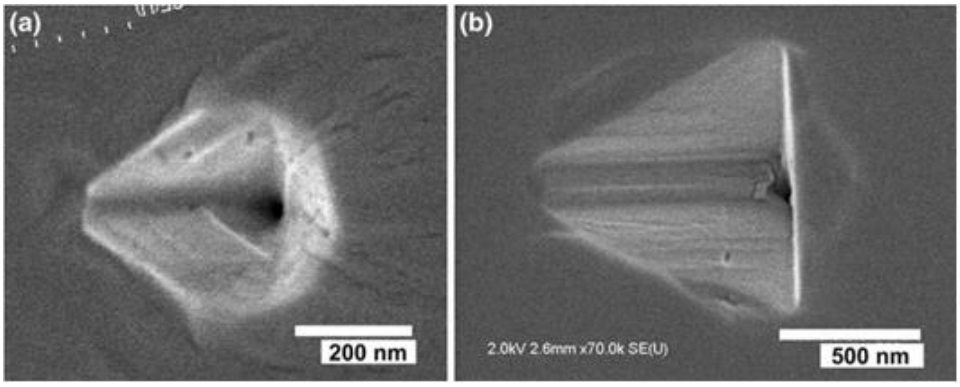

Figure 2.15 Microvoids in HgCdTe layers grown at different temperatures. a) T_{opt} – 12.3°C b) T_{opt} + 2.9°C [66].

For high growth temperatures, due to low sticking coefficient of Hg, it is evaporated. Hence, there will be Hg deficiency at high growth temperatures. In case of Hg deficiency, Te precipitates will nucleate and grow, and as a result of this, a poor crystalline HgCdTe will form. The high temperature voids can become much larger than the microvoids, and their size increases with growth temperature. Figure 2.16 shows high temperature voids grown at different growth temperatures.

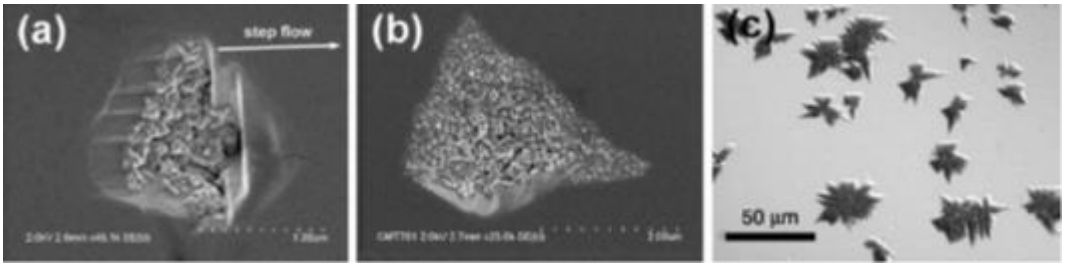

Figure 2.16 High temperature voids in HgCdTe layers. a) SEM image of small void at T_{opt} + 2.9°C b) SEM image of larger void at T_{opt} + 5°C c) Optical image of very large void at T_{opt} + 8.3°C [65].

There are also substrate related defects in HgCdTe layers. Needle defect is one of the observed defects. E.Selvig et al. [65] showed that the needle length is about the same

as the film thickness. This indicates that the needles nucleate at the substrate interface and grow with the film.

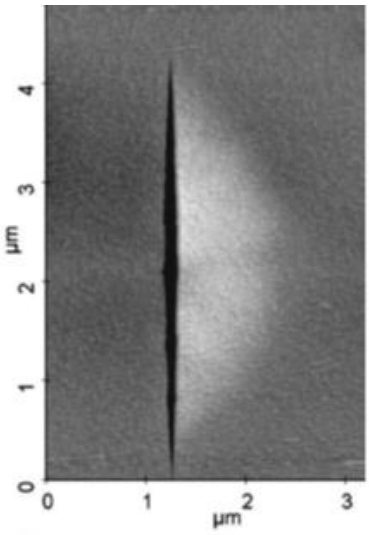

Figure 2.17 AFM image of a Needle defect [66].

L.He et al. [60] also studied defects in HgCdTe layers and they showed that failing to remove organic contamination on substrate surface also causes substrate related defects. This mostly happens when the substrate is rinsed in bad DI water. Figure 2.18 shows the substrate related defect caused by organic contamination.

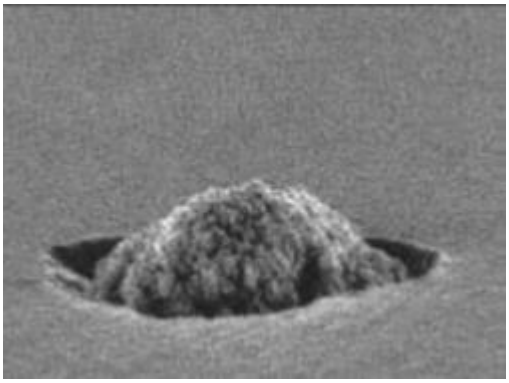

Figure 2.18 SEM image of the substrate related defect caused by organic contamination [60].

SEM and nomarski images of the sample grown in this work are shown in the following figures.

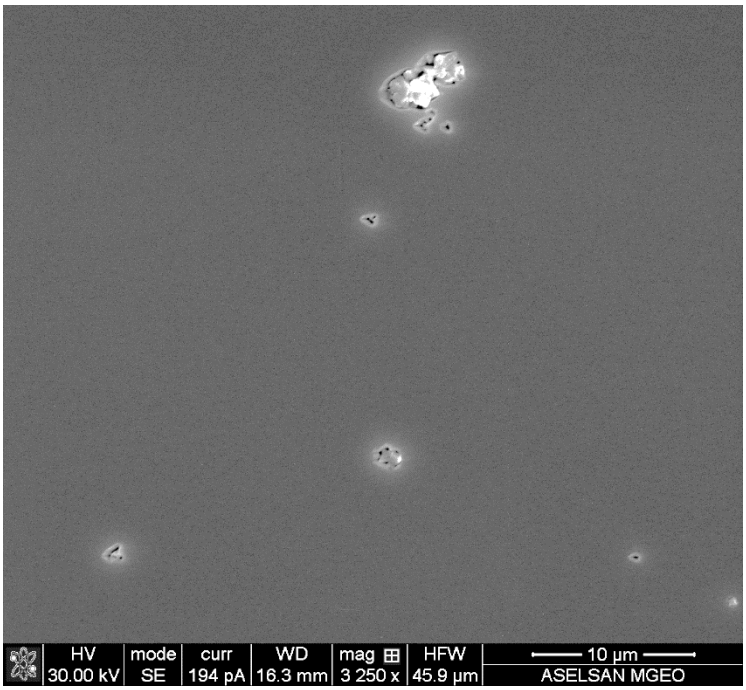

Figure 2.19 SEM image of the grown HgCdTe layer surface.

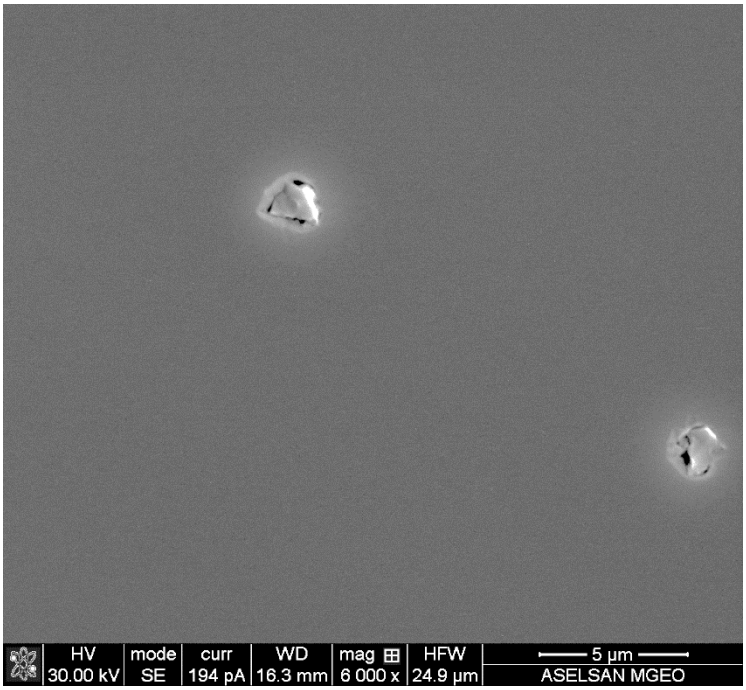

Figure 2.20 SEM image of the grown HgCdTe layer surface.

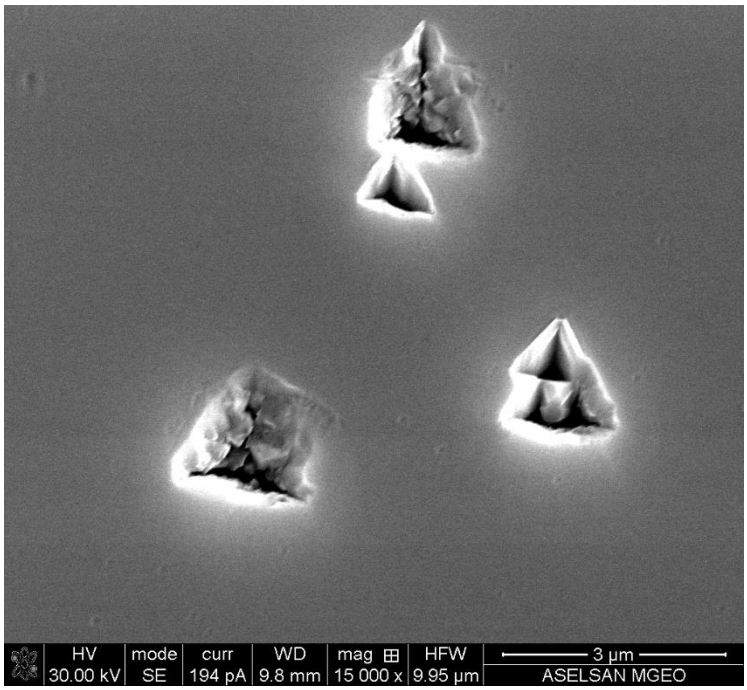

Figure 2.21 SEM image of the grown HgCdTe layer surface.

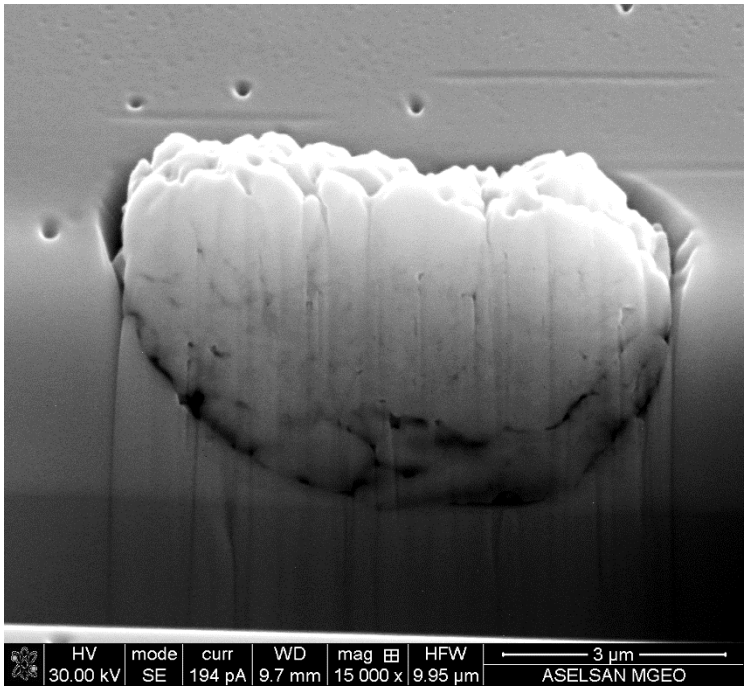

Figure 2.22 Cross sectional SEM image of the defect which is etched by focused ion beam tool of SEM.

When compared to literature, Figure 2.19 - Figure 2.22 indicates that the growth temperature of the grown sample was slightly higher, since the microvoids shown in

Figure 2.21 have a triangular shape. Moreover, Figure 2.22 indicates that some of the defects observed are substrate related, since the defects starts to form at the substrate interface. Furthermore, needle defects are observed showing that the substrate preparation was not as good as targeted.

The defect density calculated from nomarski micrographs shown in Figure 2.23 is around 533 cm^{-2}. If the growth of HgCdTe is close to the optimal conditions, a common pattern which is called as crosshatch may be observed on the HgCdTe surface. The crosshatches stem from lattice mismatch [68]. M.Martinka et al. [68] concluded that the crosshatches consist of three sets of lines parallel to the $[2\bar{3}1]$, $[\bar{2}13]$ and $[0\bar{1}1]$ directions which are illustrated in Figure 2.24.

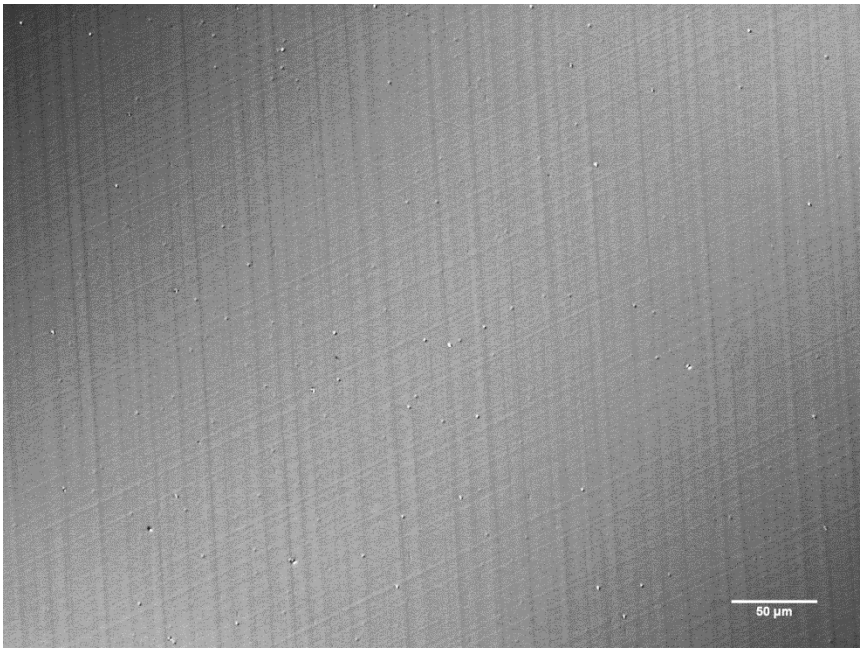

Figure 2.23 Nomarski micrographs of the grown HgCdTe layer surface.

.

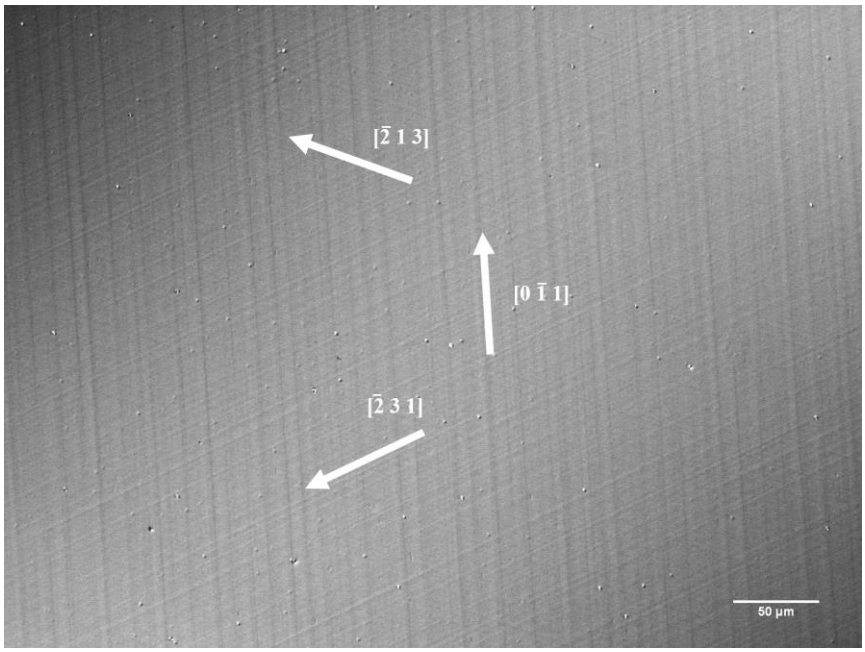

Figure 2.24 Crosshatches visible on the grown HgCdTe surface with $[\bar{2}\,3\,1]$, $[\bar{2}\,1\,3]$ and $[0\,\bar{1}\,1]$ vectors.

The lattice constant of $Cd_{1-x}Zn_xTe$ can be expressed by [20]:

$$a = 6.4810 - 0.3773x \quad °A \tag{2.2}$$

The Zn mole fraction of the utilized CdZnTe substrate is determined with Global Fit software of Rigaku. The Zn mole fraction is determined as 0.038. Using Equation (2.2) the lattice constant of the substrate is calculated as 6.4668 °A. The lattice constant of the grown sample is calculated by using Equation (1.15) and determined as 6.4688 °A corresponding to a substrate with Zn mole fraction of 0.0324. There is a little lattice mismatch resulting in crosshatch pattern as seen in Figure 2.23.

2.4 Fabrication of Test Arrays

The most commonly used method to fabricate HgCdTe photodiodes is to make simple n-on-p homojunctions by ion implantation into vacancy doped p-type layers. Longer minority carrier diffusion length in p-type material and the possibility of achieving longer minority carrier lifetime make n-on-p configuration being the reason of choice for comparable carrier concentration with n-type material [69], [70].

Rogalski and Larkowski indicated that the diffusion-limited R_0A product of p-on-n junctions is larger than that of n-on-p structures because of the lower minority carrier diffusion length in the p-on-n structures. Hence, holes has lower mobility [69].

An important benefit of the p-on-n device structure is that the n-type doping control is easy in the range of $10^{14} – 10^{15}$ cm^{-3}. However the p-type doping control in the n-on-p structures is difficult at these low levels. Due to low n-type doping in the base region, they have longer minority carrier lifetimes.

As can be seen from Figure 2.7, the grown HgCdTe layer has p-on-n device structure. The grown sample is 20x20 mm^2. For fabrication process, 100x100 pixel array with 30 μm pitch mask is used. The steps of fabrication process are as follows.

- Firstly, alignment markers were placed with photolithography method.
- Mesa photolithography was done, and the layer was etched up to the half of the absorber layer.

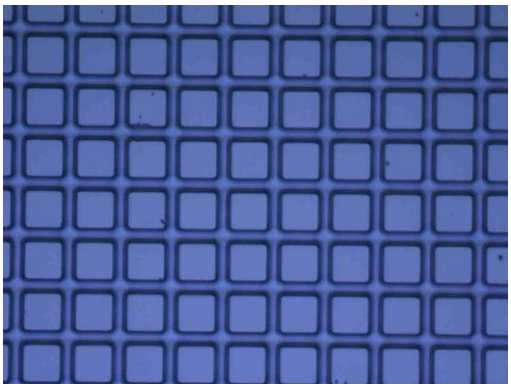

Figure 2.25 Mesa structures on the grown HgCdTe layer.

- As a passivation layer, CdTe was coated in the MBE system. Before passivation coating, the layer was etched in a bromine based solution to remove any oxidized layer. HgTe layer (grown for better ohmic contact formation) was left unetched during etching.
- Passivation layer was opened to reach HgTe layer and ohmic contact metals were coated.
- An insulating layer was coated.

- Insulating layer was opened to reach ohmic contact metals and UBM (Under Bump Metallization) and then In were coated.

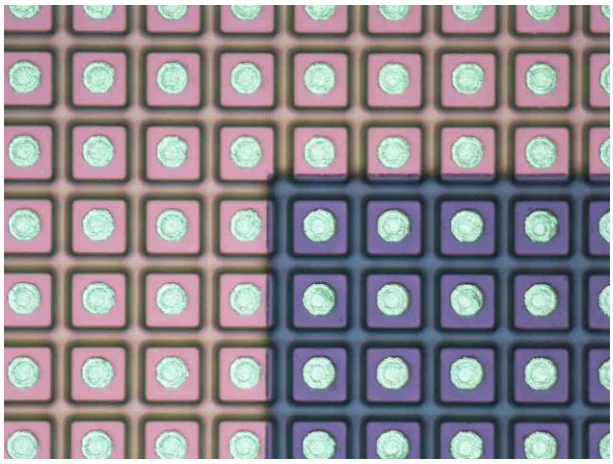

Figure 2.26 100x100 support array after In coating.

After In coating, the support array is ready to couple with fan-out. Flip-chip bonding process is done under formic acid. It helps to break oxide layer on In bumps and the bumps can gather on UBM easily, and uniform In bump heights can be obtained. When force is applied to bond the support array and the fan-out, short and open pixels may be observed if In bumps' heights are different. Because force is not applied uniformly due to different bump heights.

The thermal expansion coefficients of the support array and the fan-out or ROIC which are made from Silicon are different. CTE of Si is 2.60 and that of HgCdTe is around $5x10^{-6}$ K^{-1} [71], therefore for each cycle from room temperature to cryogenic temperatures and then again to room temperature, In bumps may be broken and pixels become open. In order to avoid this drawback, underfill epoxy is applied to the gap between the array and the fan-out or ROIC. Against the stress resulting from the thermal expansion difference, the hybridized structure becomes robust mechanically.

After underfill, the array is thinned. The reason of this is to decrease the effect of thermal expansion difference, since the array becomes more flexible. Moreover crosstalk through the substrate is decreased.

The steps of process is summarized in Figure 2.27.

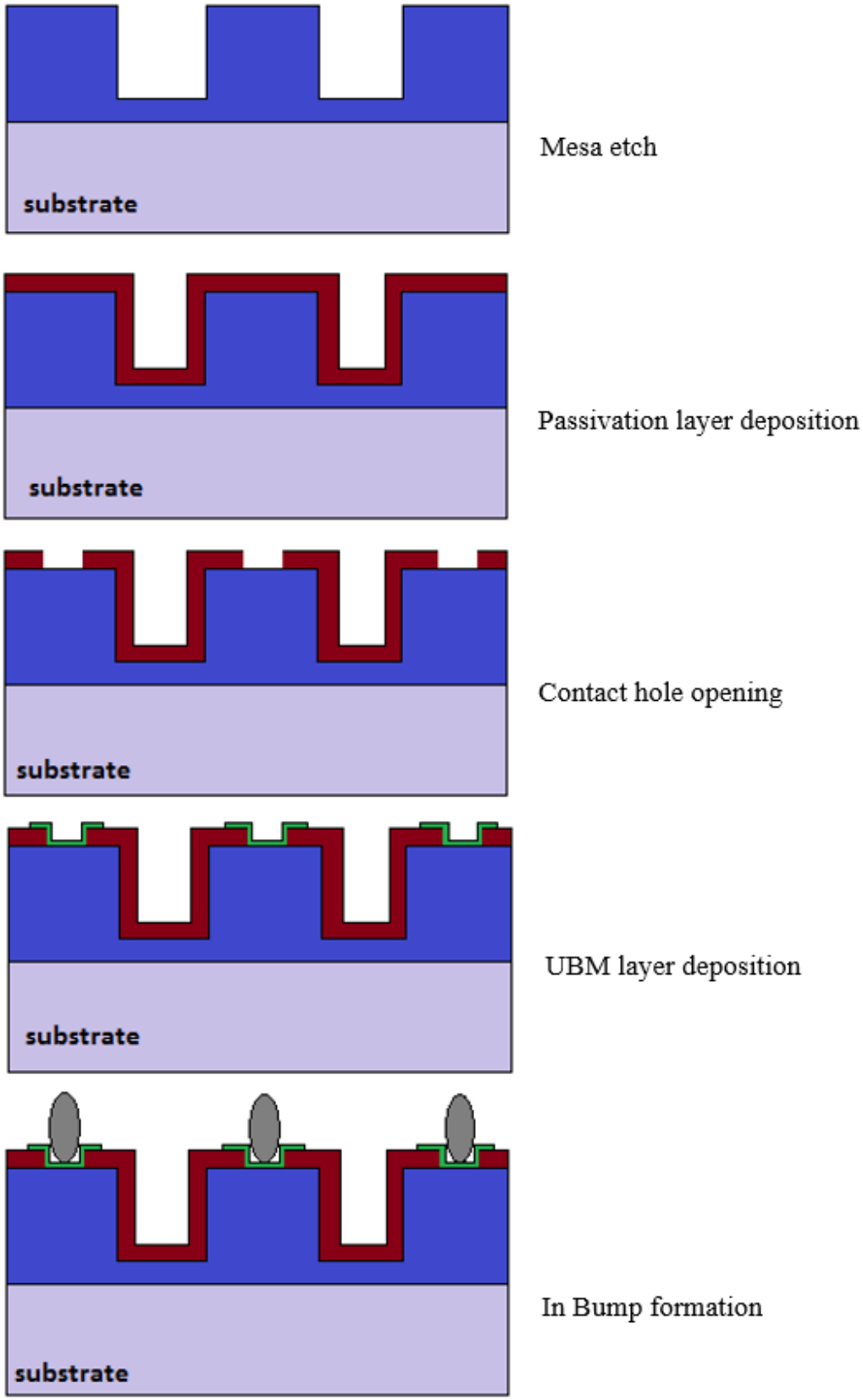

Figure 2.27 SWIR HgCdTe support array fabrication steps.

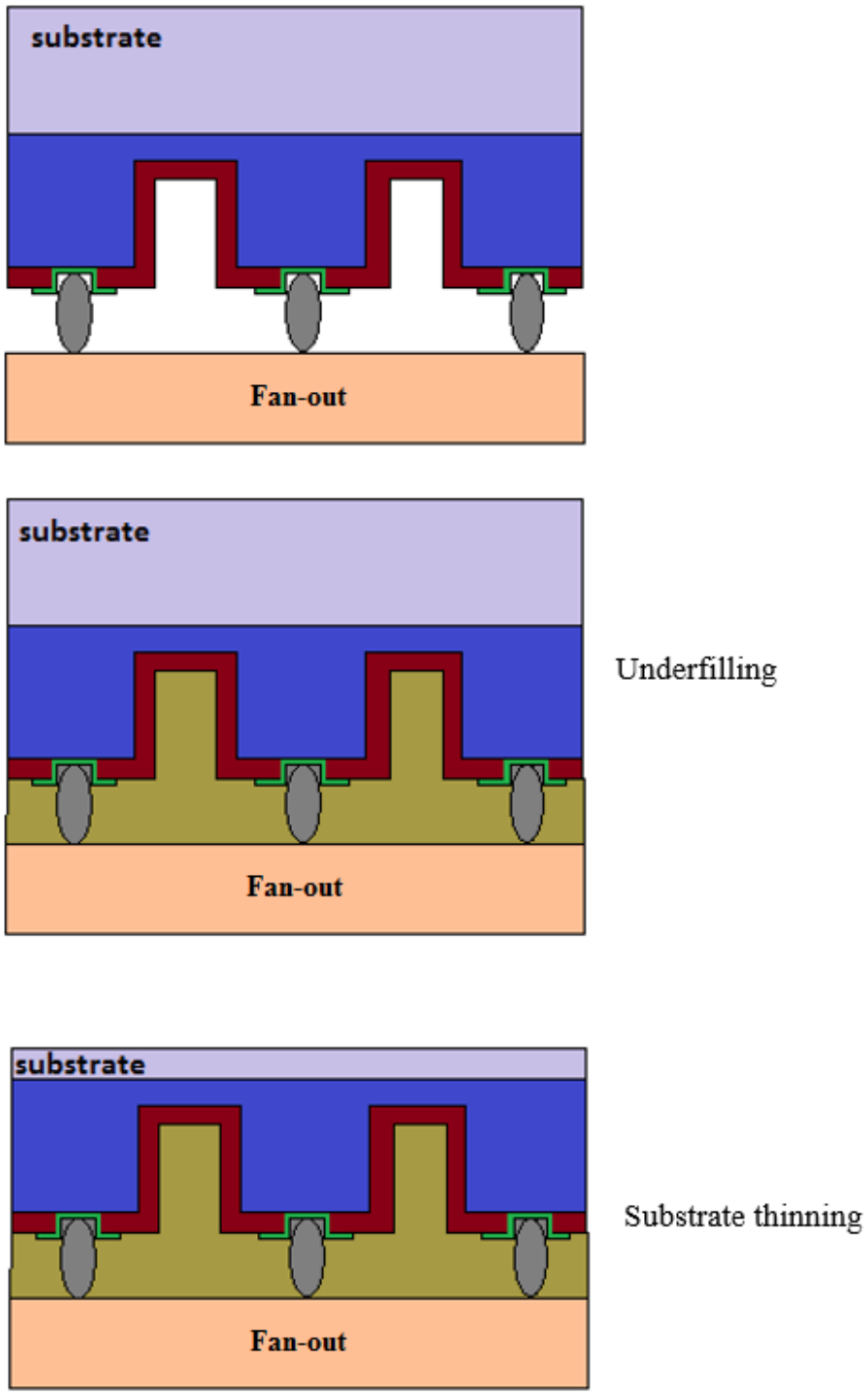

Figure 2.27 SWIR HgCdTe support array fabrication steps. (continued)

The test arrays were fabricated from the grown HgCdTe layer which was deposited on home-polished CdZnTe substrates. It can be concluded from the defects analyzed with nomarski and SEM that the quality of the substrate affects the grown layer on it badly. Furthermore, the X-Ray diffraction pattern of the substrate promotes the poor quality of the substrate. The fabricated test arrays were characterized electrically and optically to analyze the effects of the substrate and growth conditions, and to make a conclusion about the diode performance. The results are given in the following chapter.

CHAPTER 3

DETECTOR CHARACTERIZATION AND DISCUSSION

Electrical and optical characterization of the layers were performed with the test array with 30 μm pitch pixels. It is important to note that there is no anti reflection coating. The hybridized support and fan-out structure was wire bonded to an 84 pin LCC package shown in Figure 3.1. Each active pin corresponds to 25 pixels connected in shunt.

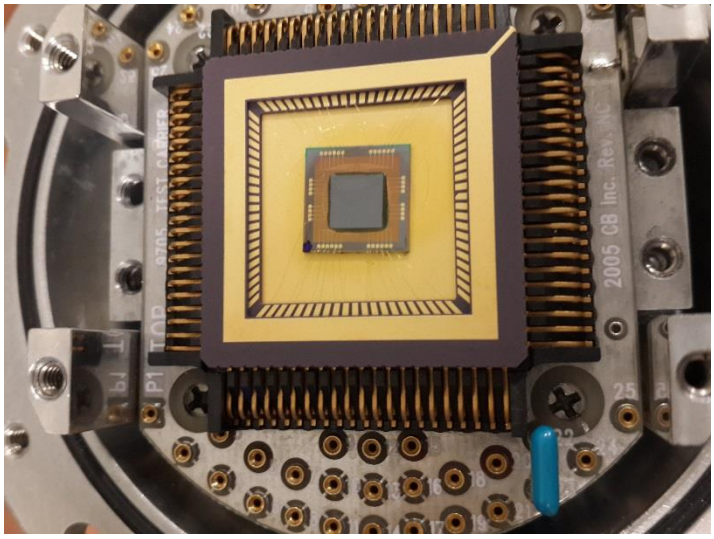

Figure 3.1 The hybridized support wire bonded to 84 pin LCC.

3.1 Dark Current Measurements

Before measuring the dark current with respect to temperature, all (5x5) pixels groups were measured with Keithley 6430 source-meter at room temperature in a test dewar

in order to identify the pixel groups which have similar I-V characteristics. Therefore the pixel groups with the same characteristics were connected in shunt for reliable electrical and optical measurements. Figure 3.2 shows pixel groups with similar characteristics at room temperature.

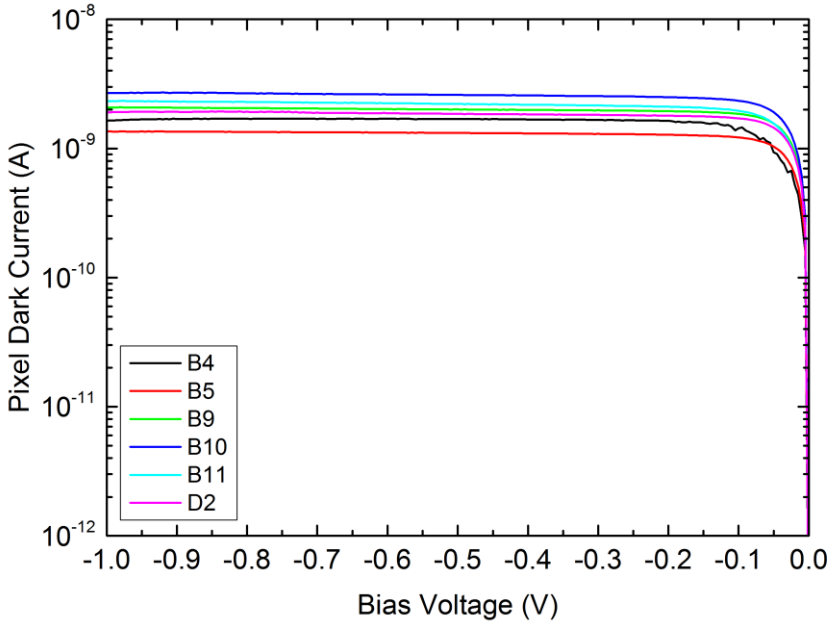

Figure 3.2 Pixel dark current of pixel groups with similar characteristics at room temperature.

Before measuring current with respect to temperature, pixels in Figure 3.2 were connected in shunt via wire bonding. Those pixels have an average dark current of 2 nA at room temperature under 1 V reverse bias. Figure 3.4 shows dark current density vs bias voltage at different temperatures measured with He cryostat shown in Figure 3.3 and Keithley 6430 source meter. Figure 3.4 indicates that the dark current density is about 0.1 mA/cm^2 at 290K, 10 μA/cm^2 at 250K and 0.1 μA/cm^2 at 200K under 1 V reverse bias. As seen from Figure 3.4, the dark current is almost constant up to 1 V reverse bias at 290 K indicating that the dominant dark current mechanism is diffusion at this temperature, and there is no considerable tunneling and generation-recombination (G-R) current components. Figure 3.6 shows the dark current activation energy under 100 mV reverse bias voltage. The activation energy is E_g/1.24 which

indicates that additional (in addition to diffusion) dark current components appear as the detector is cooled to lower temperatures.

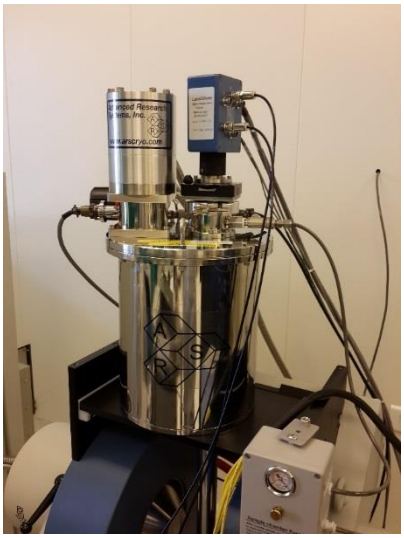

Figure 3.3 He cryostat used for dark current measurement.

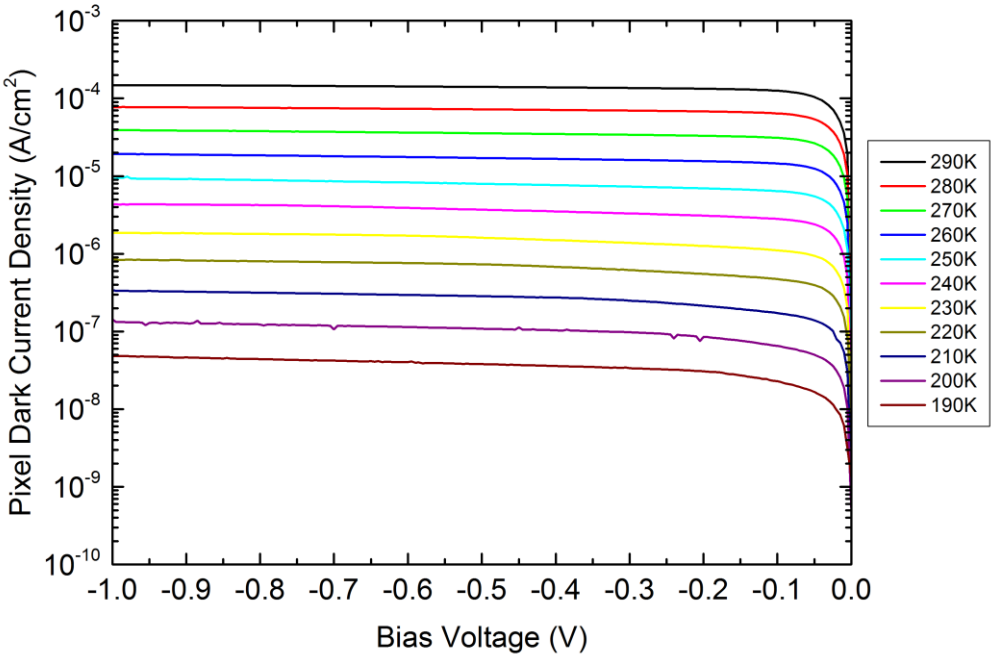

Figure 3.4 Pixel dark current density derived from 5 pixel groups (each group consists of 25 pixels) vs bias voltage at different temperatures.

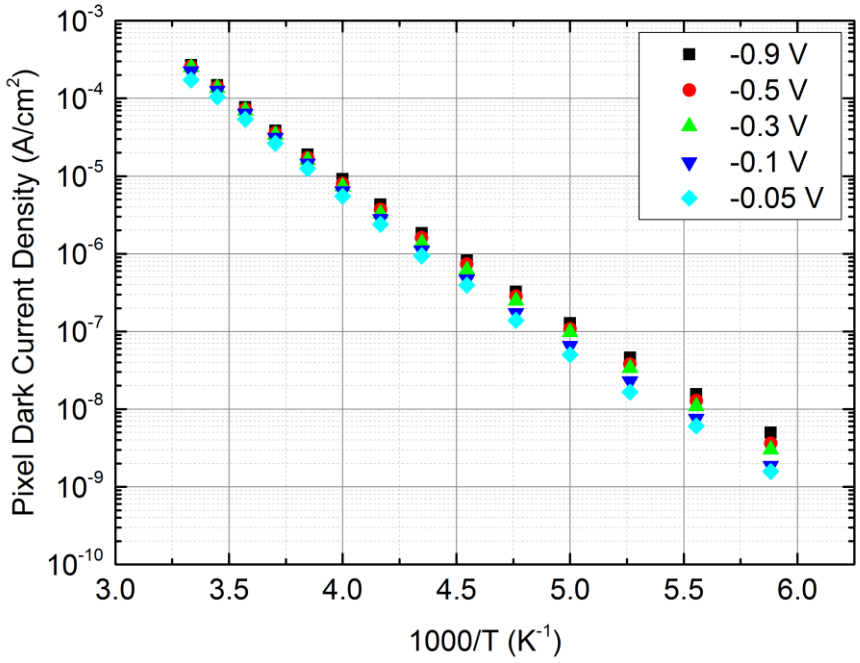

Figure 3.5 Pixel dark current density vs 1000/T under different reverse bias voltages.

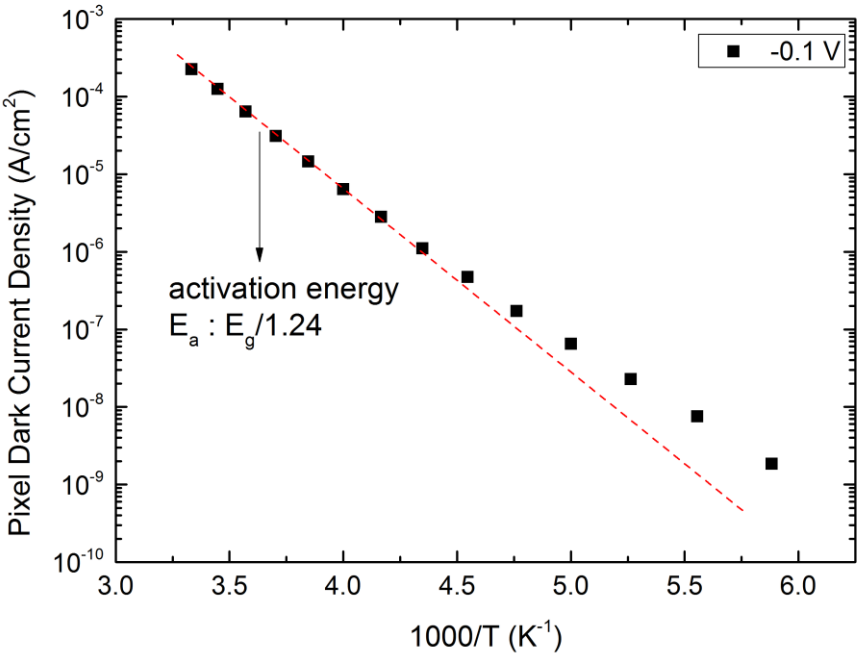

Figure 3.6 Dark current activation energy under 100 mV reverse bias.

3.2 Responsivity and Quantum Efficiency

In order to obtain responsivity spectrum, the following procedure is performed.

- Calculation of blackbody responsivity,
- Measurement of normalized spectral response,
- Multiply blackbody exitance with normalized spectral response,
- Calculate peak factor (divide total exitance with exitance multiplied with normalized spectral response),
- Multiply blackbody responsivity with peak factor to find peak responsivity,
- Multiply normalized spectral response with peak responsivity to find responsivity spectrum.

In order to obtain blackbody responsivity, a blackbody with chopper, a preamplifier and a lock-in amplifier were used. The instruments shown in Figure 3.8 were used as indicated in Figure 3.7. The blackbody was set to 800°C and the chopper in front of the blackbody source was at 11 Hz speed. Due to chopper, the background radiation is eliminated. The detector was placed in front of the blackbody 30 cm away. The detector was connected to the preamplifier, and the output signal of the preamplifier was fed into the lock-in amplifier measuring the signal at 11 Hz. The computer then divided the signal by the optical power falling on the detector, which is calculated by the user once the distance of the detector to the blackbody, detector area, window transmission and the diameter of the blackbody aperture are known. With this setup, the voltage responsivity of the detector – preamplifier combination was measured. To find the current responsivity of the detector, the measured voltage responsivity was divided by the trans-impedance gain of the preamplifier.

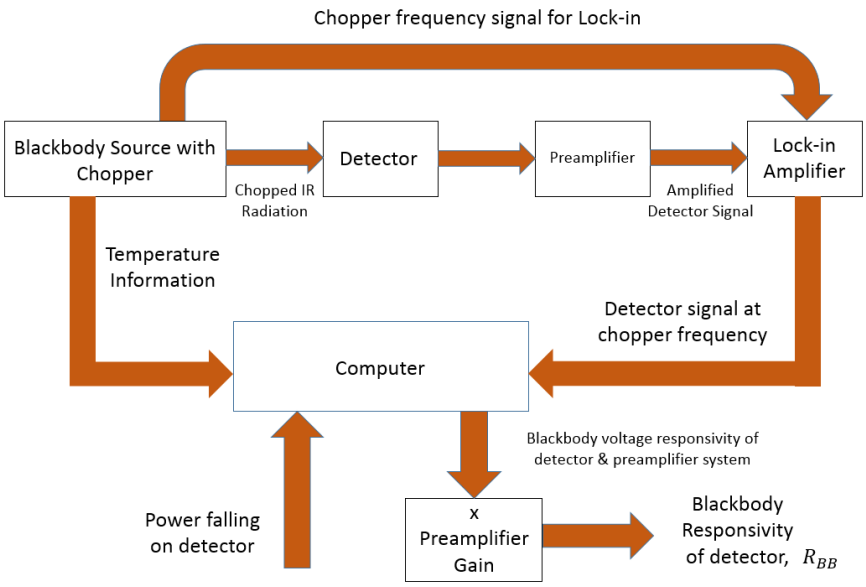

Figure 3.7 Blackbody responsivity measurement setup illustration.

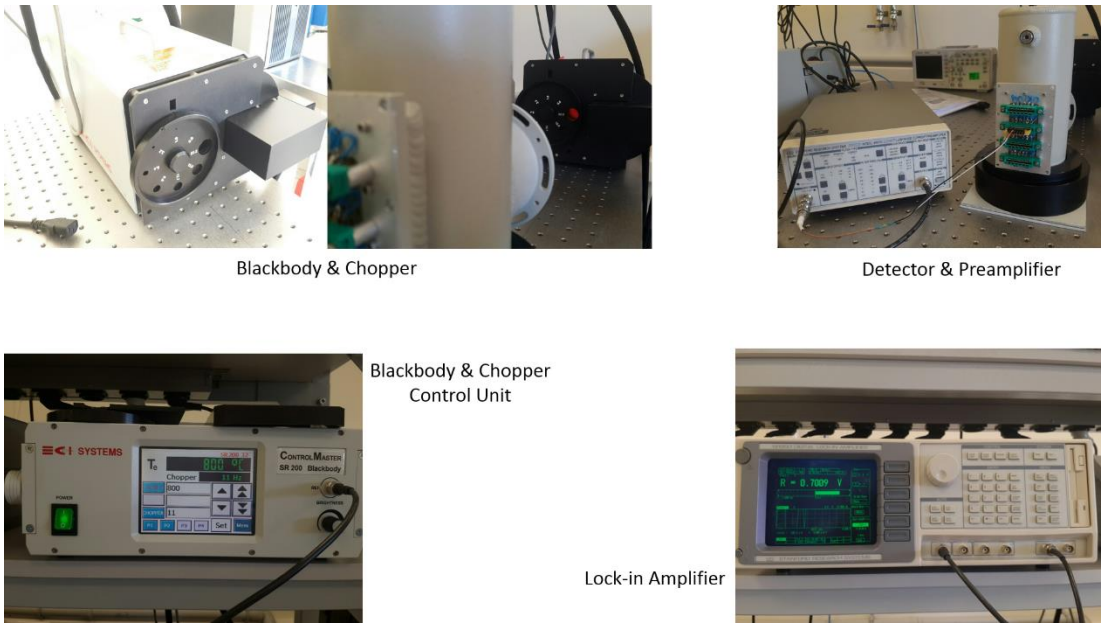

Figure 3.8 The instruments used in measurement of blackbody responsivity.

Spectral response in arbitrary unit was obtained with FTIR. The background signal was measured through MCT detector which is also sensitive to SWIR band. Then the signal was measured through fabricated detector array. The detector was at room

temperature in test dewar. The obtained normalized responsivity spectrum with arbitrary unit under 100 mV reverse bias is given in Figure 3.9.

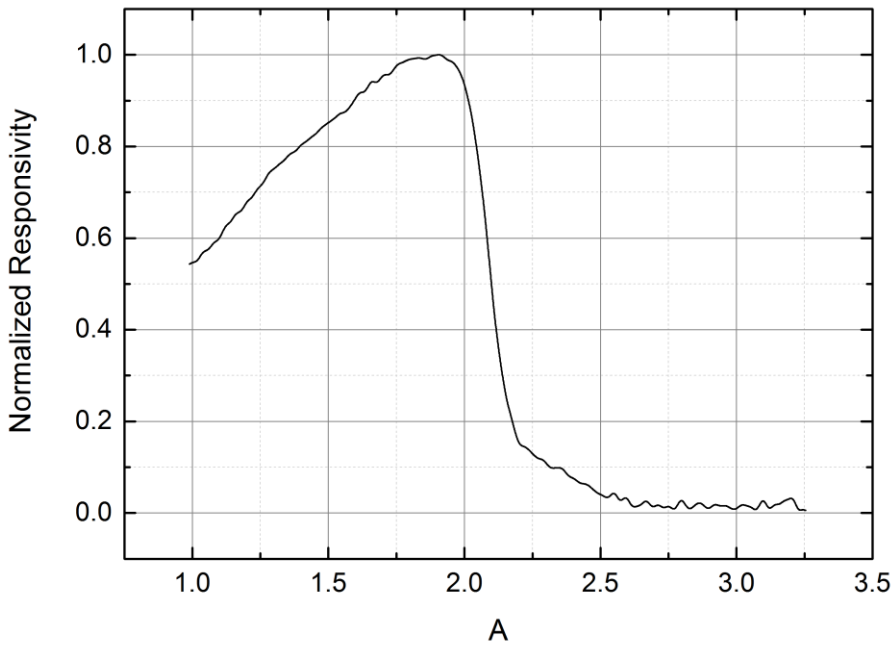

Figure 3.9 The normalized responsivity spectrum with arbitrary unit under 100 mV reverse bias at room temperature.

The blackbody responsivity is found as 1.2755×10^{-1} A/W and peak factor is calculated as 7.88. The peak responsivity is found as 1.0 A/W by multiplying the peak factor with blackbody responsivity. The cut-off wavelength is about 2.17 μm at room temperature where responsivity is half of the peak responsivity.

Quantum efficiency is calculated from peak responsivity. Equation (3.1) is used for responsivity in terms of quantum efficiency.

$$R = \eta g \frac{\lambda}{1.24} \ (\mathrm{A/W}) \qquad (3.1)$$

$$1 = \eta \frac{2}{1.24} \quad \Rightarrow \quad \eta \cong 62\%$$

Peak responsivity corresponds to 2 μm wavelength, and as a result quantum efficiency is found as about 62% at room temperature under 100 mV reverse bias. It should be noted that there is no anti reflection coating. Figure 3.10 shows the quantum efficiency spectrum with respect to the wavelength. The average quantum efficiency is about 65% up to 2 μm wavelength.

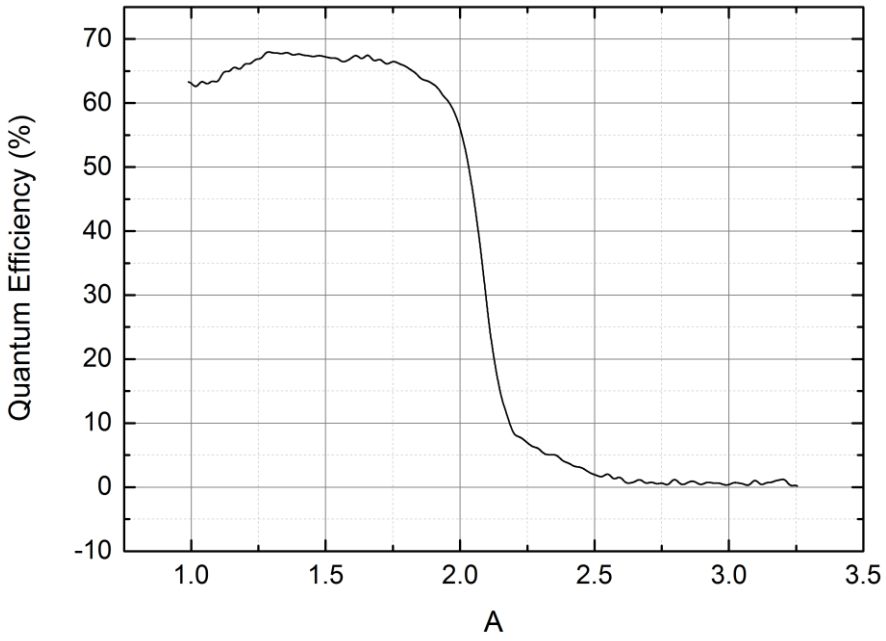

Figure 3.10 Quantum efficiency spectrum of the grown sample.

Theoretical quantum efficiency was calculated using Equation (3.2),

$$\eta = \frac{\eta_{\text{int}}(1-r)(1-e^{-\alpha t})}{1-re^{-\alpha t}} \tag{3.2}$$

where r is the reflection coefficient, t is the thickness of the absorption layer and α is the absorption coefficient. The internal quantum efficiency is nearly unity for common low bandgap IR detector materials.

$$\alpha = \alpha_g \exp[\beta(\hbar\omega - E_g)]^{1/2} \quad \mathrm{cm}^{-1}$$

$$where$$

$$\alpha_g = -65 + 1.88T + (8694 - 10.31T)x \quad \mathrm{cm}^{-1} \tag{3.3}$$

$$\beta = -1 + 0.083T + (21 - 0.13T)x \quad \mathrm{eV}^{-1}$$

$$E_g = -0.295 + 1.87x - 0.28x^2 + (6 - 14x + 3x^3)(10^{-4})T + 0.35x^4 \quad \mathrm{eV}$$

$$r = \left[\frac{n-1}{n+1}\right]^2 \tag{3.4}$$

where n is the refractive index of the surface, and n is assumed as 2.65 which is the refractive index of CdTe.

Absorption coefficient is 1.3907×10^4 cm^{-1}. The absorbing layer thickness is about 2.53 μm.

Calculation according to Equation (3.2) shows that the theoretical quantum efficiency without anti reflection coating is 77.67% at 230K. The difference between theoretical and experimental quantum efficiency is probably the discrepancy in the refractive index of CdTe which can change the reflection from the surface. It should be noted that cut-off wavelength is almost unchanged with temperature in SWIR band. Therefore responsivity and quantum efficiency spectrum of the grown sample is almost same for different operating temperatures

3.3 Noise Measurement and Detectivity

Noise measurement under dark conditions was performed with lock-in amplifier on 125 pixels in shunt at room temperature. The noise measurement and peak detectivity calculation results at room temperature under various bias voltages can be seen from Figure 3.11 and Figure 3.12. The maximum peak detectivity is 4.36×10^{10} $cmHz^{1/2}/W$ under 100 mV reverse bias at room temperature. The corner frequency is about 150 Hz.

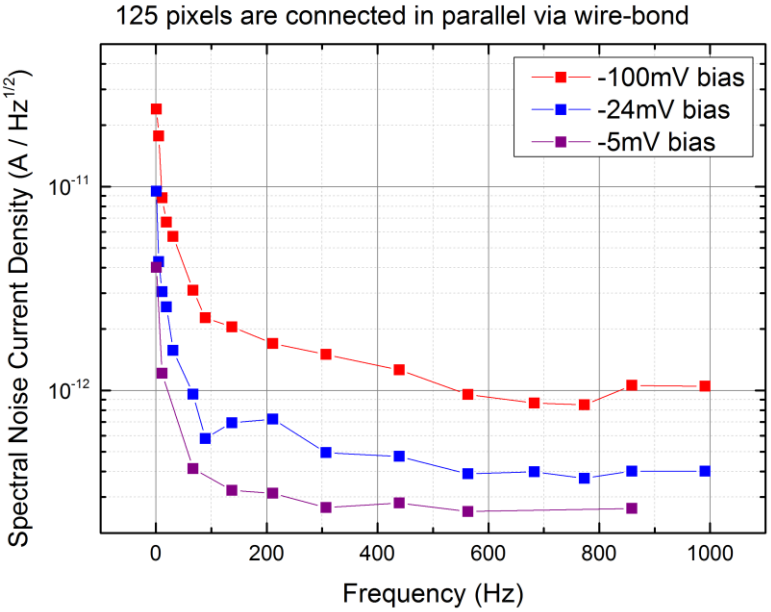

Figure 3.11 Spectral noise under different bias voltages at room temperature.

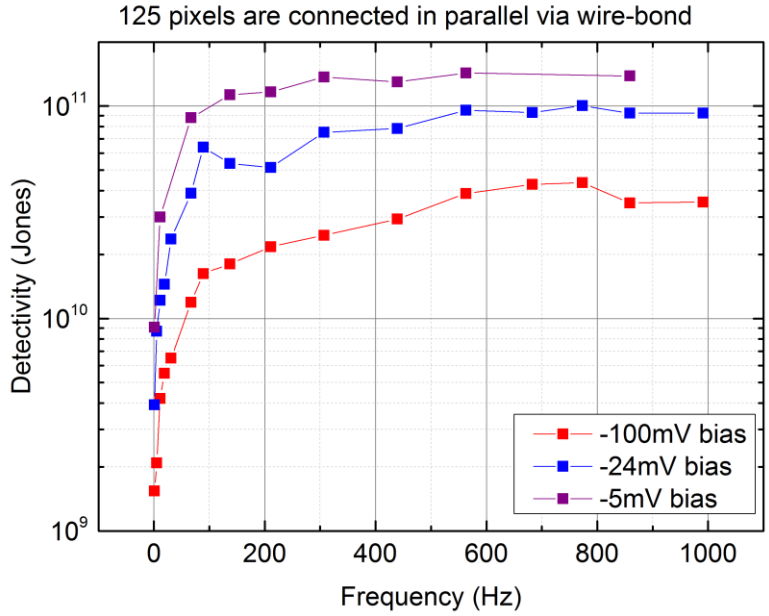

Figure 3.12 Peak detectivity under different bias voltages at room temperature.

The detectivity was also calculated theoretically. In the calculation, shot noise and thermal (Johnson) noise which are expressed as in Equation (1.10) and (1.8), respectively were taken into account.

Dark current was measured, and dynamic resistance is calculated for noise calculations. The dark current is 4.6×10^{-8} A, and the dynamic resistance of the detector is 1×10^{7} Ω under 100 mV reverse bias at room temperature. Detectivity is calculated as 1.17×10^{11} cmHz$^{1/2}$/W under dark conditions. The theoretical peak detectivity is 2.7 times of the experimental peak detectivity. The reason of this difference is that 1/f noise is ignored in the theoretical calculation and also there is some extra noise coming from measurement setup.

3.4 Dark Current Modeling

Current – voltage (I-V) measurements are generally used to specify the performance of an infrared (IR) detector. The characteristics of an IR detector's I-V depends on the dominant current limiting mechanism in the device. Temperature, applied bias voltage and detector bandgap affect the dark current components.

In recent years, due to advancements in material growth and device processing, detectors with longer cut-off wavelength have become important. Moreover, to be able to achieve a good detector, the dark current mechanisms should be given more importance.

Diffusion Current:

The thermal diffusion of minority carriers (holes from the n-region and electrons from the p-region) create a dark current component. The diffusion current can be expressed as [72]–[76],

$$J_{diff} = \sqrt{qkT}\, n_i^2 \left[\sqrt{\frac{\mu_n}{\tau_n}} \frac{1}{N_A} + \sqrt{\frac{\mu_p}{\tau_p}} \frac{1}{N_D} \right] \left(e^{\frac{qV_r}{nkT}} - 1 \right) \quad \text{long diode assumption}$$

$$J_{diff} = q n_i^2 \left[\frac{w_p}{\tau_n} \frac{1}{N_A} + \frac{w_n}{\tau_p} \frac{1}{N_D} \right] \left(e^{\frac{qV_r}{nkT}} - 1 \right) \quad \text{short diode assumption} \tag{3.5}$$

Generation-Recombination (G-R) Current:

If depletion region has high density of Schokley-Read-Hall recombination centers, then this type of current may become a dominant dark current mechanism. The SRH

center may be introduced to the layer during growth or process. The G-R current density is expressed as [72], [74], [76],

$$J_{gr} = \frac{q n_i w \sqrt{V_{bi} - V_r}}{2\tau} \left(e^{\frac{qV_r}{2kT}} - 1 \right)$$

$$\text{where} \quad w = \sqrt{\frac{2\varepsilon_0 \varepsilon_r}{q} \frac{N_A + N_D}{N_A N_D}} \tag{3.6}$$

Trap assisted tunneling (TAT) Current:

Tunneling of the carriers from the trap states in the depletion region or in the quasi neutral region to the empty band states cause this type of dark current. It is illustrated in Figure 3.13. The TAT current density is expressed as [72]–[76],

$$A = -qN_t 6e5 / (Eg - Et)$$

$$B = -1.7e7 w \sqrt{Eg} \sqrt{(Eg - Et)^3}$$

$$w = \sqrt{\frac{2\varepsilon_0 \varepsilon_r}{q} \frac{N_A + N_D}{N_A N_D}} \tag{3.7}$$

$$J_{tat} = A(V_{bi} - V_r) e^{\frac{B}{\sqrt{V_{bi} - V_r}}}$$

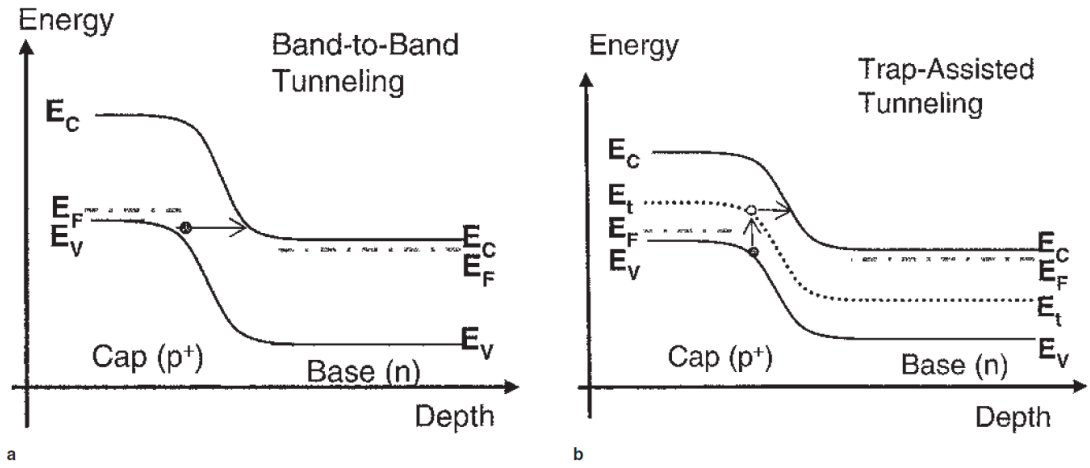

Figure 3.13 Energy band diagrams for HgCdTe illustrating tunneling process. a) The band diagram is for possible band to band tunneling transition. b) The band diagram is for possible TAT [76].

Ohmic Current:

This current is responsible from the surface or dislocation related bulk leakage currents which exhibit shunt-like behavior in the junction performance.

Dark current modeling was performed in order to identify the dominating dark current components. Before fitting the data, the series resistance which is calculated at large forward bias to the diode was extracted. The series resistance is around 1.2 KΩ which is higher than expected.

The shunt resistance, R_{shunt} is found as 10^9 Ω, and the diffusion life time, τ, is found as 4.5 nsec. Figure 3.15 indicates that diffusion current mechanism is the dominant mechanism at 230K for reverse biases up to 1 V. The R_0A product is 2.48×10^4 Ω and maximum dynamic resistance R_{dyn} is around 4×10^9 Ω at 230K.

The dark current modeling at 190K indicates that the G-R and diffusion lifetimes are 1.8 μsec and 0.2 nsec, respectively. The shunt resistance is 2.5×10^{10} Ω.

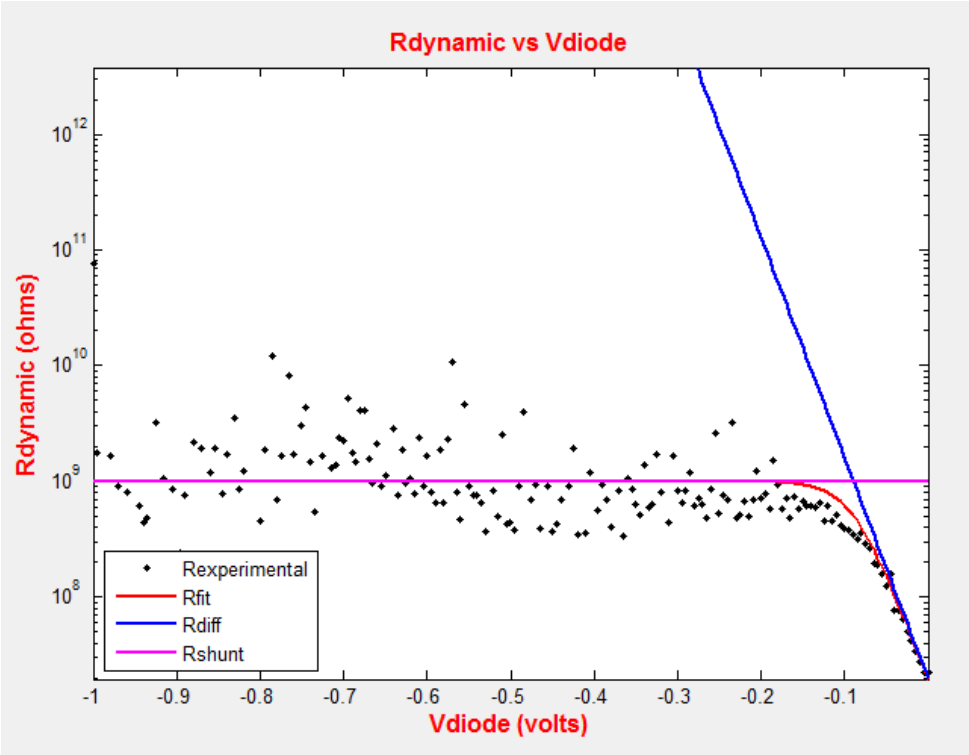

Figure 3.14 Dynamic resistance fit of the detector array at 230K.

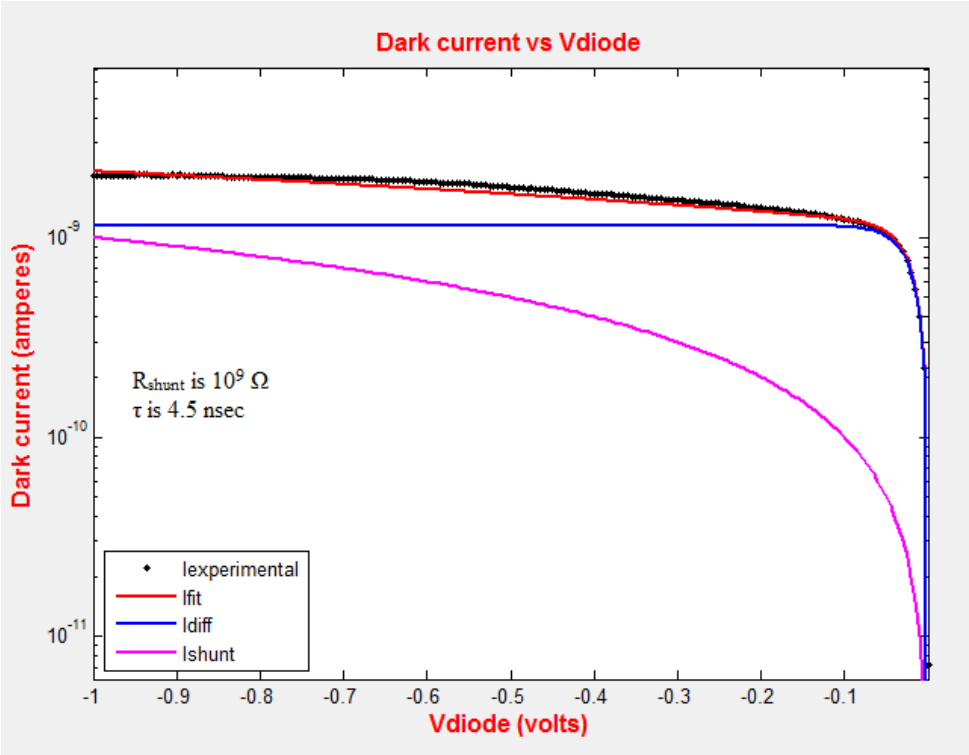

Figure 3.15 Dark Current fit of the detector array at 230K.

3.5 Capacitance – Voltage Measurement

The built-in potential of a pn junction and the doping concentration can be obtained by measuring the depletion capacitance with respect to applied voltage to the junction. The capacitance can be expressed as:

$$C = \varepsilon \frac{A}{W} \tag{3.8}$$

where ε is the permittivity, A is the area of the junction, and W is the depletion width. Depletion width is given by:

$$W = \sqrt{\frac{2\varepsilon}{q} \frac{N_A + N_D}{N_A N_D} (V_{bi} - V_{bias})} \tag{3.9}$$

where N_A and N_D are acceptor and donor impurity densities respectively and V_{bi} is the built-in voltage. When reverse bias is increased in magnitude then the depletion width is also increased and as a result the depletion capacitance is decreased.

Equation (3.8) and Equation (3.9) are combined to obtain Equation (3.10)

$$C_A = \sqrt{\frac{q\varepsilon N_{doping}}{2(V_{bi} - V_{bias})}} \qquad \text{per unit area}$$
$$\frac{1}{C_A^2} = \frac{2}{q\varepsilon N_{doping}} (V_{bi} - V_{bias}) \tag{3.10}$$

where N_{doping} is the impurity concentration of the layer. If $N_A >> N_D$ then N_{doping} is equal to N_D..(If $N_D >> N_A$, $N_{doping} = N_A$)

If one plots V_{bias} vs $1/C_A^2$ then impurity concentration and built-in voltage can be calculated easily. The measurements were performed on the circular mesa type diodes which has 400 μm diameter at 77K.

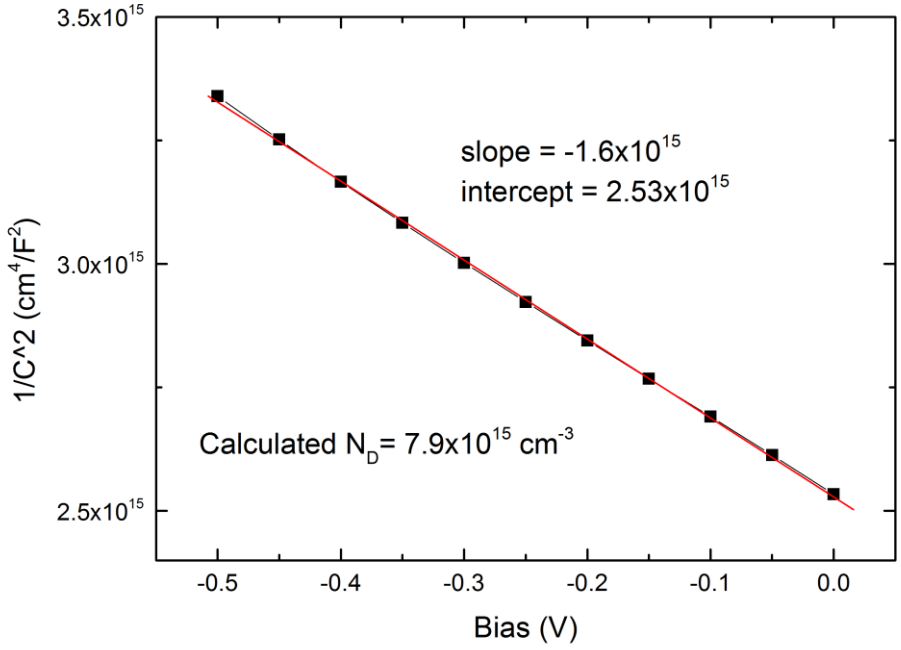

Figure 3.16 $1/C_A^2$ vs voltage characteristic and linear fit of one of the diodes.

The theoretical average depletion capacitance over the bias voltage is calculated as 28.3 pF at 77K. It verifies the observed average experimental value, about 25 pF. Moreover the targeted n-type doping density is about $5x10^{15}$ cm^{-3} which is also comparable with the experimental data, $7.9x10^{15}$ cm^{-3}.

3.6 Deep Level Transient Spectroscopy (DLTS) Measurement

Undesired lattice defects caused by impurities, dislocations etc. can be formed during growth and are usually situated in deep levels of the band gap. Those deep level defects have large capture cross sections, and therefore the minority carrier lifetime is decreased which decreases the performance of the detector.

Deep Level Transient Spectroscopy is a method to study deep level defects by monitoring the capacitance transient. This method provides activation energy, capture cross section and trap concentration.

As stated before, the theory behind the DLTS method is the capacitance transient. This transient is obtained by giving pulses to the diode at steady-state. A reverse bias

increases the width of the depletion region and hence the depletion capacitance is decreased as stated in Section 3.5. At first, the traps are empty at the steady-state, and due to reverse bias the depletion width is large, and the depletion capacitance is small. Pulse is applied to change the occupancy of the deep states that pulse fills the traps below the fermi level. Pulse from reverse to zero bias is to inject majority carriers and into forward bias is to inject minority carriers. During pulse bias, the depletion width is decreased and therefore the depletion capacitance is increased. When applied pulse bias is removed the depletion width is increased and the depletion capacitance is decreased more due to the captured carriers. Thermal emission of the captured electrons occurs. The emitted electrons are swept out of the depletion region due to electric field and as a result the depletion capacitance reaches the steady state value under reverse bias [77], [78]. This event is illustrated in Figure 3.17.

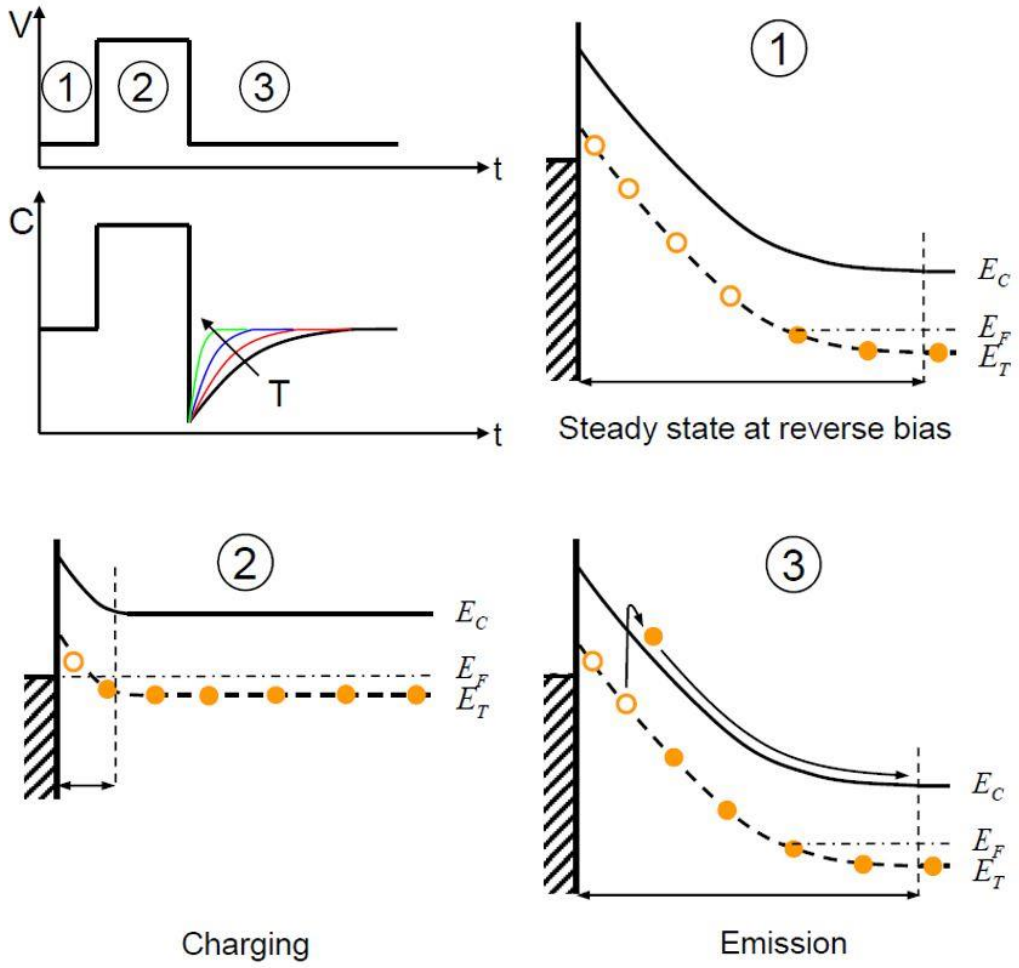

Figure 3.17 DLTS capacitance transient illustration [79].

The capacitance transient with respect to applied bias is illustrated in Figure 3.18

At steady state the depletion capacitance is given as [77]:

$$C_{ss} = A\sqrt{\frac{q\varepsilon(N_D + N_T)}{2(V_{bi} - V_{bias})}} \tag{3.11}$$

where N_T is the trap concentration and A is the diode area. The time dependent capacitance is given by [77]:

$$C(t) = C_{ss}\sqrt{1 - \frac{n_T(t)}{N_D + N_T}} \tag{3.12}$$

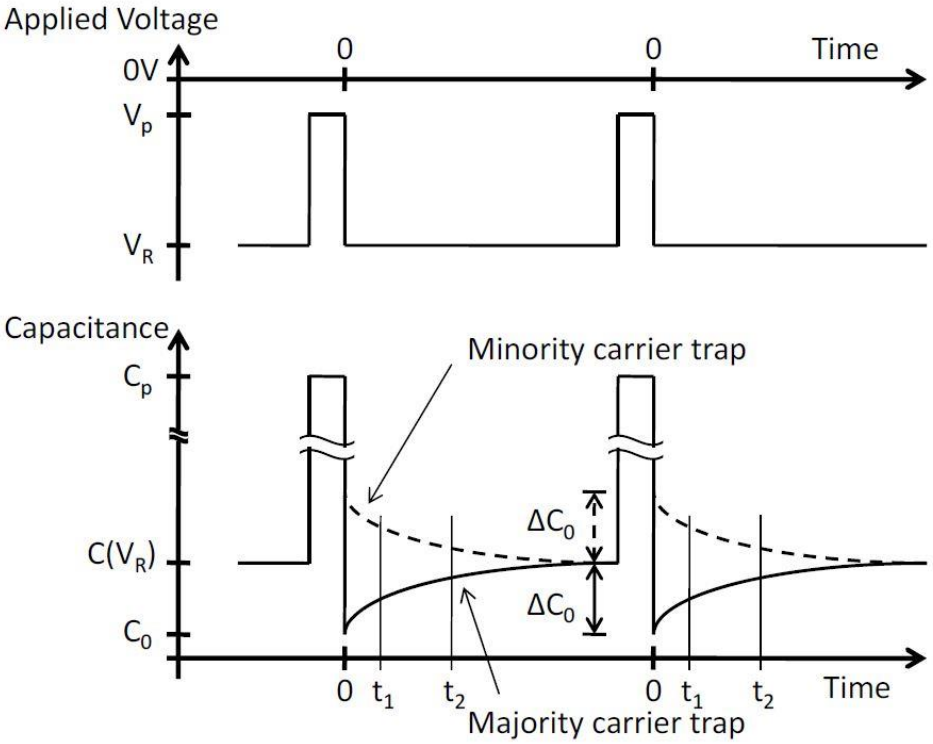

Figure 3.18 Capacitance transient with respect to applied pulse [77].

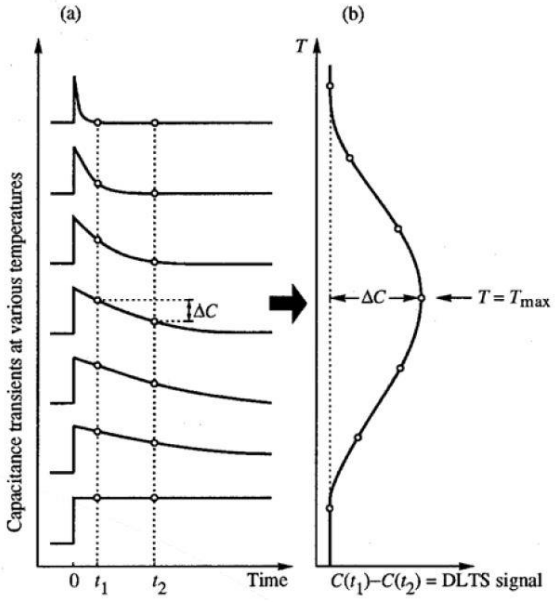

Figure 3.19 a) Capacitance transient at various temperatures b) Corresponding DLTS signal with respect to temperature [80].

To calculate trap density, an empirical formula is expressed by:

$$\frac{\Delta C}{C_{ss}} = \frac{C(t_2) - C(t_1)}{C_{ss}} = -\frac{1}{2}\frac{N_T}{N_D} \tag{3.13}$$

Equation (3.13) is valid for $N_T << N_D$. It should be noted that trap density must be much lower than doping density to be able to obtain meaningful data in DLTS measurements.

In DLTS method, the output signal is the difference between two capacitance values which are sampled at times t_1 and t_2 after pulse bias. If there is a minority trap then DLTS signal shows maxima and if there is a majority trap then DLTS signal shows minima in the spectrum. The output DLTS signal with respect to temperature can be written as,

$$S(T) = C(t_2) - C(t_1) \tag{3.14}$$

S(T) changes with temperature, since the emission rate depends on the temperature. The inverse of the emission rate is known as emission time constant, and at the peak DLTS signal it can be written as [77]:

$$\tau = \frac{t_2 - t_1}{\ln(t_2 / t_1)} \quad \text{and emission rate} \quad e_n = \frac{\ln(t_2 / t_1)}{t_2 - t_1} \tag{3.15}$$

The DLTS signal becomes maximum when the trap emits the carriers in the rate window [77], [80]:

$$e_n = \sigma_n v_{th} N_c \exp(-\frac{E_a}{kT}) \tag{3.16}$$

where σ is the capture cross section of the electron v_{th} is the thermal velocity and N_c is the effective density of states in the conduction band and E_a is the thermal activation energy of the traps. The thermal velocity and the effective density of states are given by:

$$v_{th} = \sqrt{\frac{3kT}{m_e^*}} \quad \text{and} \quad N_c = 2\sqrt{\left(\frac{2\pi m_e^* kT}{h^2}\right)^3} \tag{3.17}$$

Rearranging Equation (3.16) using Equation (3.17), e_n can be written as:

$$\begin{aligned} e_n(T) &= AT^2 \exp(-\frac{\Delta E}{kT}) \\ \frac{e_n(T)}{T^2} &= A\exp(-\frac{\Delta E}{kT}) \\ \ln(\frac{e_n(T)}{T^2}) &= \ln A - \frac{\Delta E}{kT} \\ A &= \frac{4\sqrt{6}\sigma k^2 \pi^{3/2} m^*}{h^3} \end{aligned} \tag{3.18}$$

If one plots $\ln\left(\frac{e_n}{T^2}\right)$ vs $\frac{1}{T}$, the activation energy and capture cross section can be found from slope and interception respectively.

When rate window is changed then the peak temperature of the DLTS signal is also shifted. Because DLTS signal becomes maximum when emission rate is same with the rate window. Figure 3.20 shows the DLTS spectrum of the one diode which has 400μm

diameter. The rate windows are 0.2 ms, 0.1 ms, 0.05 ms and 0.02 ms. The filling pulse width is 100 µs. The peak temperatures of the signals are chosen as in Figure 3.20.

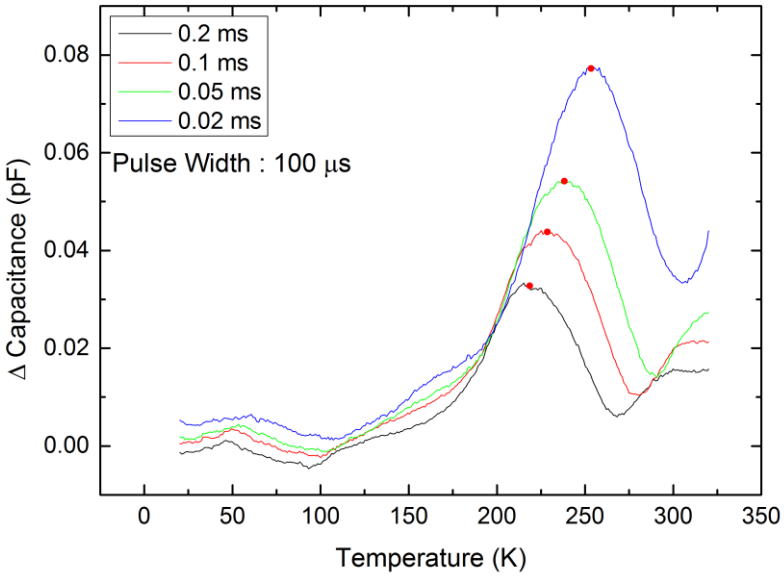

Figure 3.20 The DLTS spectrum of the test diode with marked peaks.

Then an Arrhenius plot is drawn with respect to marked points as in Figure 3.21

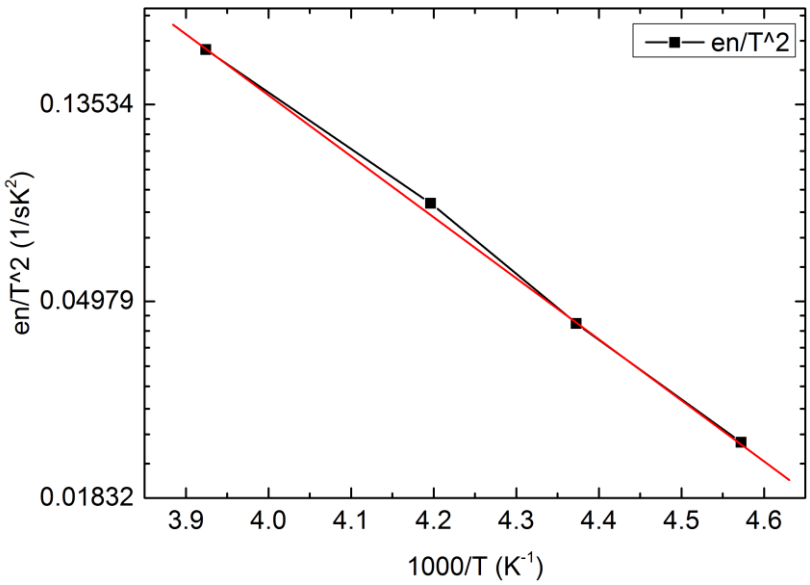

Figure 3.21 Arrhenius plot of e_n/T^2 vs 1000/T.

Using Equation (3.18), the activation energy, E_a, is calculated as about 267 meV and the capture cross section, σ calculated as $2.06x10^{-17}$ cm^2 and the trap concentration is about $3.2x10^{13}$ cm^{-3}. Those values make sense, since the bandgap of the sample is about 555 meV, and the trap activation energy corresponds to almost half of the bandgap energy. It is well known that the mid-gap traps are generally the effective ones. Indeed there is another hole trap at high temperatures. Since HgCdTe material is broken at temperatures higher than 80 C, it could not be resolved effectively.

L.Gelczuk et al. reported a study about the defects types analyzing the DLTS line amplitude and shape [78]. They summarized the defects types according to DLTS spectrum.

If the trap is a point defect, then one can generally obtain the followings [78]:

- DLTS peaks are symmetric and narrow,
- DLTS peaks are almost stable with increasing pulse width,
- DLTS signal shows saturation for long pulse duration, i.e. logarithm of the pulse width vs DLTS signal peaks is almost constant. (exponential capture law),

If the trap is an extended defect, then one can observe opposite features [78]:

- DLTS peaks can be symmetrically or asymmetrically broadened,
- DLTS signal maxima is almost constant and its high temperature side intersects with each other after normalizing,
- DLTS signal maxima shifts to lower temperatures and high temperature side intersects with each other after normalizing,
- DLTS signal shows no saturation with increasing pulse duration, i.e. logarithm of the pulse width vs DLTS signal peaks is almost linear. (logarithmic capture law)

DLTS measurements for different pulse widths were performed. It is observed that the amplitudes of the signals are almost stable with increasing pulse width, and DLTS signal amplitude with respect to logarithm of pulse width show an almost constant characteristic. It can be concluded that the found defect is a point defect. L.Gelczuk et al. claim that point defects are formed from impurities [77].

3.7 Discussion

Electro-optical characterization of the detector array shows that the performance of the diodes is comparable with the latest results in the literature in terms of dark current and quantum efficiency.

Figure 3.22 shows the dark current density results obtained in this work and other research groups. Note that the cut-off wavelength of fabricated HgCdTe detector is 2.17 µm. Therefore the dark current density is expected to be lower than HgCdTe detectors with higher cut-off wavelength. Table 3.1 shows the quantum efficiencies of HgCdTe SWIR detectors of different research groups. Some of them have no information about anti reflection coating.

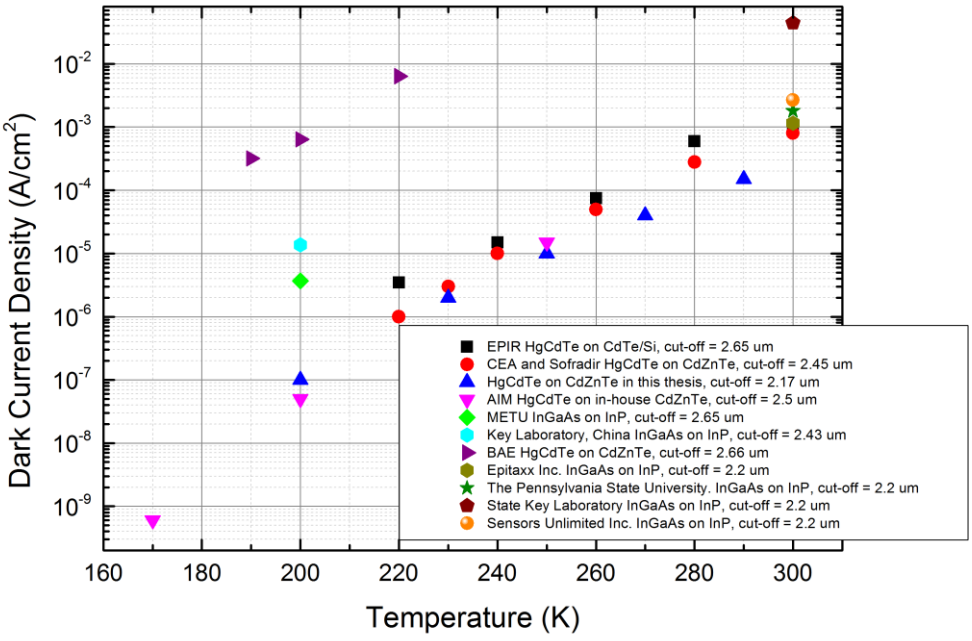

Figure 3.22 Dark current density of HgCdTe and extended InGaAs detectors vs temperature of different research groups including own grown layer. (Compared data are taken from the references used in Section 1.6)

Table 3.1 Quantum efficiencies of HgCdTe detectors from different research groups.

	Quantum Efficiency
EPIR HgCdTe on CdTe/Si, cut-off = 2.65 um without AR	70
AIM HgCdTe on in-house CdZnTe, cut-off = 2.5 um	74
CEA and Sofradir HgCdTe on CdZnTe, cut-off = 2.45 um	70
HgCdTe on CdZnTe in this thesis, cut-off = 2.17 um without AR	65
Sensors Unlimited, Inc. InGaAs on InP, cut-off = 2.2 um without AR	50
State Key Laboratory, InGaAs on InP, cut-off = 2.2 um	70

The dark current characterization indicates that the dark current of our diode is lower than state of the art studies for one order of magnitude, however it should not be forgotten that the cut-off wavelength of our layer is 2.17 μm. If the cut-off wavelength was 2.6 μm which is comparable to other studies, then the dark current would be higher. Therefore it is difficult to compare our results with HgCdTe detectors having higher cut-off wavelength values than 2.17 μm. The reason why the dark current is not much lower than that of other studies originates from the growth conditions and the substrate degrading the diode performance.

CHAPTER 4

CONCLUSION

In this thesis study, extended wavelength short wave infrared (SWIR) $Hg_{1-x}Cd_xTe$ layers were grown on 20mmx20mm home-polished CdZnTe substrates by molecular beam epitaxy (MBE) and support test arrays with 30 μm pitch were fabricated. Electrical and optical characterization were performed and the results are promising for future production of extended SWIR HgCdTe photodetectors and comparable with the results of state of the art studies.

MBE growth of HgCdTe is a challenging study, since lots of growth parameters affect the quality of the layers grown. In this study, the growth parameters are studied to be able to obtain SWIR HgCdTe layers. High Resolution X-Ray Diffraction, Fourier Transform Infrared Spectroscopy and Scanning Electron Microscopy methods were used to tune the growth parameters.

The tested layer has 2.17 μm cut-off wavelength at room temperature. The dark current density at room temperature is roughly ~100 $\mu A/cm^2$ which is diffusion limited. The dark current modeling indicates that the diffusion current dominates the dark current up to 1 V reverse bias at 230K. The R_0A product is $2.48x10^4$ Ω at 230K. The peak responsivity of the test diodes is 1.0 A/W with a quantum efficiency of 62% at room temperature. The dark current limited peak detectivity is $1.17x10^{11}$ $cm\sqrt{Hz}/W$ at room temperature.

DLTS measurements state that there is an effective hole (minority) trap with an activation energy of 267 meV.

In conclusion, we have demonstrated the extended SWIR HgCdTe detector performance achievable with limited quality CdZnTe substrates. We believe that our results are useful for understanding the limitations of efforts toward decreasing the cost of HgCdTe sensors.

REFERENCES

[1] H. Tang, X. Li, K. Zhang, L. Ye, N. Wang, X. Li, H. Gong, "High uniformity InGaAs linear mesa-type SWIR focal plane arrays," presented at the Infrared Materials, Devices, and Applications, Proc.SPIE, 2008, vol. 6835, p. 16.

[2] G. Cao, T. Li, H. Tang, X. Shao, X. Li, and H. Gong, "Performance of extended wavelength InGaAs/InAsP SWIR detector," presented at the 7th International Symposium on Advanced Optical Manufacturing and Testing Technologies: Optoelectronics Materials and Devices for Sensing and Imaging, Proc.SPIE, 2014, vol. 9284, p. 6.

[3] A. Rogalski, "Infrared detectors: an overview," *Infrared Phys. Technol.*, vol. 43, no. 3–5, pp. 187–210, Jun. 2002.

[4] J. D. Vincent, S. E. Hodges, J. Vampola, M. Stegall, and G. Pierce, *Fundamentals of infrared and visible detector operation and testing*, Second edition. Hoboken, New Jersey: Wiley, 2016.

[5] M. Vollmer and K.-P. Möllmann, *Infrared thermal imaging: fundamentals, research and applications*. Weinheim: Wiley-VCH, 2010.

[6] C. Beşikci, "EE514 Lecture Notes," METU, 2013.

[7] "Atmosfaerisk_spredning.png (588x300)." [Online]. Available: https://upload.wikimedia.org/wikipedia/commons/1/1c/Atmosfaerisk_spredning.png.

[8] F. Träger, Ed., *Springer handbook of lasers and optics: with 136 tables*. New York, NY: Springer, 2007.

[9] A. Rogalski and K. Chrzanowski, "Infrared Devices And Techniques (Revision)," *Metrol. Meas. Syst.*, vol. 21, no. 4, Jan. 2014.

[10] M. Henini and M. Razeghi, Eds., *Handbook of infrared detection technologies*. Oxford: Elsevier Science Ltd, 2002.

[11] T. Kanno *et al.*, "Uncooled infrared focal plane array having 128 x 128 thermopile detector elements," presented at the Infrared Technology XX, Proc.SPIE, 1994, vol. 2269, pp. 450–460.

[12] Gordon K.O. Tsen, “Investigation of molecular beam epitaxy grown p-type mercury cadmium telluride for infrared detector applications,” PhD Thesis, The University of Western Australia, 2010.

[13] A.Rogalski, “Infrared Photon Detectors,” SPIE Optical Engineering Press, 1995.

[14] Richard H. Sewell BE(Hons), “Investigation of mercury cadmium telluride heterostructures grown by molecular beam epitaxy,” PhD Thesis, The University of Western Australia, 2005.

[15] Pierre-Yves Emelie, “HgCdTe Auger-Suppressed Infrared Detectors Under Non-Equilibrium Operation,” PhD Thesis, The University of Michigan, 2009.

[16] G. D. Boreman, *Basic electro-optics for electrical engineers*. Bellingham, Wash: SPIE Optical Engineering Press, 1998.

[17] J.Piotrowski and F.Perry, “Designers Still Choose Mercury Cadmium Telluride,” *Laser Focus World*, Jul. 1997.

[18] R. S. Allgaier, “History of narrow-gap semiconductors and semimetals, 1945-65,” *Semicond. Sci. Technol.*, vol. 5, no. 3S, pp. S326–S333, Mar. 1990.

[19] “bandgap_misfit.gif (857x552).” [Online]. Available: https://www.tf.uni-kiel.de/matwis/amat/semitech_en/kap_2/illustr/bandgap_misfit.gif.

[20] P. Capper and J. Garland, Eds., *Mercury cadmium telluride: growth, properties and applications*. Chichester: Wiley, 2011.

[21] A. Rogalski, “HgCdTe infrared detector material: history, status and outlook,” *Rep. Prog. Phys.*, vol. 68, no. 10, pp. 2267–2336, Oct. 2005.

[22] M. A. Kinch, *Fundamentals of infrared detector materials*. Bellingham, Wash: SPIE, 2007.

[23] Norton, P., “HgCdTe Infrared Detectors,” *Optoelectron. Rev.*, pp. 159–174, 2002.

[24] M. Jaime-Vasquez, R.N. Jacobs, C. Nozaki, J.D. Benson, L.A. Almeida, J. Arias, J. Pellegrino, “Understanding the Evolution of CdTe Buffer Layer Surfaces on ZnTe/Si(211) and GaAs(211)B During Cyclic Annealing,” J. Electron. Mater., vol. 41, no. 10, pp. 2975–2980, Oct. 2012.

[25] J. W. Garland and S. Sivananthan, “Molecular-Beam Epitaxial Growth of HgCdTe,” in *Springer Handbook of Crystal Growth*, G. Dhanaraj, K. Byrappa, V. Prasad, and M. Dudley, Eds. Berlin, Heidelberg: Springer Berlin Heidelberg, 2010, pp. 1069–1132.

[26] Alp Tolungüç, "Moleculer Beam Epitaxy Growth and Characterization of Mercury Cadmium Telluride Epilayers For Infrared Detector Applications," M.Sc. Thesis, Middle East Technical University, 2011.

[27] P. Knowles *et al.*, "Status of IR detectors for high operating temperature produced by MOVPE growth of MCT on GaAs substrates," presented at the Electro-Optical and Infrared Systems: Technology and Applications IX, Proc.SPIE, 2012, vol. 8541, p. 8.

[28] R. Triboulet, "The Travelling Heater Method (THM) for Hg1−xCdxTe and related materials," *Prog. Cryst. Growth Charact. Mater.*, vol. 28, no. 1–2, pp. 85–144, Jan. 1994.

[29] G. Dhanaraj, Ed., *Springer handbook of crystal growth*. Berlin: Springer, 2010.

[30] P. Capper and M. Mauk, Eds., *Liquid phase epitaxy of electronic, optical and optoelectronic materials*. Hoboken, NJ: Wiley, 2007.

[31] S. Kasap, Ed., *Springer handbook of electronic and photonic materials: with 168 tables*. New York, NY: Springer, 2006.

[32] K. R. Linga, G. H. Olsen, V. S. Ban, A. N. Joshi, and W. F. Kosonocky, "Dark current analysis and characterization of InxGa1-xAs/InAsyP1-y graded photodiodes with x>0.53 for response to longer wavelengths (>1.7um)," *J. Light. Technol.*, vol. 10, no. 8, pp. 1050–1055, Aug. 1992.

[33] G. H. Olsen, M. J. Lange, M. J. Cohen, D.-S. Kim, and S. R. Forrest, "Three-band 1.0-2.5 um near-infrared InGaAs detector array," presented at the Infrared Detectors and Focal Plane Arrays III, Proc.SPIE, 1994, vol. 2225, pp. 151–160.

[34] R. Kochhar, W.Y. Hwang, M. Micovic, T. S. Mayer, D. L. Miller, and S. M. Lord, "Development of 2.2-um InGaAs photodetectors using molecular beam epitaxy," presented at the Lasers and Electro-Optics, CLEO '96 Anaheim, 1996, pp. 198–199.

[35] J. John, L. Zimmermann, S. Nemeth, T. Colin, P. Merken, S. Borghs, C.A.V. Hoof, "Extended InGaAs on GaAs detectors for SWIR linear sensors," presented at the Infrared Technology and Applications XXVII, Proc.SPIE, 2001, vol. 4369, pp. 692–698.

[36] M. H. Ettenberg, M. A. Blessinger, M. T. O'Grady, S.-C. Huang, R. M. Brubaker, and M. J. Cohen, "High-resolution SWIR arrays for imaging at night," presented at the Infrared Technology and Applications XXX, Proc.SPIE, 2004, vol. 5406, pp. 46–56.

[37] H. Guo-Qiang, Z. Yong-Gang, G. Yi, L. Ai-Zhen, and Z. Cheng, "Performance analysis of extended wavelength InGaAs photovoltaic detectors grown with gas source MBE," *J Infrared Millim Waves*, vol. 25, pp. 241–245, 2006.

[38] M. MacDougal *et al.*, "InGaAs focal plane arrays for low-light-level SWIR imaging," presented at the Infrared Technology and Applications XXXVII, Proc.SPIE, 2011, vol. 8012, p. 21.

[39] H. Yuan, M. Meixell, J. Zhang, P. Bey, J. Kimchi, and L. C. Kilmer, "Low dark current small pixel large format InGaAs 2D photodetector array development at Teledyne Judson Technologies," SPIE DSS, 2012, vol. 8353, p. 7.

[40] A. D. Hood, M. H. MacDougal, J. Manzo, D. Follman, and J. C. Geske, "Large-format InGaAs focal plane arrays for SWIR imaging," presented at the Infrared Technology and Applications XXXVIII, Proc.SPIE, 2012, vol. 8353.

[41] F. Rutz, P. Kleinow, R. Aidam, W. Bronner, L. Kirste, and M. Walther, "InGaAs infrared detector development for SWIR imaging applications," Proc.SPIE, 2013, vol. 8896.

[42] Y. Arslan, F. Oguz, and C. Besikci, "Extended wavelength SWIR InGaAs focal plane array: Characteristics and limitations," *Infrared Phys. Technol.*, vol. 70, pp. 134–137, May 2015.

[43] N. Cohen and O. Aphek, "Extended wavelength SWIR detectors with reduced dark current," presented at the Infrared Technology and Applications XLI, Proc.SPIE, 2015, vol. 9451, p. 6.

[44] P. Chorier and P. M. Tribolet, "High-performance HgCdTe SWIR detector development at SOFRADIR," presented at the Infrared Technology and Applications XXVII, Proc.SPIE, 2001, vol. 4369, pp. 698–713.

[45] J.-S. Kim, S.-Y. An, and S.-H. Suh, "SWIR diodes of HgCdTe on GaAs substrates grown by metal organic vapor phase epitaxy," presented at the Materials for Infrared Detectors II, Proc.SPIE, 2002, vol. 4795, pp. 207–213.

[46] H. R. Vydyanath, P. Lamarre, S. P. Tobin, A. W. Hairston, P. W. Norton, and L. S. R. Becker, "High-operability SWIR HgCdTe focal plane arrays," presented at the Materials for Infrared Detectors III, Proc.SPIE, 2003, vol. 5209, pp. 33–58.

[47] A. Hairston *et al.*, "SWIR HgCdTe 256x256 focal plane array technology at BAE Systems," presented at the Infrared Detectors and Focal Plane Arrays VIII, Proc.SPIE, 2006, vol. 6295.

[48] O. Gravrand, L. Mollard, O. Boulade, V. Moreau, E. Sanson, and G. Destefanis, "Ultralow-Dark-Current CdHgTe FPAs in the SWIR Range at CEA and Sofradir," *J. Electron. Mater.*, vol. 41, no. 10, pp. 2686–2693, Oct. 2012.

[49] R. Bommena *et al.*, "High-performance SWIR HgCdTe FPA development on silicon substrates," presented at the Infrared Technology and Applications XL, Proc.SPIE, 2014, vol. 9070, p. 9.

[50] H. Figgemeier, M. Benecke, K. Hofmann, R. Oelmaier, A. Sieck, J. Wendler, J. Ziegler, “SWIR detectors for night vision at AIM,” presented at the Infrared Technology and Applications XL, Proc.SPIE, 2014, vol. 9070, p. 8.

[51] A. Weber, M. Benecke, J. Wendler, A. Sieck, D. Hübner, H. Figgemeier, R. Breiter, “Extended SWIR imaging sensors for hyperspectral imaging applications,” presented at the Image Sensing Technologies: Materials, Devices, Systems, and Applications III, Proc.SPIE, 2016, vol. 9854.

[52] R. Breiter *et al.*, “MCT SWIR modules for passive and active imaging applications,” Proc.SPIE, 2016, vol. 9819, p. 8.

[53] X. Hu *et al.*, “Large format high SNR SWIR HgCdTe/Si FPA with multiple-choice gain for hyperspectral detection,” presented at the Hyperspectral Imaging Sensors: Innovative Applications and Sensor Standards 2017, Proc.SPIE, 2017, vol. 10213.

[54] A. Ichimiya and P. I. Cohen, *Reflection high-energy electron diffraction*, 1. paperback ed. Cambridge: Cambridge Univ. Press, 2010.

[55] J. D. Benson *et al.*, “Analysis of Etched CdZnTe Substrates,” *J. Electron. Mater.*, vol. 45, no. 9, pp. 4502–4510, Sep. 2016.

[56] Zandian, Majid, “Studies of arsenic incorporation and p-type doping in epitaxial HgCdTe thin films grown by MBE,” PhD Thesis, The University of Southern California, 2003.

[57] E. C. Piquette, M. Zandian, D. D. Edwall, and J. M. Arias, “MBE growth of HgCdTe epilayers with reduced visible defect densities: Kinetics considerations and substrate limitations,” *J. Electron. Mater.*, vol. 30, no. 6, pp. 627–631, Jun. 2001.

[58] G. K. O. Tsen, J. Zhang, C. A. Musca, J. M. Dell, J. Antoszewski, and L. Faraone, “Various annealing methods for activation of arsenic in Molecular Beam Epitaxy grown HgCdTe,” presented at the Conference on Optoelectronic and Microelectronic Materials and Devices, IEEE, 2008, pp. 125–128.

[59] G. K. O. Tsen, J. Zhang, C. A. Musca, J. M. Dell, J. Antoszewski, and L. Faraone, “Various annealing methods for activation of arsenic in Molecular Beam Epitaxy grown HgCdTe,” 2008, pp. 125–128.

[60] L. He *et al.*, “Composition control and surface defects of MBE-grown HgCdTe,” *J. Cryst. Growth*, vol. 227–228, pp. 677–682, Jul. 2001.

[61] T. Aoki *et al.*, “Defect characterization for epitaxial HgCdTe alloys by electron microscopy,” *J. Cryst. Growth*, vol. 265, no. 1–2, pp. 224–234, Apr. 2004.

[62] T. Aoki *et al.*, "Electron microscopy of surface-crater defects on HgCdTe/CdZnTe(211)B epilayers grown by molecular-beam epitaxy," *J. Electron. Mater.*, vol. 32, no. 7, pp. 703–709, Jul. 2003.

[63] R. Haakenaasen *et al.*, "HgCdTe Research at FFI: Molecular Beam Epitaxy Growth and Characterization," *J. Electron. Mater.*, vol. 39, no. 7, pp. 893–902, Jul. 2010.

[64] I. V. Sabinina, A. K. Gutakovsky, Y. G. Sidorov, and A. V. Latyshev, "Nature of V-shaped defects in HgCdTe epilayers grown by molecular beam epitaxy," *J. Cryst. Growth*, vol. 274, no. 3–4, pp. 339–346, Feb. 2005.

[65] E. Selvig *et al.*, "Defects in CdHgTe grown by molecular beam epitaxy on (211)B-oriented CdZnTe substrates," *J. Vac. Sci. Technol. B Microelectron. Nanometer Struct.*, vol. 26, no. 2, p. 525, 2008.

[66] E. Selvig, C. R. Tonheim, T. Lorentzen, K. O. Kongshaug, T. Skauli, and R. Haakenaasen, "Defects in HgTe and CdHgTe Grown by Molecular Beam Epitaxy," *J. Electron. Mater.*, vol. 37, no. 9, pp. 1444–1452, Sep. 2008.

[67] E. Selvig, C. R. Tonheim, K. O. Kongshaug, T. Skauli, T. Lorentzen, and R. Haakenaasen, "Defects in HgTe grown by molecular beam epitaxy on (211)B-oriented CdZnTe substrates," *J. Vac. Sci. Technol. B Microelectron. Nanometer Struct.*, vol. 25, no. 6, p. 1776, 2007.

[68] M. Martinka, L. A. Almeida, J. D. Benson, and J. H. Dinan, "Characterization of cross-hatch morphology of MBE (211) HgCdTe," *J. Electron. Mater.*, vol. 30, no. 6, pp. 632–636, Jun. 2001.

[69] A. Rogalski and R. Ciupa, "Long-wavelength HgCdTe photodiodes: n^+-on-p versus p-on-n structures," *J. Appl. Phys.*, vol. 77, no. 7, pp. 3505–3512, Apr. 1995.

[70] A. Rogalski, A. Jóźwikowska, K. Jóźwikowski, and J. Rutkowski, "Performance of p+−n HgCdTe photodiodes," *Infrared Phys.*, vol. 33, no. 6, pp. 463–473, Nov. 1992.

[71] M. Carmody *et al.*, "Recent Progress in MBE Growth of CdTe and HgCdTe on (211)B GaAs Substrates," *J. Electron. Mater.*, vol. 41, no. 10, pp. 2719–2724, Oct. 2012.

[72] V. Gopal, S. K. Singh, and R. M. Mehra, "Analysis of dark current contributions in mercury cadmium telluride junction diodes," *Infrared Phys. Technol.*, vol. 43, no. 6, pp. 317–326, Dec. 2002.

[73] Y. Nemirovsky, D. Rosenfeld, R. Adar, and A. Kornfeld, "Tunneling and dark currents in HgCdTe photodiodes," *J. Vac. Sci. Technol. Vac. Surf. Films*, vol. 7, no. 2, pp. 528–535, Mar. 1989.

[74] Y. Nemirovsky, “Tunneling and 1/f noise currents in HgCdTe photodiodes,” *J. Vac. Sci. Technol. B Microelectron. Nanometer Struct.*, vol. 10, no. 4, p. 1602, Jul. 1992.

[75] V. Gopal, S. K. Singh, and R. M. Mehra, “Excess dark currents in HgCdTe p^+-n junction diodes,” *Semicond. Sci. Technol.*, vol. 16, no. 5, pp. 372–376, May 2001.

[76] A. S. Gilmore, J. Bangs, and A. Gerrish, “Current voltage modeling of current limiting mechanisms in HgCdTe focal plane array photodetectors,” *J. Electron. Mater.*, vol. 34, no. 6, pp. 913–921, Jun. 2005.

[77] Zenan Jiang, “Deep Level Transient Spectroscopy Measurements of GaAsBi/GaAs,” M.Sc. Thesis, Simon Fraser University, 2010.

[78] L. Gelczuk, M. Dabrowska, and G. Jozwiak, “Distinguishing and identifying point and extended defects in DLTS measurements,” *Mater. Sci. Pol.*, vol. 23, no. 3, pp. 625–641, 2005.

[79] Vincent Quemener, “Deep Level Transient Spectroscopy,” University of Oslo.

[80] Tony Peaker, “Deep Level Transient Spectroscopy and Shockley-Read-Hall Kinetics,” University of Manchester, 2011.